

© 2018 by Yakov Kulinich. All rights reserved.

DIJET AZIMUTHAL CORRELATIONS AND CONDITIONAL YIELDS IN pp AND
p+Pb COLLISIONS AT $\sqrt{S_{\text{NN}}} = 5.02$ TeV WITH THE ATLAS DETECTOR

BY

YAKOV KULINICH

DISSERTATION

Submitted in partial fulfillment of the requirements
for the degree of Doctor of Philosophy in Physics
in the Graduate College of the
University of Illinois at Urbana-Champaign, 2018

Urbana, Illinois

Doctoral Committee:

Professor Alexey Bezryadin

Professor Matthias Grosse Perdekamp, Co-Director of Research

Professor Anne Marie Sickles, Co-Director of Research

Professor Scott Willenbrock

Professor Liang Yang, Chair

Abstract

This dissertation presents a measurement of forward-forward and forward-central dijet azimuthal angular correlations and conditional yields in proton-proton (pp) and proton-lead ($p+\text{Pb}$) collisions as a probe for possible gluon-density saturation at low parton momentum fractions x of the lead nucleus. Gluon saturation can modify the rapidly increasing parton distribution function of the gluon at low x . The analysis utilizes 25 pb^{-1} of pp data and $360 \mu\text{b}^{-1}$ of $p+\text{Pb}$ data, both at $\sqrt{s_{\text{NN}}} = 5.02 \text{ TeV}$, collected in 2015 and 2016, respectively, with the ATLAS detector at the LHC. The measurement is performed in the center-of-mass frame of the nucleon–nucleon system in the rapidity range $-4.0 < y^* < 4.0$ using the two highest transverse momentum jets in each event. The highest transverse momentum jet is restricted to the forward rapidity range where it is possible to probe the low- x region of the lead nucleus wave function. No significant broadening of azimuthal angular correlations is observed for forward-forward or forward-central dijets in $p+\text{Pb}$ compared to pp collisions within the statistical and systematic uncertainties. The ratio of conditional yields of jet pairs in the proton-going direction in $p+\text{Pb}$ collisions compared to pp collisions is suppressed by approximately 20%, with no significant dependence on the transverse momentum of the dijets system or center-of-mass rapidity.

Table of Contents

List of Abbreviations	vi
List of Symbols	viii
Introduction	ix
Chapter 1 Experimental Setup	1
1.1 LHC	1
1.2 ATLAS Experiment	3
1.2.1 ATLAS Trigger System	4
1.2.2 Calorimetry	5
1.2.3 Solenoid Magnet	13
1.2.4 Inner Detector	13
Chapter 2 Theoretical Introduction	15
2.1 Quantum Chromo-Dynamics	15
2.2 Deep Inelastic Scattering	18
2.3 Parton Distribution Functions	19
2.4 Hadronic Collisions and Jets	23
2.4.1 Anti- k_t Jets	25
2.5 Gluon Saturation	27
2.6 Color Glass Condensate	29
2.7 Measured Observables	30
Chapter 3 ATLAS Required Qualification Work	33
3.1 Event Selection and Cuts	33
3.2 Procedure	34
3.3 Results	34
3.4 Conclusion	35
Chapter 4 Measurement of Dijet Azimuthal Correlations	37
4.1 Overview	37
4.2 Data Sets	38
4.3 Trigger and Event Selection	39
4.3.1 General Cuts	39
4.3.2 Trigger Selection	40
4.3.3 Disabled HEC in $p+\text{Pb}$ Data-taking	43
4.4 Jet Selection and Reconstruction Performance	44
4.5 Analysis Procedure	50
4.5.1 Overview	50
4.5.2 Unfolding Procedure	51
4.5.3 Jet Spectra	53

4.5.4	Jet Spectra Re-weighting	55
4.5.5	Jet Spectra Unfolding	56
4.5.6	Dijet Azimuthal Distributions C_{12}	56
4.5.7	Re-weighting C_{12} Distributions	57
4.5.8	Fitting of C_{12} Distributions	59
4.5.9	Unfolding C_{12} Distributions	61
4.5.10	MC Closure Test	62
4.5.11	Isolation Requirements	64
4.6	Systematic Uncertainties	65
4.6.1	Overview	65
4.6.2	Systematic Uncertainty Due to the Jet Energy Scale	66
4.6.3	Additional Systematic Uncertainty in $p+\text{Pb}$ Due to the Jet Energy Scale	66
4.6.4	Systematic Uncertainty Due to the Jet Energy Resolution	67
4.6.5	Systematic Uncertainty Due to the Jet Angular Resolution	68
4.6.6	Systematic Uncertainty Due to Unfolding	69
4.6.7	Systematic Uncertainty Due to Fitting	70
4.6.8	Systematic Uncertainty Due to the HEC	71
4.6.9	Summary of Systematic Uncertainties	72
4.7	Results	77
4.7.1	C_{12} Distributions and Their Fits	77
4.7.2	Widths and Conditional Yields With no Δp_T Requirement	78
4.7.3	Widths and Conditional Yields With a $\Delta p_T > 3$ GeV Requirement	79
Chapter 5	Summary	83
Appendix A	Data Sets	84
Appendix B	Bin-by-bin Unfolding Procedure.	85
Appendix C	$\Delta\phi$ Correction Factors From pp MC Samples	90
Appendix D	$\Delta\phi$ Correction Factors From $p+\text{Pb}$ MC Samples	93
Appendix E	Appendix: Effect of Isolation Cuts	96
Appendix F	Effect of New JES Systematic Uncertainties	98
Appendix G	Fitting Systematic Uncertainties	101
Appendix H	Unfolded C_{12} Distributions from Data with Systematic Uncertainties	103
H.1	C_{12} distributions with no Δp_T requirement	103
H.2	C_{12} distributions with a requirement of $\Delta p_T > 3$ GeV	106
References	109

List of Abbreviations

LHC	Large Hadron Collider
ATLAS	A Toroidal LHC Apparatus
CERN	European Organization for Nuclear Research
LS	Long Shutdown
RF	Radio Frequency
LINAC	Linear Accelerator
ALICE	A Large Ion Collider Experiment
CMS	Compact Muon Solenoid
LHCb	LHC Beauty
IP	Interaction Point
ID	Inner Detector
EM	Electromagnetic
LAr	Liquid Argon
EMB	EM Barrel
EMEC	EM End-Cap
FCal	Forward Calorimeter
HEC	Hadronic End-Cap
TileCal	Tile Calorimeter
L1,L2	Level 1,2 Triggers
HLT	High Level Trigger
EF	Event Filtering
QCD	Quantum Chromo-Dynamics
IR	Infrared
pQCD	Perturbative QCD
QGP	Quark Gluon Plasma

DIS	Deep Inelastic Scattering
<i>ep</i>	Electron-Proton Collisions
<i>p + Au</i>	Proton-Gold Collisions
<i>pp</i>	Proton-Proton Collisions
<i>p+Pb</i>	Proton-Lead Collisions
HERA	Hadron-Electron Ring Accelerator
RHIC	Relativistic Heavy Ion Collider
RMS	Root-mean-square, synonym for standard deviation
MC	Monte-Carlo
GRL	Good Runs List
UE	Underlying Event
JER	Jet Energy Resolution
JES	Jet Energy Scale
JAR	Jet Angular Resolution

List of Symbols

z	Cartesian coordinate defined to be in the direction of the LHC beam direction.
$x - y$	Cartesian coordinates defined to be perpendicular to the LHC beam direction.
(E, p_x, p_y, p_z)	Four-vector describing energy and Cartesian momentum components of an object.
$p_{tot} = \sqrt{p_x^2 + p_y^2 + p_z^2}$	Total momentum of an object.
$\phi = \arcsin(p_z/p_T)$	Azimuthal angle in the $x - y$ plane perpendicular to the beam direction.
$\theta = \arccos(p_z/p_{tot})$	Polar angle with respect to the beam direction (z -axis).
$p_T = \sqrt{p_x^2 + p_y^2}$	Transverse momentum defined in the $x - y$ plane.
$\eta = -\ln \tan(\theta/2)$	Pseudorapidity, defined in terms of the polar angle θ .
$y = \frac{1}{2} \ln(\frac{E+p_z}{E-p_z})$	Rapidity, defined in terms of energy E .
$\Delta R \equiv \sqrt{(\Delta\eta)^2 + (\Delta\phi)^2}$	Measure of angular distance.
x	Parton longitudinal momentum fraction of a nucleon.
$\Delta\phi = \phi_1 - \phi_2$	Difference in azimuthal angle ϕ between two objects.
C_{12}	Azimuthal correlation between two jets normalized by the number of leading jets.
W_{12}	Width of the C_{12} distribution. Defined as the RMS or standard deviation of a fit to C_{12} .
I_{12}	Conditional yield, extracted as the integral of a C_{12} distribution.
$\rho_W^{p\text{Pb}}$	Ratio of W_{12} between pp and $p+\text{Pb}$ collisions.
$\rho_I^{p\text{Pb}}$	Ratio of I_{12} between pp and $p+\text{Pb}$ collisions.

Introduction

The fundamental properties of the matter surrounding us have always been of great interest to mankind. The word atom dates back to ancient Greece, and then almost 125 years ago, J.J Thompson discovered the electron, which is an elementary particle that almost everyone has heard of. In recent years, technology has allowed us to probe microscopic distances and study matter at an unprecedented level. To this day, many new breakthroughs in the understanding of microscopic and macroscopic properties of matter have been made.

The LHC, a particle collider in CERN, Switzerland, is currently the worlds most powerful machine for probing the properties of known matter and carrying out searches for new types of matter. It has contributed to the recent discovery of the Higgs boson and to an improved understanding of physics at high energies. The ATLAS detector is one of the largest instruments that measures collisions at the LHC and is the product of thousands of collaborators from hundreds of institutions from around the world. The author of this thesis is a member of the ATLAS collaboration, and had the privilege to use this wonderful machine and conduct the study which will be presented in this thesis.

One of the fundamental building blocks of matter surrounding us is the proton, which like the electron, is a well known particle to most readers. The properties and structure of the proton have attracted a lot of attention over the years. While many of its macroscopic properties such as its mass, charge, and lifetime are known to a precise degree, there remain many unanswered questions about its microscopic properties. This dissertation will present a measurement probing into one of these unanswered questions - the behavior of subatomic particles called *partons* at different energy regimes inside of the proton. More specifically, the measurement will focus on studying a parton called the *gluon*, which is a particle that binds together partons called *quarks*. These quarks and gluons, and the interactions between them, are currently described by a globally recognized model called the Standard Model. The system of three quarks, held together by three gluons, describes the simplest picture of the gluon. We will look at a more complex picture of the proton, where present measurements are not able to explain the observation that there is an unrealistically large (tending to infinity) amount of gluons seen in the proton at shorter timescales. This unphysical process has

to stop at some point, and this is described by a phenomenon called *saturation*.

This dissertation is split into four chapters. Chapter 1 describes the experimental apparatus used throughout this measurement. Chapter 2 gives a theoretical background that should help the reader understand the measurement that will be presented in this thesis. Chapter 3 presents a brief overview of the qualification work completed as a requirement for becoming a member of the ATLAS collaboration. Finally, Chapter 4 presents a detailed outline of the measurement along with its results.

In addition to carrying out this analysis into the structure of the proton. The author of this dissertation contributed to the commissioning of a large area drift chamber for the COMPASS experiment at CERN. The contributions included parts procurement, assembly, testing, and data acquisition for the detector. The author also contributed to the simulation work, assembly, and data taking at beam tests for new ATLAS zero degree calorimeter (ZDC) prototype.

I hope that you learn from, and enjoy reading this dissertation. Thank you.

Chapter 1

Experimental Setup

1.1 LHC

The Large Hadron Collider (LHC) [1] was built by the European Organization for Nuclear Research (CERN) and is located on the France-Switzerland border outside of Geneva. The LHC is designed to collide beams of protons at a center of mass energy up to $\sqrt{s}=14$ TeV and beams of lead ions at a center-of-mass energy per nucleon up to $\sqrt{s_{NN}}=8.16$ TeV. It is the largest of many accelerators that constitute the the CERN accelerator complex, pictured in Fig. 1.1.

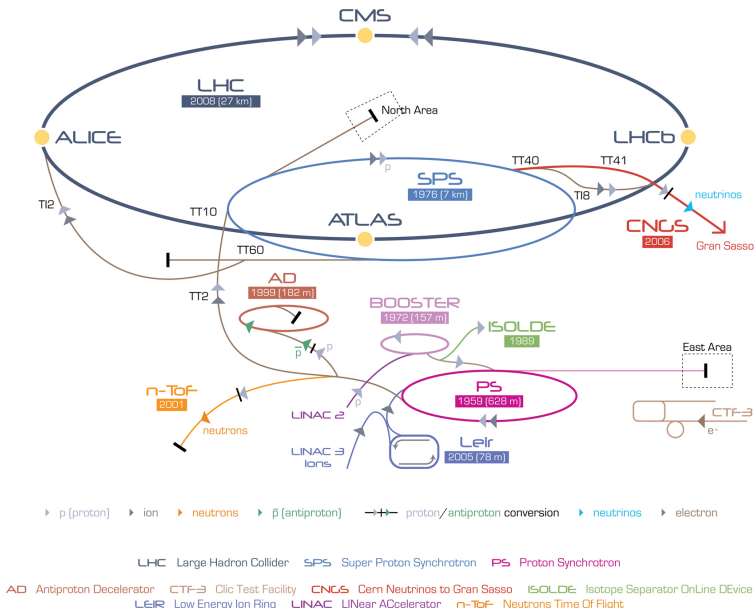


Figure 1.1: The accelerator complex at CERN. ATLAS can be seen inside the SPS on the LHC ring. Figure taken from Ref. [2]

During the LHC's first operational data taking run, referred to as Run 1 (2009-2013), the first collisions with stable beams were observed between protons and protons (pp), as well as protons with lead ions ($p+Pb$) at center of mass energies of $\sqrt{s}=8$ TeV and $\sqrt{s_{NN}}=2.76$ TeV, respectively. Center of mass energies for $p+Pb$ collisions were subsequently increased to $\sqrt{s_{NN}}=5.02$ TeV in 2013. After an extended technical shutdown for

upgrades following Run 1, the LHC was restarted for run Run 2, during which pp and $p+Pb$ collisions with stable beams were observed at center-of-mass energies of $\sqrt{s}=13$ TeV and $\sqrt{s_{NN}}=8.16$ TeV, respectively.

The LHC is located in a tunnel at depths of 50 to 175 m underground. Originally, this tunnel was built for the Large Electron-Proton Collider (LEP), an electron-proton collider that was operation from 1989-2000. In the LHC, particle packets in high vacuum beam pipes going in opposite directions are accelerated by 8 radio frequency cavities (RF) which deliver voltages up to 2 MV at an oscillator frequency of 400 MHz. Each 26.7 km ring consists of eight arched sections with 616 dipole super-conducting magnets per beam, which supply fields of up to 8.33 Tesla. An additional 196 beam focusing quadropole magnets per beam serve to narrow the beam and increase luminosity. To supply such high magnetic fields, LHC magnets use super-fluid helium and operate at temperatures down to 1.9 K while the RF cavities operate at temperatures down to 4.5 K.

Any proton or lead ion entering the LHC must go through the complex chain of accelerators shown in Fig. 1.1. In order to be accelerated and focused in the beams, the proton and lead ions are required to have a net positive charge. Thus, the hydrogen and lead atoms must be first stripped of the electrons in their atomic shells. Positively charged protons are obtained by stripping atoms of hydrogen gas from their electrons using an electric field. Positively charged lead ions are initially extracted from a source which provides partially stripped lead ions with an average around Pb^{29+} . These ions then go through a series of pre-accelerators, seen at the bottom of Fig. 1.1, starting with the Linear Accelerator 3 (LINAC3) where they are further stripped of electrons by passing through 3.0 μm of carbon foil. Next, a mass spectrometer selects lead ions with an average Pb^{29+} to be fed into the Low Energy Ion Ring (LEIR). The protons, meanwhile, begin their journey at the Linear Accelerator 2 (LINAC2). Both protons and lead ions then enter the next phase of pre-accelerators which consist of the Proton Synchrotron (PS) and the Super Proton Synchrotron (SPS), where they continue to be accelerated. The lead ions are completely stripped away of remaining electrons at the exit of the PS, where they pass through 0.8 mm aluminum foil. The final stage is at the exit of the SPS where the protons and lead ions enter the LHC for the final phase of acceleration before they are collided.

Beams in the LHC consist of 2808 bunches of protons or lead ions with bunch spacing down to 25 ns (7.5 m). A proton bunch contains approximately 1.15×10^{11} protons while an ion bunch contains approximately 2.2×10^8 ions. These beams are brought to collide at four interaction points which can be seen along the circumference of the LHC in Fig. 1.1. At these interaction points there are detectors present to analyze the collisions: A Large Ion Collider Experiment (ALICE), A Toroidal LHC Apparatus (ATLAS), Compact Muon Solenoid (CMS), and the Large Hadron Collider Beauty (LHCb).

1.2 ATLAS Experiment

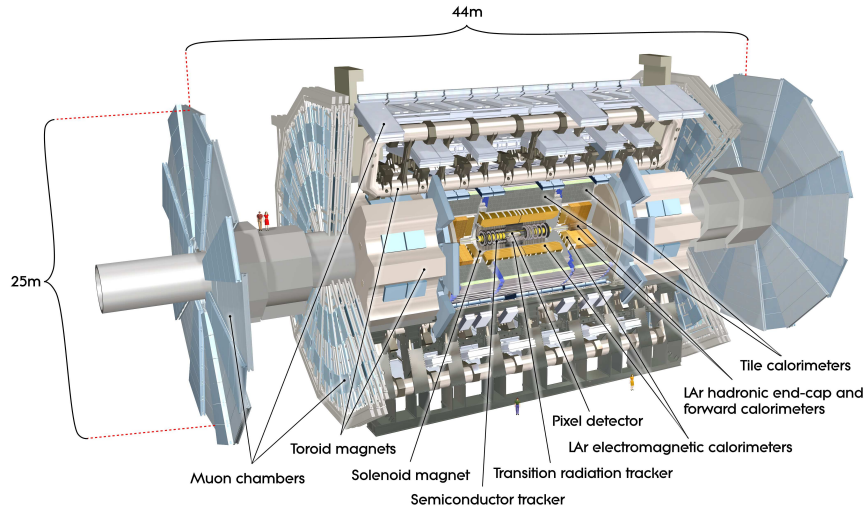


Figure 1.2: The ATLAS detector. Figure taken from Ref. [3].

The ATLAS detector [3], shown in Fig. 1.2 is one of the two larger detectors on the LHC and is located at interaction point 1 (IP1) on the LHC ring¹. It is designed to perform measurements of Standard Model physics, including the search for the Higgs boson, and search for physics beyond the Standard Model. Although ATLAS is primarily a detector used to measure pp collisions, it has also been used to study Heavy Ion physics with much higher nuclear collision energies and much larger particle multiplicities compared to pp collision.

The ATLAS detector consists of four main parts, or sub-detectors. The closest part to the interaction point is the Inner Detector (ID), which is placed close to the IP and is used to measure charged particle tracks. The ID is inside a 2 Tesla solenoidal magnetic field, which causes charged particles to curve, allowing their momentum to be measured. Outside of the ID are the electromagnetic (EM) and hadronic calorimeters. These give energy measurements and are the primary detectors for the analysis presented in this thesis. The fourth and outermost part is the muon spectrometer which is placed inside a toroidal field provided by eight toroid magnets. The muon system is the outermost part of the detector because due to their weakly interacting nature, muons are one of the only particles which pass through the calorimeters. All of the ATLAS sub-detectors have full 2π azimuthal coverage and different pseudorapidity coverages shown in

¹ ATLAS uses a right-handed coordinate system with its origin at the nominal interaction point (IP) in the centre of the detector and the z -axis along the beam pipe. The x -axis points from the IP to the centre of the LHC ring, and the y axis points upward. Cylindrical coordinates (r, ϕ) are used in the transverse plane, ϕ being the azimuthal angle around the beam pipe. The pseudorapidity is defined in terms of the polar angle θ as $\eta = -\ln \tan(\theta/2)$. Angular distance is measured in units of $\Delta R \equiv \sqrt{(\Delta\eta)^2 + (\Delta\phi)^2}$. Rapidity is defined in terms of energy and momentum of a particle or jet as $y = \frac{1}{2} \ln(\frac{E+p_z}{E-p_z})$. The rapidity with center-of-mass frame boost accounted for is denoted y^* .

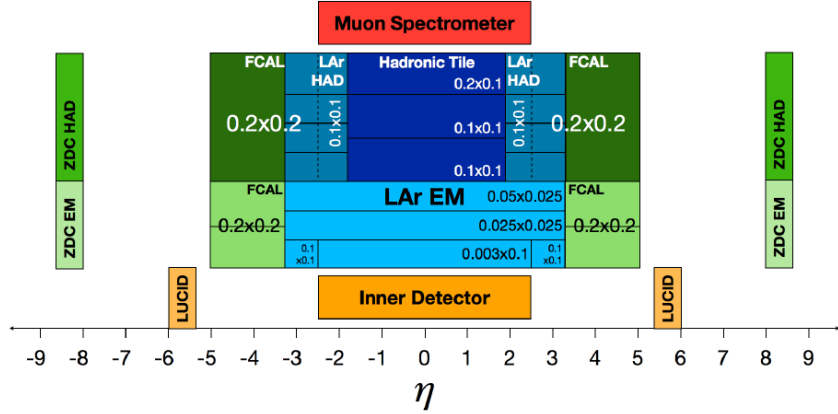


Figure 1.3: ATLAS detector pseudorapidity coverage. All components cover 2π in azimuth.

Fig. 1.3. A detailed description of the ATLAS detector and its subsystems can be found in [3].

1.2.1 ATLAS Trigger System

In order to select events during data-taking, a complex hardware and software system called the *trigger* is required. It relies on many detector subsystems to flag events based on a set of rules that are defined prior to each run. A two-level trigger system was used to select the pp and $p+\text{Pb}$ collisions analyzed for the measurement presented in this thesis. The first, the hardware-based trigger stage Level-1 (L1), is implemented with custom electronics. The second level is the software-based High Level Trigger (HLT). The HLT consists of the Level-2 (L2) trigger, followed by the event filter (EF). The ATLAS trigger was designed for a collision rate of 40 MHz, with the L1 trigger designed to reduce the rate to 75 kHz, and the HLT to perform a final reduction to about 200 Hz, which is the final even rate written to disk. A schematic of the ATLAS trigger and data acquisition systems can be seen in Fig. 1.4. Some triggers selecting minimum-bias (MB) events used the minimum-bias trigger scintillator detectors (MBTS). The MBTS detect charged particles over $2.1 < |\eta| < 3.9$ using two segmented counters placed at $z = \pm 3.6$ m. Each counter provides measurements of both the pulse heights and the arrival times of ionization energy deposits [3].

Some triggers can be prescaled, meaning that not every event meeting the requirements of a particular trigger is saved to disk. If a trigger with prescale c_p is saved n times, this corresponds to $c_p n$ events passing through the HLT. The decision of what prescale to assign to a trigger is very complicated. Various physics analysis groups have different requirements, but unfortunately not all data from a run can be saved due to technical limitations. Depending on the physics goals of a particular run, the trigger menu, which assigns the triggers and their respective prescales, will change. The UIUC ATLAS group has been responsible for the trigger system operation in all of the heavy ion runs since 2015.

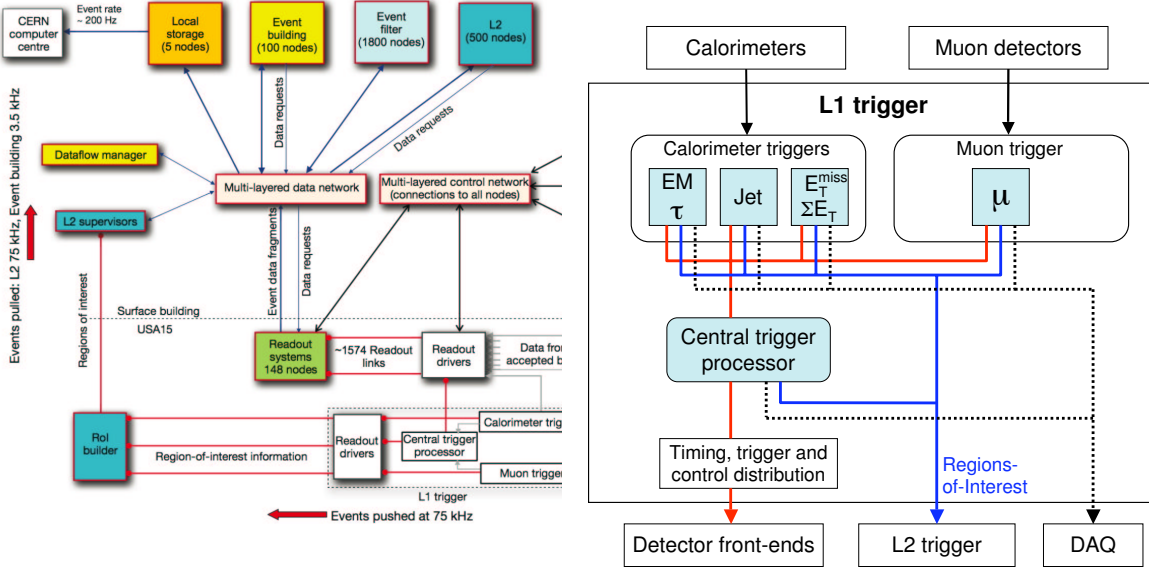


Figure 1.4: A schematic (left) of the ATLAS trigger and data acquisition systems, and the L1 hardware trigger (right). The total event rate of about 40 MHz is reduced by the L1 trigger to about 75 kHz, and further reduced to 200 Hz by the HLT (L2 + EF) trigger. Figure taken from Ref. [3].

1.2.2 Calorimetry

The ATLAS calorimeter system [3] is the main system used for the present analysis, a picture of this system is shown in Fig. 1.5. The calorimeters are of sampling and non-compensating nature with a pseudorapidity coverage of $|\eta| < 4.9$. The non-compensating nature gives a different response on the EM and hadronic scales, and this is corrected in the calibration procedure. A sampling calorimeter is one where two distinctly different materials are chosen, one to produce a particle shower, and the other to measure the deposited energy.

There are two different sampling technologies used in the ATLAS calorimeter system. One technology is where liquid argon (LAr) is interspersed with lead, which acts as the absorber material. This is used in all of the ATLAS EM systems - the electromagnetic barrel (EMB), electromagnetic end-cap (EMEC), forward calorimeter (FCal), as well as the hadronic end-cap (HEC). Shower development starts in the absorber, and due to moving electrons and ions from ionization in the active material (LAr), a signal can be read out from induced charge on copper electrodes. The LAr gap is subject to a high voltage electric field in order

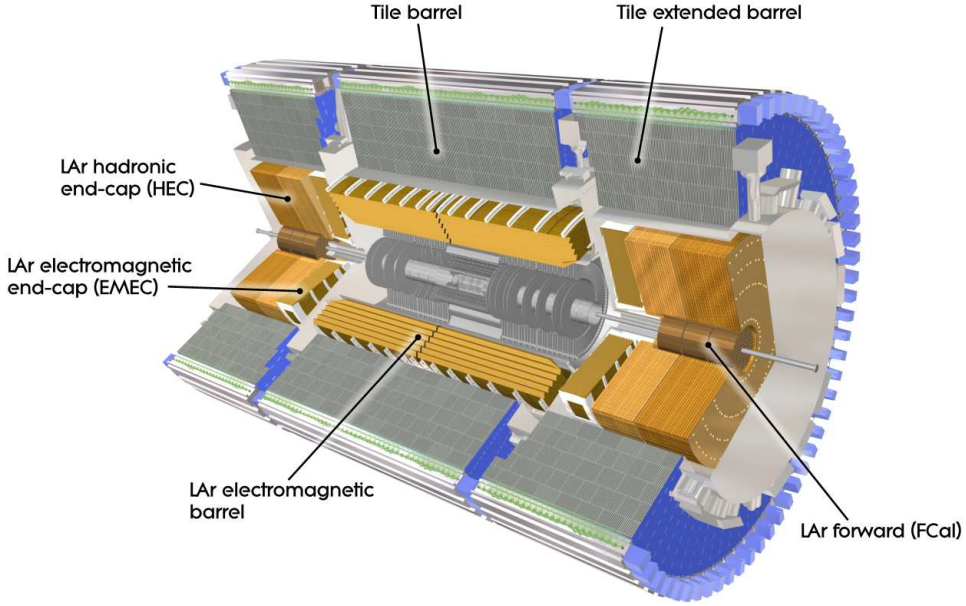


Figure 1.5: The ATLAS calorimeter system. Figure taken from Ref. [3].

to direct the ionized electrons and ions to the electrodes in a predictable way. The second technology, used in the hadronic tile calorimeters (TileCal), uses absorber material interspersed with plastic scintillator. The readout is different from the LAr case since scintillation light converted by wavelength shifting fibers and transported to photomultipliers instead of reading induced charge from ionization in LAr.

EM Calorimeters

The ATLAS LAr electromagnetic calorimeter was chosen to have an accordion geometry to minimize capacitance in the detecting elements. It is split into a barrel part covering $|\eta| < 1.475$, and two end-caps covering $1.375 < |\eta| < 3.2$. The accordion design allows modules to have multiple layers in depth, with varying granularity ($\Delta\eta \times \Delta\phi$). Layouts of segments from the barrel and end-cap EM calorimeters are shown in Fig. 1.6. A detailed sketch of a barrel EM module and its constituent layers is shown in Fig. 1.7. All components are placed into cryostats at a temperature of approximately 86° K [4]. The design and size of the EM calorimeter provides a total thickness of at least 22 radiation lengths (X_0). One X_0 represents the average distance an electron must travel through a material to reduce its energy to $1/e$ of its initial energy [5]. The cumulative thickness of the calorimeter system can be seen as a function of pseudorapidity in Fig. 1.8. All EM calorimeter systems were designed and tested to have an energy resolution of $\sigma(E_T)/E_T = 10\%/\sqrt{E_T} \oplus 0.7\%$.

A typical pulse in the LAr calorimeter comes from electrons coming from ionized argon in the LAr gap.

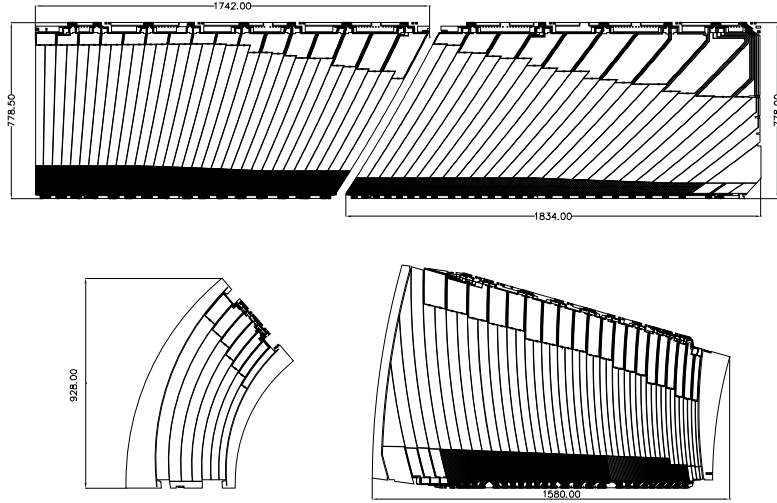


Figure 1.6: Layouts of a barrel EM module (top), inner end-cap wheel (bottom left), and outer end-cap wheel (bottom right). Figure taken from Ref. [3].

An electric field inside the gap collects the electrons and an ionization pulse is then read out and shaped. An ionization pulse is triangular in shape has a width of ~ 450 ns [6], as can be seen in Fig. 1.9. The final pulse that is digitized has a width between 450 and 600 ns after shaping. This corresponds to roughly 18 to 24 LHC bunch crossings. During this time, there could be contributions from out-of-time events (pile-up), and various techniques such as optimal filtering [7] have been developed to minimize contributions from pile-up.

EM Barrel Calorimeter

The EM barrel, covering $|\eta| < 1.475$, consists of two half-barrels, each 3.2 meters long and weighing 57 tons. It has an inner and outer diameter of 2.8 m and 4.0 m, respectively. The calorimeter is comprised of three layers, with a thickness of at least $22 X_0$ increasing to from 22 to $30 X_0$ in the interval $0 < |\eta| < 0.8$, and from 24 to $33 X_0$ in the interval $0.8 < |\eta| < 1.3$, as seen in Fig. 1.8. In front of these three layers is a LAr presampler which is intended to recover energy lost to material in front of the EMCAL. The granularity of the EM barrel calorimeter's first layer is $\Delta\eta \times \Delta\phi = 0.025 \times 0.025$ in order to be able to perform shower shape measurements and to distinguish pairs of γ from π^0 decays with pairs of γ from H decay. The granularity of the presampler is $\Delta\eta \times \Delta\phi = 0.025 \times 0.1$.

EM End-cap Calorimeter

The EM end-cap calorimeter, covering $1.375 < |\eta| < 3.2$, consists of two wheels on each side of the EM barrel calorimeter, each 63 cm thick, with a weight of 27 tons. Each wheel of the EM end-cap calorimeter consists

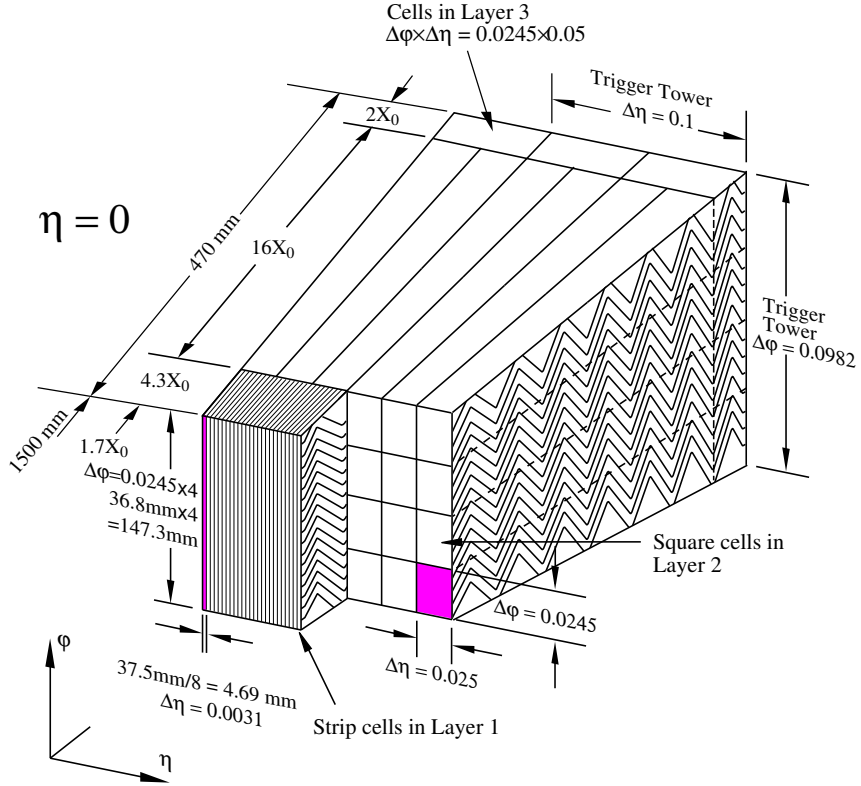


Figure 1.7: Sketch of a barrel EM module showing the different layers and their respective granularities. Radiation length (X_0) is the average distance an electron must travel through a given material to reduce its energy to $1/e$ of its initial energy. Trigger towers are sets of cells (strip or square) from which analog signals are summed for input to the L1 trigger. Figure taken from Ref. [3].

of 32 identical azimuthal sectors. Similar to the EM barrel calorimeter, the barrel end-cap calorimeter consists of three layers. It has a total thickness of at least $24 X_0$ increasing from 24 to $38 X_0$ on the outer wheel ($1.475 < |\eta| < 2.5$), and from 26 to $36 X_0$ on the inner wheel ($2.5 < |\eta| < 3.2$). Similar to the EM barrel calorimeter, the granularity of the first layer is $\Delta\eta \times \Delta\phi = 0.025 \times 0.025$ and the granularity of the presampler is $\Delta\eta \times \Delta\phi = 0.025 \times 0.1$.

Hadronic Calorimeters

The hadronic calorimeters surround the EM calorimeters and are designed to measure the energy deposited from hadrons and hadronic showers that passed through the EM calorimeters. The hadronic calorimeter is composed of Tile barrel calorimeter with a coverage $|\eta| < 0.8$, Tile extended barrel with a coverage $0.8 < |\eta| < 1.7$, and the HEC with a coverage $1.5 < |\eta| < 3.2$. Both Tile systems use steel as an absorber, with scintillator as the active material. The particle shower begins in the absorber, and scintillation light then gets transported through the wavelength shifting fiber into photomultiplier tubes where the signal is

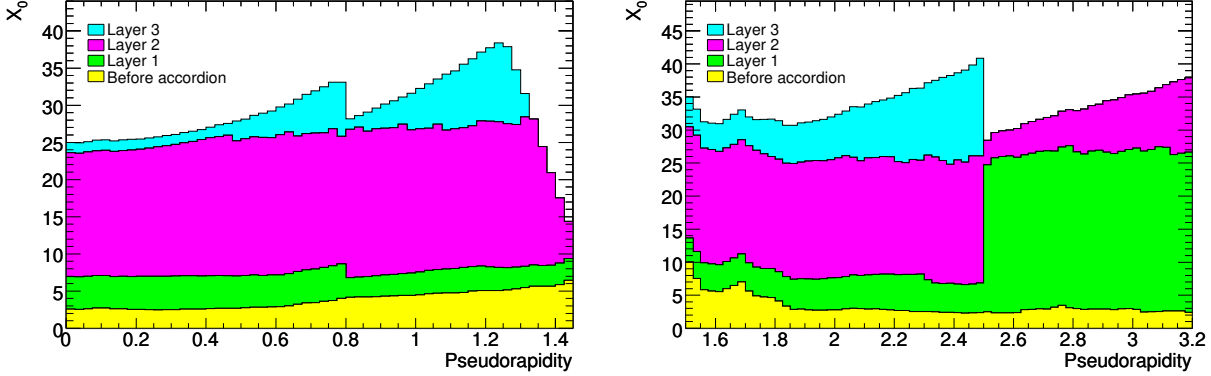


Figure 1.8: Cumulative thickness, in units of radiation length X_0 and as a function of $|\eta|$, in front of (yellow distribution) and in the electromagnetic calorimeters. Shown separately are the amounts of radiation in the various layers of the barrel (left) and end-cap (right) EM calorimeters. Figure taken from Ref. [3].

read out. The HEC is based on the same LAr technology used in the EM calorimeters, but uses copper, instead of lead, for the absorber material. The interaction length λ_I of the EM calorimeter system is small, so a proper thickness of the hadronic calorimeters is necessary to make proper measurements of high energy jets. A summary of the total interaction length of the ATLAS calorimeter system, as a function of pseudorapidity is shown in Fig. 1.10. Both TileCal and HEC calorimeters have an energy resolution of $\sigma(E_T)/E_T = 50\%/\sqrt{E_T} \oplus 3\%$.

Tile Barrel and Extended Barrel Calorimeters

The Tile barrel and extended barrel calorimeters cover $|\eta| < 0.8$ and $0.8 < |\eta| < 1.7$ respectively. The tile barrel calorimeter is 5.8 m long, the two tile extended barrels are each 2.6 m in length. Both the tile barrel and extended barrel calorimeters have an inner and outer diameter of 2.28 m and 4.25 m, respectively. They are composed of three layers with granularity of $\Delta\eta \times \Delta\phi = 0.1 \times 0.1$ for the first two layers, and the outermost layer with granularity $\Delta\eta \times \Delta\phi = 0.2 \times 0.1$. Each barrel consists of 64 modules roughly $\Delta\phi = 0.1$ in size. A schematic showing a TileCal module is shown in Fig. 1.11.

LAr Hadronic End-Cap Calorimeter

The HEC calorimeter is based on the LAr technology used in the EM calorimeter systems. The absorber material is copper, and the active material is LAr. The HEC covers a pseudorapidity region of $1.5 < |\eta| < 3.2$. The two barrels of the HEC each contain 32 modules symmetric in azimuth, with an outer radius of 2030 mm. The first two layers of the HEC have a granularity $\Delta\eta \times \Delta\phi = 0.1 \times 0.1$, while the last layer has a coarser granularity of $\Delta\eta \times \Delta\phi = 0.2 \times 0.2$.

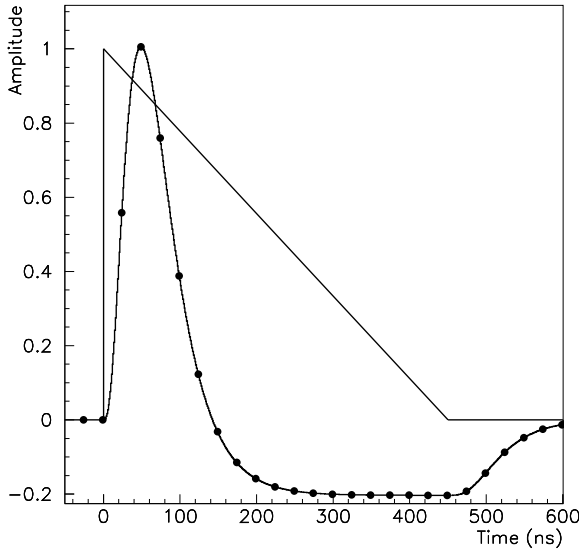


Figure 1.9: Amplitude versus time plot of a LAr calorimeter pulse before shaping (triangular). The shaped pulse is sampled every 25 ns, as indicated by the periodic points. The sampling frequency corresponds to the LHC bunch crossing frequency of 25 ns. Figure taken from Ref. [3].

Forward Calorimeter

The forward calorimeter is an important sub-system in the present analysis due to its forward pseudorapidity coverage. The calorimeter is comprised of two halves located on either side of the ATLAS detector IP, surrounded by the HEC. It covers a pseudorapidity range of $3.2 < |\eta| < 4.9$, and has a granularity of $\Delta\eta \times \Delta\phi = 0.2 \times 0.2$. While the other EM calorimeter systems use an accordion design, the forward calorimeter has electrodes oriented parallel to the beamline (z -axis) which consist of thin tubes of copper with a gap for LAr that surround rods of absorber material. These tubes are located inside the same kind of absorber material. The LAr gap is thin, about 0.25 mm in the first module, in order to increase readout time and decrease noise from ion buildup.

Each FCal is composed of three modules, as shown in the $y - z$ plane in Fig. 1.12. The first of three modules (FCal1) is the EM module and uses copper as the absorber. The last two hadronic modules (FCal2, FCal3) use tungsten as the absorber. FCal1 uses copper plates that are stacked one behind the other. These plates have 12,260 drilled holes to make space for the electrodes, which are rods made from absorber material coaxial to a thin surrounding LAr layer with precision, radiation-hard plastic fiber used for readout. A schematic of first layer of the calorimeter as it appears in the $x - y$ plane, perpendicular to the beam direction, showing the tubes of LAr inside the absorber material, is shown in the left of Fig. 1.13. Signal is read out from ionized charges in the LAr that travel to electrodes which run parallel to the tubes. The

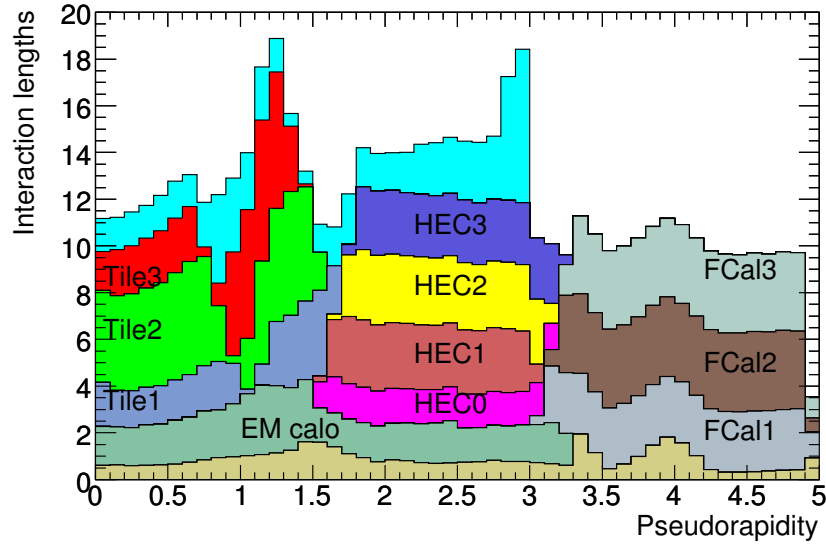


Figure 1.10: Cumulative thickness, units of interaction length (λ_I) as a function η , in front of the EM calorimeters, in the EM calorimeters themselves, in the hadronic calorimeters, and the total amount after all calorimeters. Figure taken from Ref. [3].

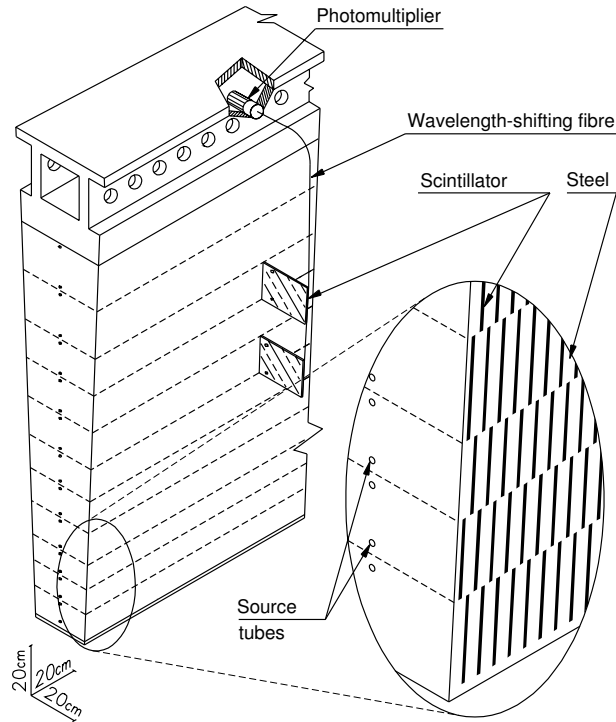


Figure 1.11: Schematic of a TileCal module, showing absorber material interspace with scintillator. Figure taken from Ref. [3].

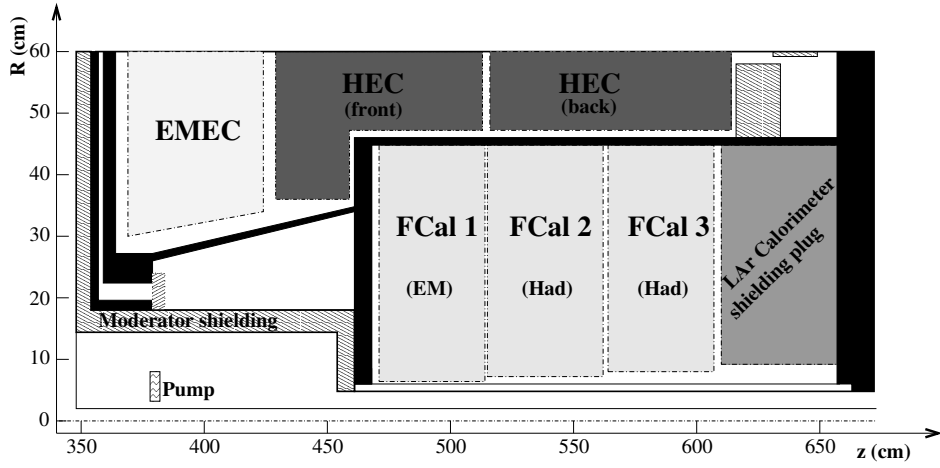


Figure 1.12: Diagram showing the three modules of the FCal. Shown in the $y - z$ plane, with the beam going in the z direction. The FCal is the most forward calorimeter in ATLAS, covering a pseudorapidity interval $3.2 < |\eta| < 4.9$. Figure taken from Ref. [3].

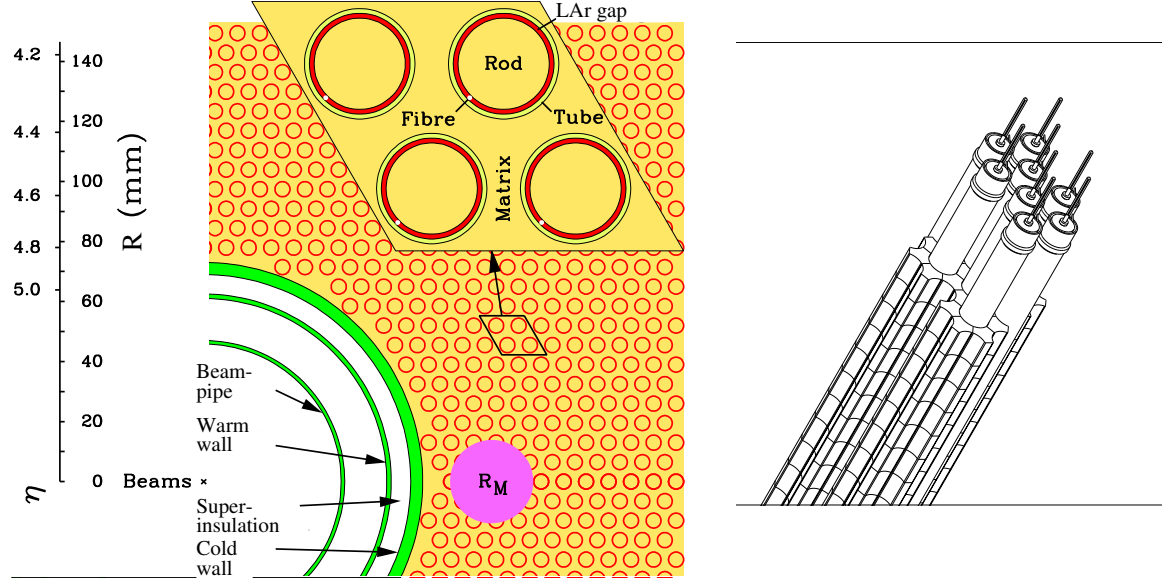


Figure 1.13: View of first FCal module (EM) as seen along the z -axis (left). Tubes of LAr inside absorber material. Shown is one Moliere radius R_M , which is the radius of a cylinder that would contain 90% of the radiation inside a calorimeter. A schematic of the tungsten rods, enclosed in copper and a LAr gap, all surrounded by tungsten slugs (right). The design is used for the two hadronic FCal modules FCal2 and FCal3. Figures taken from Ref. [3].

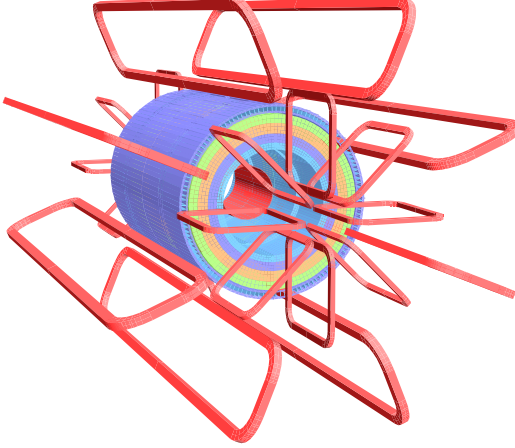


Figure 1.14: The ATLAS magnet system. Shown is the cylindrical solenoid magnet, as well as the eight barrel toroid magnets used for muon detection. Figure taken from Ref. [3].

hadronic modules FCal2 and FCal3 require large interaction lengths, which is why tungsten is chosen as the absorber material, rather than copper as in FCal1. The modules consist of two copper plates, 2.35 cm thick, that have many tungsten rods, coaxial to copper tubes with a LAr gap, enclosed in tungsten slugs, as shown in right of Fig. 1.13. These modules give a total of $10 \lambda_I$ interaction lengths. The FCal has an energy resolution of $\sigma(E_T)/E_T = 100\%/\sqrt{E_T} \oplus 10\%$.

1.2.3 Solenoid Magnet

The magnet system, shown in Figure 1.14 has an overall dimension of 22 m in diameter and 26 m in length. It stores a total energy of 1.6 GJ and consists of a barrel solenid magnet, and toroidal magnets used by the muon system. The toroidal magnets are not used in the present analysis. The solenoid magnet, which is used by the inner detector tracker, provides a 2 T axial field which is supplied by a 7.73 kA current. NbTi is used as a conductor and is supercooled by a LAr cryostat temperatures down to 4.5 K.

1.2.4 Inner Detector

The ATLAS Inner Detector (ID) is responsible for tracking, which is the precise determination of the position of charged particles. In an average collision there can be thousands of particles, which, in the presence of a magnetic field, will curve. If their positions are well known and can be distinguished, the particles momentum can be calculated. The ID is designed to provide precision tracking for particles above a p_T threshold of 0.5 GeV, although some studies have had similar performance with particle p_T as low as 0.1 GeV. The ID is designed to have a transverse momentum resolution of $\sigma(p_T)/p_T = 0.05\%/\sqrt{E_T} \oplus 1\%$.

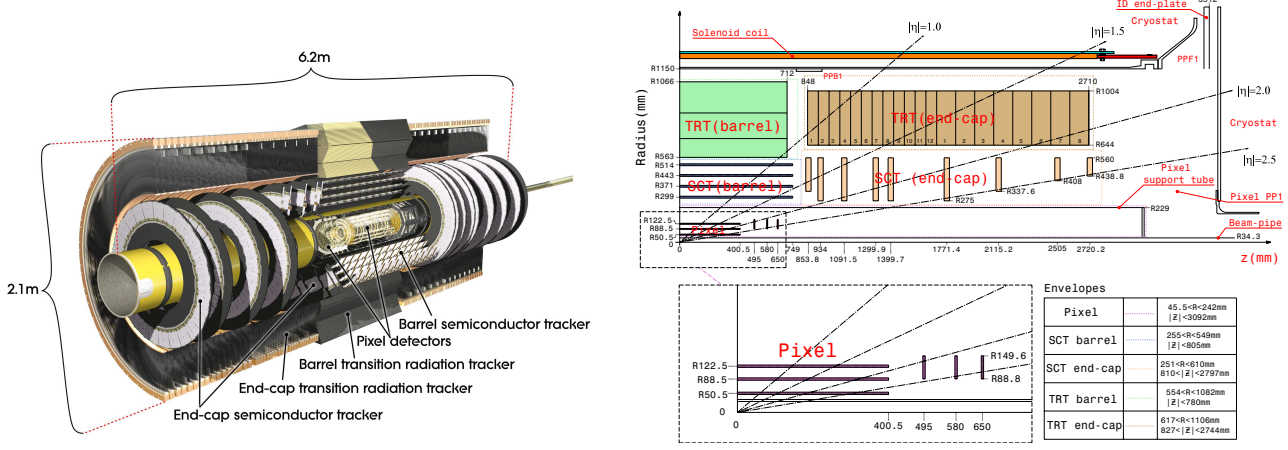


Figure 1.15: Cut-away picture (left) and schematic (right) of the ATLAS Inner Detector. Figures taken from Ref. [3].

Tracking is a very important part of every high energy particle detector, and is usually placed closest to the interaction point of a detector. A cut-away and schematic of the ID is shown in Fig. 1.15. The detector sits inside the 2T magnetic field produced by the solenoid. The ID has a rapidity coverage of $|\eta| < 2.5$ and has an outer radius of 1.15 m. There are three main subsystems that comprise the ID, listed outwards from the beam pipe: the pixel detectors, the semiconductor tracker (SCT), and the transitional radiation tracker (TRT).

The pixel layer has the highest granularity out of the ATLAS tracking subsystems. There is a barrel layer and two end-cap layers, one on each side of the IP. The barrel detector has three concentric layers located 50.5mm, 88.5mm, and 122.5 mm radially away from the beam pipe. The end-caps also have three layers located 495mm, 580mm, and 650mm in the transverse direction on each side of the interaction point. All of the pixel subsystems have a granularity of $50 \times 400 \mu\text{m}^2$ and total approximately 80 million readout channels. The SCT has roughly 6.3 million channels and consists of four concentric barrel layers, and nine disks on each side of the IP. The accuracy of the barrel and end-cap regions is $17 \mu\text{m}$ in the $(R\phi)$ plane and $580 \mu\text{m}$ in the radial direction. The TRT, which is a drift tube (straw) detector, is the outermost tracking layer of the ID. It has a total of approximately 351,000 channels (one per straw) and an accuracy of $130 \mu\text{m}$ per straw tube. However, during HI running, the occupancy in the TRT is usually too large to use effectively.

Chapter 2

Theoretical Introduction

2.1 Quantum Chromo-Dynamics

Quantum Chromo-Dynamics (QCD) is a relativistic non-abelian gauge theory, with symmetry group $SU(3)$, which describes the strong interaction between quarks and gluons. Quarks are charged subatomic particles that are the fundamental constituents of matter and gluons are gauge bosons that are mediators of the strong interaction between quarks. In its form, QCD appears similar to QED [8], however, since the gluons of the strong force carry color charge, solutions to the QCD Lagrangian become more complicated. The QCD Lagrangian [9] is

$$\mathcal{L} = \bar{\psi}_i (i\gamma^\mu \partial_\mu - m_i) \psi_i - g \bar{\psi}_i \gamma^\mu t_{ij}^a \mathcal{A}_\mu^a \psi_j - \frac{1}{4} F_a^{\mu\nu} F_{\mu\nu}^a, \quad (2.1)$$

where ψ is the spin-1/2 quark field (quark), m_i is the quark mass, \mathcal{A}_α^A is the spin-1 gluon field (gluon), t_{ij}^a is a generator from the fundamental representation of the $SU(3)$ group which describes the interactions between quark and gluon fields. The field strength tensor $F_a^{\mu\nu}$ is derived from \mathcal{A}_α^A ,

$$F_{\mu\nu}^a = \left[\partial_\mu \mathcal{A}_\nu^a - \partial_\nu \mathcal{A}_\mu^a - g f^{abc} \mathcal{A}_\mu^b \mathcal{A}_\nu^c \right] \quad (2.2)$$

where the indices a , b , and c sum over the eight color degrees of freedom of the gluon field and f^{abc} are the structure constants of the $SU(3)$ color group. The term $g = \sqrt{4\pi\alpha_S}$ is related to the strong force coupling constant α_S .

In 2.1, the left-most term, $\bar{\psi}_i (i\gamma^\mu \partial_\mu - m_i) \psi_i$, is the Dirac equation describing a free particle. To account for interactions with the field, additional terms are present. The middle term, $g \bar{\psi}_i \gamma^\mu t_{ij}^a \mathcal{A}_\mu^a \psi_j$, describes the coupling between quarks and gluons, and the last part of the Lagrangian, $\frac{1}{4} F_a^{\mu\nu} F_{\mu\nu}^a$, is the kinetic term from the gluon field.

The third term, $f^{abc} \mathcal{A}_\mu^b \mathcal{A}_\nu^c$, in the field strength tensor $F_a^{\mu\nu}$, is the non-abelian term that distinguishes QCD from QED. This gives raise to three- and four-point gluon vertices, resulting in the three basic vertices

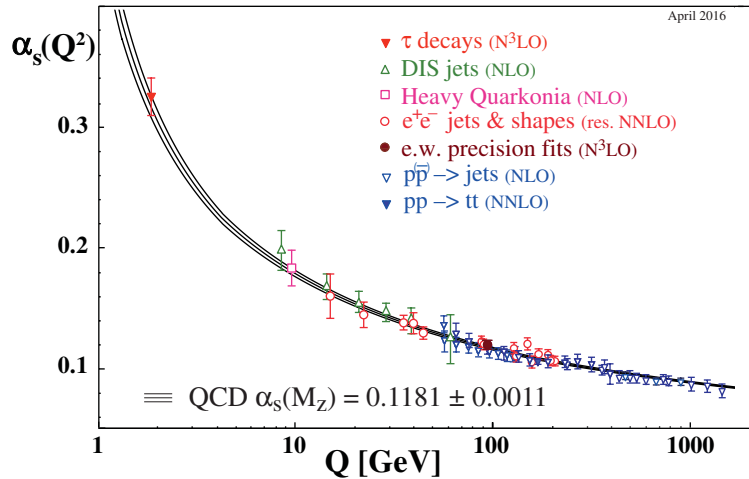


Figure 2.1: Strong force coupling constant $\alpha_S(Q^2)$, which decreases with increasing four-momentum transfer $Q = \sqrt{|q^2|}$. Figure taken from Ref. [10].

of QCD, shown in Figure 2.2.

A consequence of gluon self interactions in QCD is the fundamental property of asymptotic freedom: the fact that the strong force coupling constant $\alpha_S(Q^2)$ decreases with increasing energy scales, or by the uncertainty principle, smaller distances. The four-momentum transfer $Q = \sqrt{|q^2|}$, where q is the four momentum of a virtual particle responsible for an interaction, determines the energy and distance scales ($d \sim 1/Q$) probed. Asymptotic freedom also explains the interpretation that quarks and gluons are point-like particles since the distances probed inside the proton can be arbitrarily small. The behavior of α_S at larger distances, or smaller energies shows a rapid increase in the coupling between quarks and gluons. A direct

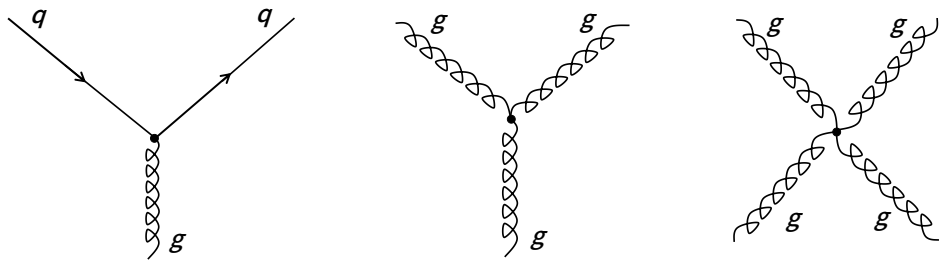


Figure 2.2: Three types of QCD vertices: the basic quark-gluon QCD vertex (left), three-gluon self interaction (center), and four-gluon self interaction (right).

consequence of this is that particles which interact via the strong force are highly confined: they cannot exist freely at macroscopic distances. Only color singlet states - quark-antiquark pairs (mesons) and three quark states (baryons) exist stably [8]. The behavior of α_S is shown from various measurements as a function of four-momentum transfer Q in Fig. 2.1.

There have been several techniques developed for performing QCD calculations. The two established methods are perturbative QCD (pQCD) [11] and lattice QCD [12]. Lattice QCD is used predominantly for calculations at lower energies where Q^2 is small and α_S is large. These calculations are performed below the characteristic QCD scale $\lambda_{QCD} \sim 200$ MeV, where $\alpha_S \sim 1$. Lattice QCD calculations have been successful in describing experimental data on the properties of nucleons, such as their mass [13]. Additionally, these computationally intensive calculations support experimental evidence of a new state of matter that exists at high temperatures and densities called the Quark Gluon Plasma (QGP) [14, 15, 16, 17, 18]. If the Q^2 of a system is above λ_{QCD} , meaning α_S is sufficiently small, pQCD calculations can be used because an order-by-order expansion of the Lagrangian in powers of α_S is appropriate. In this high Q^2 regime, individual quarks or gluons in the nucleus can be resolved. Whereas, in the low Q^2 regime, where lattice QCD calculations are used, only individual nucleons and not their constituents can be observed. The measurement presented in this dissertation will rely on tools that were developed to work at energy scales where pQCD calculations can be used.

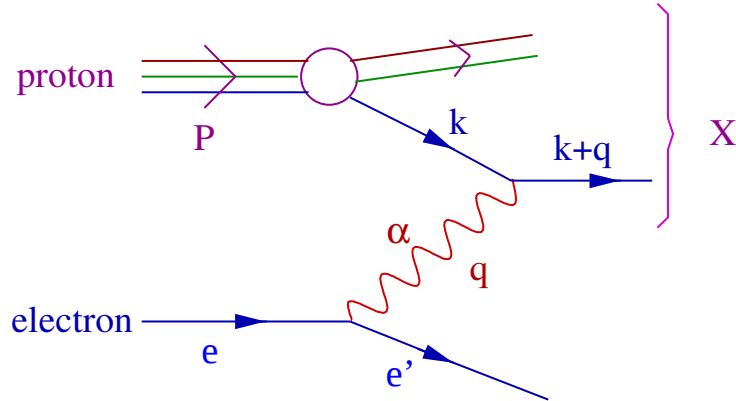


Figure 2.3: The DIS process that takes place in $e^\pm p$ collisions with an exchange via a virtual photon γ^* . Figure taken from Ref. [19].

2.2 Deep Inelastic Scattering

The proton, the fundamental building block of nuclear matter in nature, is a fermion with one positive unit of electric charge, a spin of $1/2\hbar$. However, much more has been discovered about its fundamental properties and constituents in recent years. Almost half a decade ago the so called *naive parton model* [20, 21] of the proton was proposed: the proton was made out of non-interacting point-like constituents called partons, which were thought to be charged fermions, possibly bound together by some other neutral particles. This model was first supported by evidence from through lepton-nucleon Deep Inelastic Scattering (DIS) experiments from the SLAC-MIT collaboration [22]. Commonly, this was done with an electron and a proton, with incoming four-momenta e and P , respectively, and a virtual photon with four-momentum q acting as the exchange particle. This process, $ep \rightarrow eX$, where X are the remnants of the proton, is shown in Fig. 2.3. From these quantities, we define two important variables in DIS, the first is the proton longitudinal momentum fraction carried by its constituent parton, *Bjorken-x*

$$x = \frac{Q^2}{2P \cdot q} = \frac{Q^2}{2M\nu}, \quad (2.3)$$

where ν is the energy of the virtual photon in the proton rest frame. The second variable is the lepton momentum fraction of the lepton transferred to the proton

$$y = \frac{P \cdot q}{P \cdot l} = \frac{\nu}{E}, \quad (2.4)$$

where E is the energy of the lepton in the proton rest frame. The resolving power of the photon goes as $R^2 \sim 1/Q^2$, meaning that for the proton, with a proton radius of $R_p \sim 8$ fm, if $Q^2 \equiv -q^2 \ll 1$ (GeV/c) 2 , the photon will interact elastically with the proton nucleus as a whole. If $Q^2 \equiv -q^2 \gg 1$ (GeV/c) 2 , the photon will interact inelastically with the proton, and will probe its individual constituents, partons. This inelastic scattering regime, where energy is transferred from the photon to the proton, $Q^2 \gg 1/R_p^2 \sim 1$ (GeV/c) 2 corresponds to $Q^2 \gg m_p^2$, where $m_p \sim 1$ (GeV/c) 2 is the proton mass. This puts a minimum requirement on Q^2 to effectively disassemble the proton and is the region of phase-space where DIS occurs. This is usually named as the boundary to the inelastic scattering regime. However, to avoid the creation of purely resonant states, a second criteria is often the energy of the hadronic final state. Thus, in some QCD global analysis, $Q^2 > 4$ GeV is chosen as the boundary.

The sub-structure of hadrons in DIS can be parameterized by so called structure functions $F_1(x, Q^2)$ and $F_2(x, Q^2)$ [23], which are distribution functions describing the structure of a baryon. Using a linear combination of the two structure functions

$$F_L(x, Q^2) = F_2(x, Q^2) - 2x F_1(x, Q^2), \quad (2.5)$$

the DIS cross section can be parameterized as

$$\frac{d^2\sigma}{dx dQ^2} = \frac{2\pi\alpha_S^2}{xQ^4} [(1 + (1 - y)^2)F_2(x, Q^2) - y^2 F_L(x, Q^2)]. \quad (2.6)$$

As introduced above y is the fractional energy loss of the lepton and is usually small in most of the kinematic plane. The majority of experiments impose a cut of $y < 0.8$ to keep QED radiative corrections small. As a result, F_L can be neglected leaving only the contribution from F_2 . In fact, the structure function F_L is only measured where Q^2 is close to the so called kinematic limit [8], which is $Q^2 < (p + l)^2$.

2.3 Parton Distribution Functions

The DIS interaction through a photon, which does not couple to gluons, first assumed that the F_2 structure function purely described quark distributions. In the naive parton model, the point-like nature of the proton constituents implied there is no cutoff on the distances that can be probed, meaning there should not be a dependence on Q^2 . This meant that the F_2 structure function can be rewritten with no Q^2 dependence purely as the sum over flavors of quark and antiquark parton distribution functions (PDFs) $q_i(x)$ and $\bar{q}_i(x)$

$$F_2(x, Q^2) \sim F_2(x) = \sum_i e_i (x q_i(x) + x \bar{q}_i(x)), \quad (2.7)$$

where e_i is their respective charge. The PDFs are probability density functions representing the probability of finding a quark with flavor i having a longitudinal momentum fraction x and $x + dx$. Therefore, $x q_i(x)$ is the number of quarks with flavor i that have a longitudinal momentum fraction x between x and $x + dx$. The results of F_2 structure function data are shown in Fig. 2.4 [24, 25, 26, 1, 27], where a lack of Q^2 dependence, called Bjorken scaling [28], is seen for $x > 0.1$. However, experiments that probed lower x saw a non-linearity, or a scaling violation, of F_2 with changing Q^2 .

The linearity of the F_2 structure function was proposed based on the assumption that protons constituents are non-interacting. This ignores QCD radiative processes, the process in which quarks interact with and radiate gluons. Probing the proton at low energies, the picture is one of three partons - two up quarks and a down quark as shown on the left of Fig. 2.5. These so called valence quarks are strongly interacting and are held together by gluons. However, at smaller distances and shorter timescales, the picture of the proton

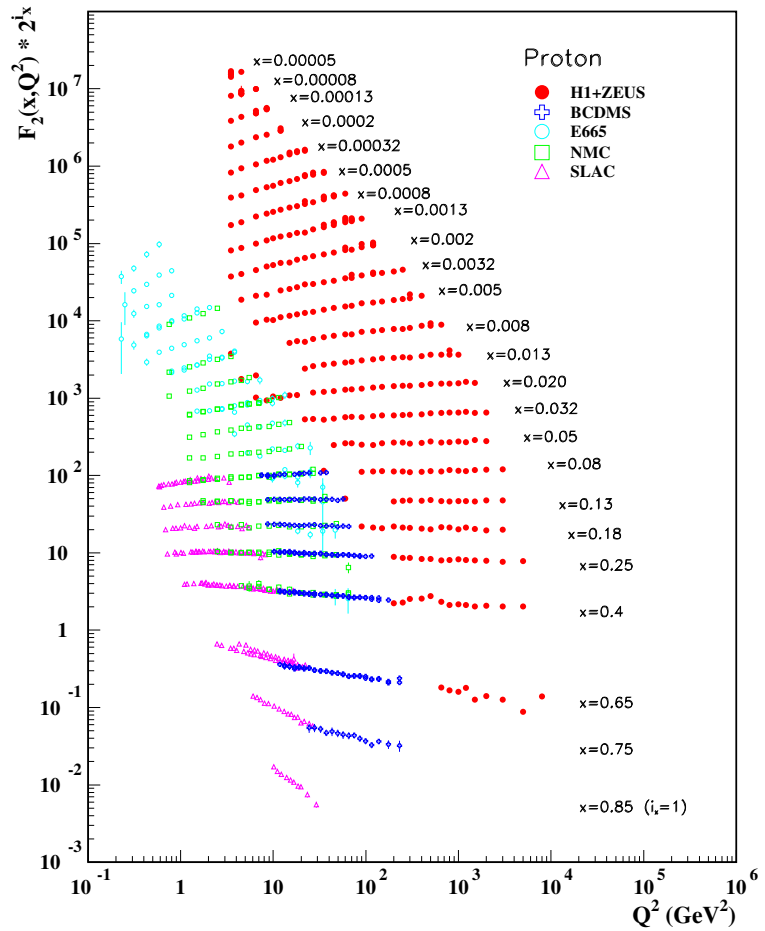


Figure 2.4: Summary of F_2 structure function data plotted as a function of Q^2 for different values of x . Figure taken from Ref. [10]

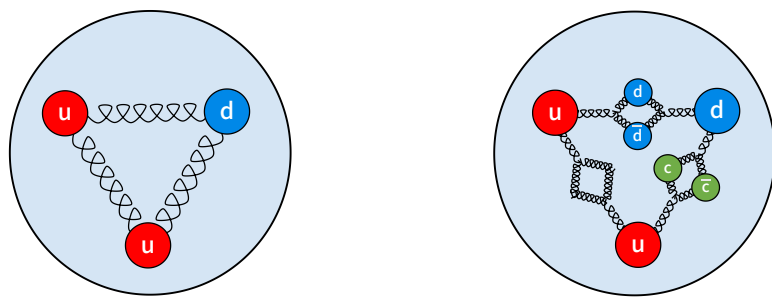


Figure 2.5: A simple picture of the proton, with three quarks connected by three gluons (left). At shorter timescales, quantum fluctuations exist and the proton picture becomes more complex (right).

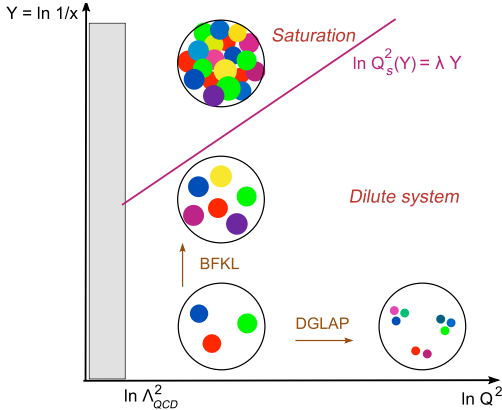


Figure 2.6: Schematic showing the BFLK evolution in $\ln(1/x)$ and DGLAP evolution in $\ln(Q^2)$ (left figure). The saturation scale Q_S is represented by the diagonal line.

becomes more complicated, as seen on the right of Fig. 2.5. In this regime, gluons can be seen splitting into short lived quark-antiquark pairs (sea quarks), or into gluon-gluon pairs. Additionally, it was found that the total momentum contribution of all quarks inside the proton, when the quark PDFs are integrated over a wide range of x , was roughly 50% [9]. All this information strongly suggested the possibility that gluons carry a significant momentum fraction of the proton, depending on the x and Q^2 of the interaction. The inclusion of gluons into the nucleus wavefunction is what gave rise to the scaling violation seen in the various experiments at lower- x . As a result, the PDFs for quarks and gluons have to be expressed as a function of x and Q^2 : $q_i(x, Q^2)$ for quarks and $g_i(x, Q^2)$ for gluons. This new picture of the proton is sometimes called the *improved parton model* or just the parton model, for brevity.

In the regime where pQCD can be used ($\alpha_S > \lambda_{QCD}$), techniques have been developed to describe the evolution of PDFs both with x and Q^2 . The Dokshitzer-Gribov-Lipatov-Altarelli-Parisi (DGLAP) equations [29, 30, 31, 32] describe the evolution of PDFs as a function of $\ln(Q^2)$, at a fixed x . The other set of equations, describing the PDF dependence on $\ln(1/x)$ at fixed Q^2 , are the Balitsky-Fadin-Kuraev-Lipatov (BFLK) evolution equations [33, 34, 35, 36]. These sets of equations describing the evolution of parton densities in Q^2 and x are considered to be the most fundamental equations in pQCD. The BFLK equation will be of particular interest to this thesis because of its role in evolving PDFs to low- x . A schematic representation of the BFLK and DGLAP evolutions in the $\ln(1/x)$ vs $\ln(Q^2)$ phase-space is shown in 2.6.

Over time, global QCD analysis of structure functions in deep inelastic lepton-nucleon scattering at HERA, as well as jet and hadron cross sections at the LHC, Tevatron, and RHIC were performed in a wide kinematic range, providing several new sets of PDFs with the highest degree of precision reached so far [38, 39, 40, 37]. Examples of quark and gluon PDFs from DIS experiments at different Q^2 from the

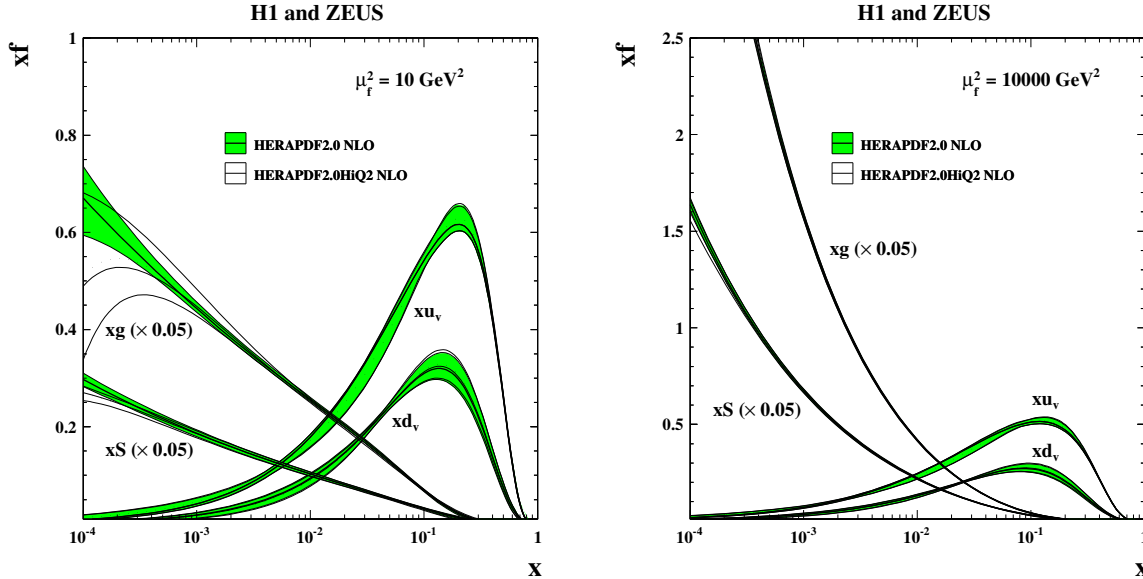


Figure 2.7: PDFs obtained at different Q^2 by the H1 and ZEUS collaborations. The gluon PDFs are scaled so they would fit on the plots with the quark PDFs. Note that the observable plotted is $xq_i(x, Q^2)$. Figure taken from Ref. [37].

H1 and ZEUS collaborations are shown in Fig. 2.7. These global QCD analyses show that the $g(x, Q^2)$ found to rise rapidly at small x in the proton. The rapidly increasing $g(x, Q^2)$ at $x \ll 1$ is explained by gluon radiation (bremsstrahlung) of soft gluons, where a parton with high- x collinearly emits a gluon with an $x_1 \ll 1$ and with small p_T . This process is shown in Fig. 2.8 where a soft gluon radiates a softer gluon and this continues with a probability $\propto \ln(1/x)$ at each step via the BFLK evolution. Naturally, the momentum fraction x carried by some intermediate gluon in this cascade is smaller than that of its predecessors ($x \ll x_n \ll x_{n-1} \ll \dots \ll x_2 \ll x_1$). This divergent behavior of $g(x, Q^2)$ means that at small enough x , the number of gluons $xg(x, Q^2)$ will tend to infinity. However, unitarity requires that the first moment of the gluon momentum distribution remains finite. Therefore, the steep rise at low- x must change at some x value; this possible phenomenon is known as *saturation* [41]. Presently it is believed that the mechanism for saturation is gluon recombination ($g + g \rightarrow g$), which is expected to happen at the saturation scale $Q_s(x)$ when the gluon wavefunctions begin to overlap due to very high gluon densities [42]. Gluons with $p_T < Q_S$ are said to be at saturation since their densities do not grow anymore. The phenomenon of saturation, which is the main focus of this thesis, will be discussed in more detail later in this chapter. First, it is informative to learn about some of the tools that can possibly be used to probe this effect.

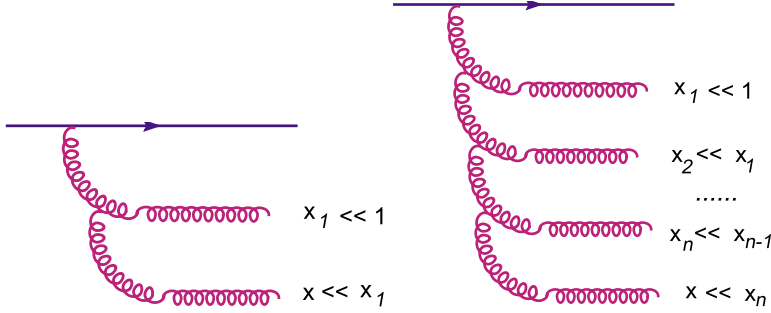


Figure 2.8: Graphic representation of BFKL evolution leading to high gluon densities at low- x . Figure taken from Ref. [19].

2.4 Hadronic Collisions and Jets

The DIS experiments successfully showed the scaling violation of the linearity of F_2 with Q^2 with smaller- x and provided precise PDFs for quarks. Indirect measurements of the gluon distribution from F_2 data were still carried out, but the precision on $g(x, Q^2)$ was limited because the photon cannot couple with gluons. Fortunately, collisions involving hadrons with hadrons, or hadrons with heavy ions open up the possibility of a hard scattering via gluon, analogous to the interaction via photon in DIS. Since gluons can couple to other gluons, hadronic collisions can be used as direct probes of $g(x, Q^2)$, providing measurements of the gluon distribution with much higher precision than in DIS. In a collision between two protons, modelled $P_A + P_B \rightarrow q_1 + q_2$ and shown in the left of Fig. 2.9, the cross section for a hard scattering process can be written [9]

$$\sigma(P_1, P_2) = \sum_{i,j} \int dx_1 dx_2 f_i(x_1, \mu^2) f_j(x_2, \mu^2) \sigma_{ij}(p_1, p_2, \alpha_S(\mu^2), Q^2/\mu^2), \quad (2.8)$$

where P_1 and P_2 are the four-momenta of the incoming protons, $p_1 = x_1 P_1$ and $p_2 = x_2 P_2$ are the four momenta of the partons participating in the interaction. The quark and gluon PDFs are f_i and f_j , the QCD scattering cross section for partons of type i and j is σ_{ij} . The hard scattering scale Q^2 is determined experimentally and places a lower limit on the possible final state particles that are produced. As discussed previously, at sufficiently high Q^2 , α_S becomes small, and the cross section can be calculated perturbatively in a series of α_S . The factorization scale μ^2 is an arbitrary parameter that places an energy threshold on what physics is considered part of the hadron wavefunction and what physics is part of the scattering process and can be considered in the hard scattering cross-section. The dependence on μ^2 gets smaller by including more terms in the perturbative expansion of the cross section calculation (which requires more computing power). In general, the factorization scale should be chosen to be $\mu^2 \sim Q^2$.

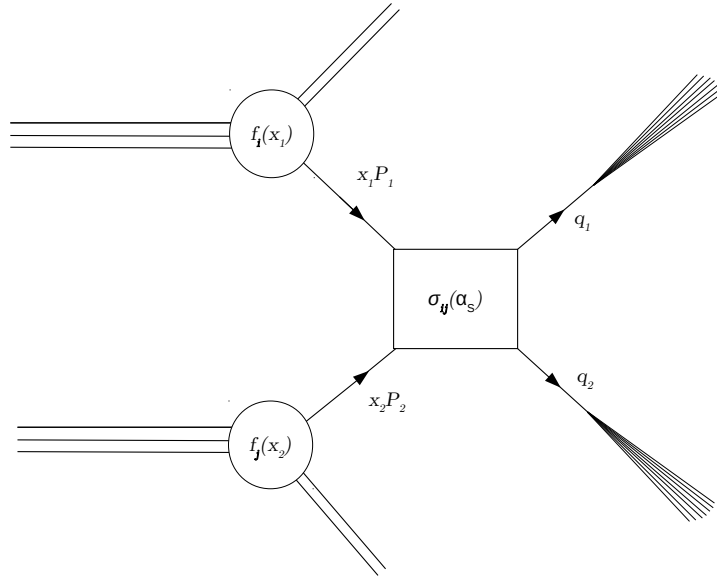


Figure 2.9: Diagram of a hadronic collision ($P_A + P_B \rightarrow q_1 + q_2$) between two protons, producing two outgoing partons, which are represented in their final state as a stream of particles. The box represents the hard scattering process.

A particle collision with sufficiently high energy transfer can result in a quark or gluon being ejected from the hadron in which it was confined. From the properties of confinement, a parton cannot exist alone at macroscopic distances, meaning a quark or gluon cannot be directly observed in a detector. The DGLAP formalism describes the evolution of the ejected parton from the hard scale until the perturbative limit λ_{QCD} . From QCD rules, as the distance of the exiting parton from its scattering event begins to increase, the probability for radiating collinear gluons will increase. These radiated gluons can in turn split into quark antiquark pairs, which can radiate more gluons, and so forth. The quarks and antiquarks from the resulting cascade then recombine into color singlet states of particles collinear with the original parton. This process, known as *hadronization*, produces a narrow cone of particles called *jets* [43, 44, 45]. The creation of these final state particles that make up a jet is described by phenomenological models, since at every level in the hadronization process, the energy of the newly created partons decreases until perturbative methods can no longer be applied. Many of these newly created particles have a lifetime sufficiently long enough for them to reach and create a signal in a detector. In this sense, a jet is a manifestation of a parton that was knocked out in a scattering event, however the precise definition of a jet depends on the procedure with which it is reconstructed. An example of an actual event from ATLAS where two jets (dijets) were created and reconstructed is shown in Fig. 2.10.

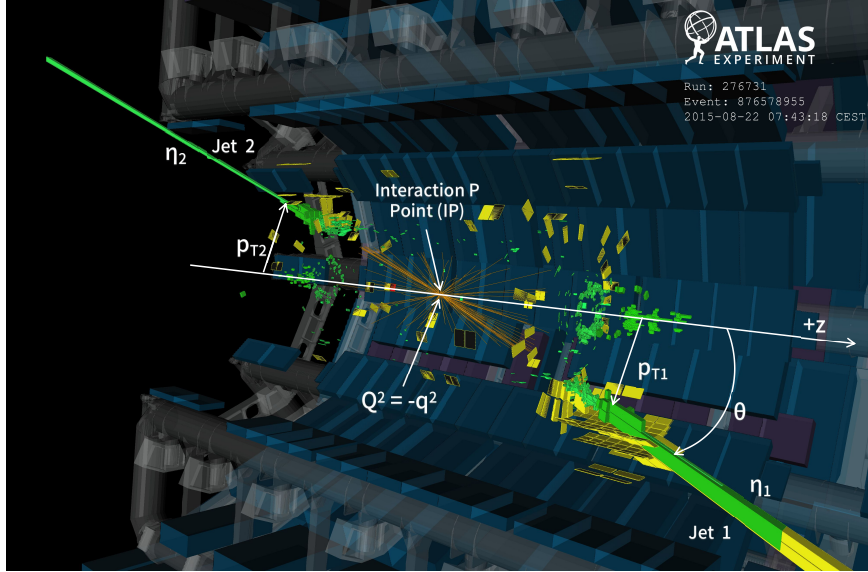


Figure 2.10: Event display from a real ATLAS dijet event. Shown are two back-to-back jets, which are manifestations of the quarks involved in a hard scattering at the interaction point, which is labeled in the figure.

2.4.1 Anti- k_t Jets

Before a jet's energy and position can be correctly described, a prescription of what a jet is must be agreed upon. A jet can have many constituents, which are final state particles produced in the hadronization process. These particles can be physically detected and used as input into clustering algorithms that aim to describe jets consistent with theory predictions [46, 47, 48, 49]. While different algorithms have their advantages and disadvantages, the anti- k_t algorithm [50] has grown in popularity since its introduction almost a decade ago. Besides its fast computation speed, the main advantage of the anti- k_t algorithm is its infrared and collinear safety (IRC) from effects of soft radiation.

Any jet clustering algorithm needs to accept a set of homogeneous input data (objects) such as the four-momenta of particles, calorimeter tower energies, topological calorimeter cells, etc. The treatment of these input objects by the algorithm is identical. The anti- k_t algorithm comes from a broader family of k_t clustering algorithms that appear the same in their formalism but yield different results based on an important parameter that will be discussed shortly. The general form of any k_t algorithm involves a collection of input objects with indexes i having energy and spatial coordinates $(\eta_i, \phi_i, p_{T_i})$ where η_i , ϕ_i , and p_{T_i} are the objects pseudorapidity, azimuthal angle, and transverse momentum, respectively. Between any two objects i and j , two distances are defined in terms of energy and position:

$$d_{iB} = -p_{T_i}^{2p} \quad (2.9)$$

$$d_{ij} = \min(p_{T_i}^{2p}, p_{T_j}^{2p}) \frac{\Delta R}{R^2} \quad (2.10)$$

where $\Delta R^2 = (\eta_i - \eta_j)^2 - (\phi_i - \phi_j)^2$, R is the characteristic radius parameter describing the maximum allowed radius of a jet, and the parameter p is what determines which type of k_t algorithm is used. The general prescription for any k_t algorithm is as follows:

1. Out of the list of objects, calculate all distances d_{ij} and d_{iB} .
2. Identify the smallest distance out of d_{ij} and d_{iB} .
3. If the minimum is d_{ij} , combine the four-momenta of the i^{th} and j^{th} objects, return to the first step, and begin again.
4. If the minimum is d_{iB} , save object i as a jet and remove it from the list of objects. Then return to the first step and begin again.
5. Continue this process until the list of objects is empty.

The behavior of all the k_t algorithms with respect to soft radiation is the same for any $p < 0$ but the focus is going to be on the case of $p = -1$, which is the parameter used in the anti- k_t jet reconstruction algorithm mentioned earlier. To understand the general idea of how it works, it is useful to begin with an ensemble several high p_T (hard) objects, and many low p_T (soft) objects used as an input to the algorithm. The distance d_{ij} between a hard particle i and a soft particle j will be dominated by the hard particle i and will be smaller than the distance d_{kl} between two soft particles k and l . This means that soft objects will cluster with hard objects preferentially over other soft objects. If the hard object i has no other hard object within a distance of $2R$, all soft objects within a circle of radius R will simply cluster with object i and eventually form a perfectly conical jet of radius R . If there are two had particles with $\Delta R < R$, then they will be combined to form a jet of radius R around the higher p_T object. If object i has another hard object within $R < \Delta R < 2R$, the object with higher p_T will form a perfectly conical jet of radius R , and the object with lower p_T will form a jet an area clipped by its neighbor with higher p_T . In reality, it does not matter what object is hard or soft, the algorithm takes a list of objects as input, naturally performs the clustering of these objects according to its prescription, and outputs a collection of jets. An example of the same input data run through different jet reconstruction algorithms is shown in Fig 2.11. The anti- k_t algorithm was adopted by ATLAS as a standard way to describe jets due to its IRC safety, fast performance, and robust treatment of various kinds of input datasets.

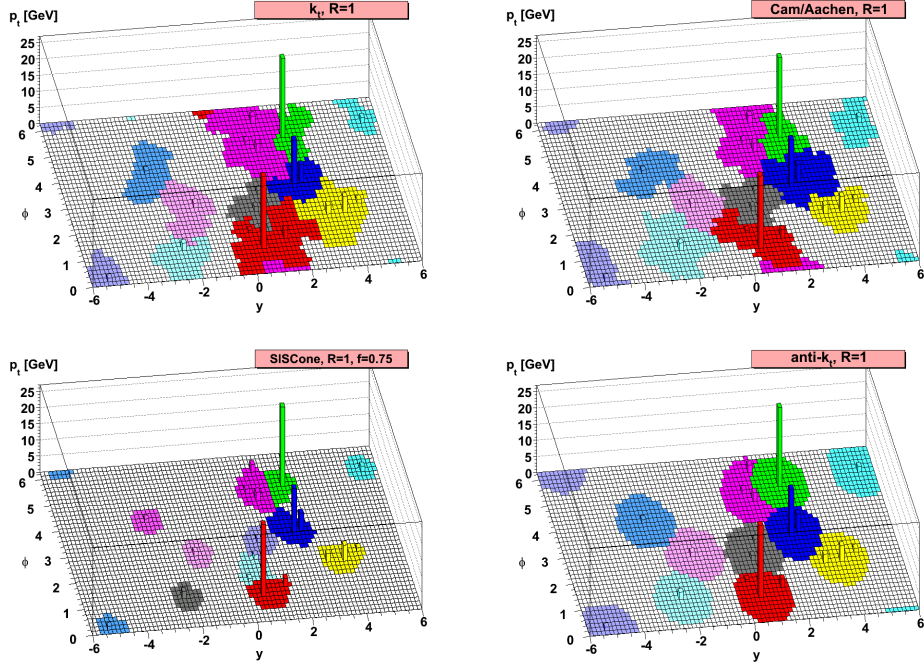


Figure 2.11: Results of jet reconstruction by the k_t (top left), Cambridge Aachen (top right), SIScone (bottom left), and anti- k_t (bottom right) algorithms on identical input sets with a jet radius requirement of $R = 0.1$. Figure taken from Ref. [50].

2.5 Gluon Saturation

The search for the onset of saturation was first pursued with $d + \text{Au}$ collisions at RHIC [51, 52, 53], where the sensitivity to possible saturation effects was increased due to the enhancement of the nuclear gluon density in the Lorentz-contracted heavy ion nucleus [54, 55]. More recent measurements at the LHC have been performed in the proton-going direction of $p + \text{Pb}$ collisions and at higher center-of-mass energies, allowing lower- x of the lead nucleus to be probed [56, 57, 58, 59]. The ALICE measurement of dijet azimuthal correlations at mid-rapidity did not find significant modification in $p + \text{Pb}$ collisions compared to pp collisions. The ATLAS and CMS measurements of inclusive jet production also did not find significant evidence of nuclear modification. Recently, CMS extended the search for gluon saturation to the highest gluon densities reached so far by measuring the inclusive jet cross-section in $p + \text{Pb}$ collisions at very forward rapidity using the CASTOR detector with $-6.6 < \eta < -5.2$, probing x down to 10^{-6} [60]. Comparing measured jet p_T spectra to event generators (EPOS-LHC [61], HIJING [62], and QGSJETII-04 [63]), it was found that none could describe the data over the full jet p_T spectra range, opening up the possibility for nuclear effects not described by these models. Currently, the differences between nuclear PDFs (nPDFs) and free nucleon PDFs are often understood from shadowing, anti-shadowing, and EMC effects [64, 65]. Calculating nPDFs $f_i^A(x, Q^2)$ for parton types i from F_2^A of heavy ions with atomic number A and comparing them to free

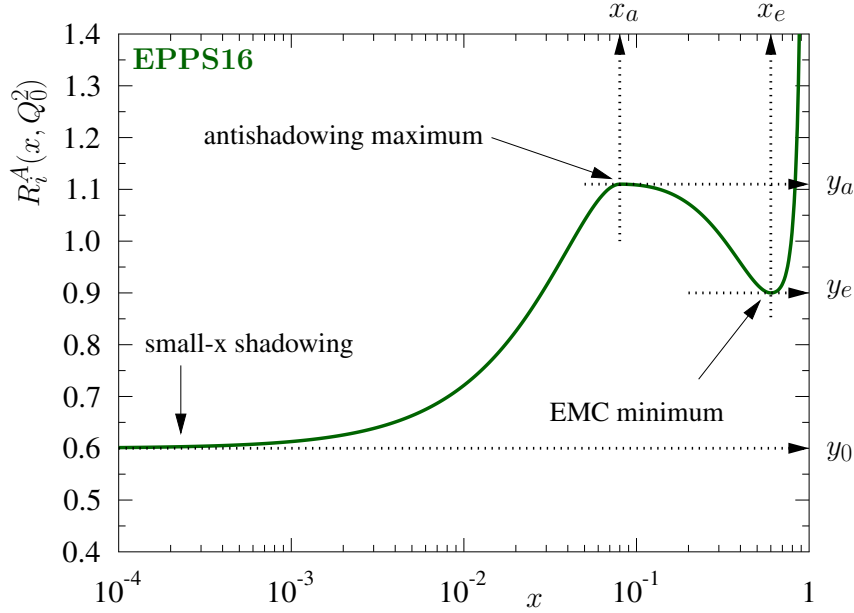


Figure 2.12: Illustration of a generalized EPPS16 parameterization of the nuclear modification factor R_i^A for different parton types i and heavy ions with atomic number A . Suppression of R_i^A by nuclear shadowing and EMC effects are prevalent at low- and high- x . Enhancement of R_i^A due to antishadowing effects are seen in an intermediate- x range. Figure taken from Ref. [64].

nucleon PDFs $f_i^p(x, Q^2)$ calculated from F_2^p is direct measure of the nuclear modification factor

$$R_i^A = \frac{f_i^A(x, Q^2)}{Af_i^p(x, Q^2)}. \quad (2.11)$$

Studies of nPDFs in heavy ion nuclei expected a scaling of free nucleon PDFs with A such that the nuclear modification factor is consistent with unity. The parameterization of R_i^A shown in Fig 2.12 indicates that the nuclear modification factor is not consistent with unity at various values of x . The suppression of R_i^A can be seen from shadowing (low- x) and EMC($x \sim 1$) effects, while enhancement of R_i^A can be seen from the antishadowing effect at $x \sim 10^{-1}$. The shadowing effect, which is of most interest to the low- x physics of this thesis, is thought to arise from screening of the nuclear parton densities by gluons on the outside of the heavy ion nucleus, which interact preferentially with any incoming probes. While this effect is not completely understood, it is well known experimentally. As discussed earlier, the large uncertainty on the gluon nPDFs and free nucleon gluon PDFs is due to the inability to directly probe gluon densities from F_2 . Additionally, final state processes can also contribute to the modification of the gluon nPDF. This opens up the possibility for additional nuclear processes to contribute to the gluon density suppression at low- x .

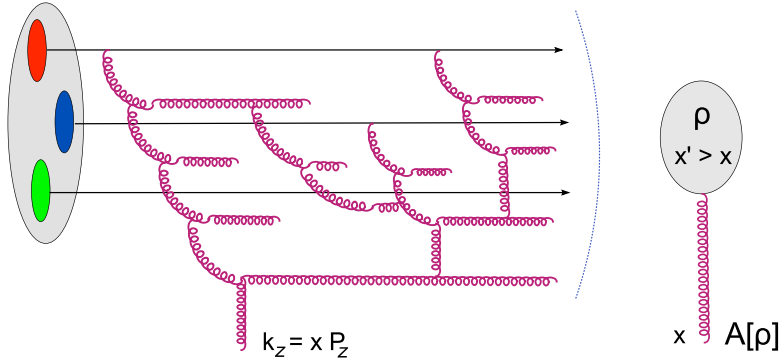


Figure 2.13: Schematic representation of the CGC theory, showing the high density, low- x gluons originating from high- x partons (left). These gluons form a gluon field $A\rho$ where the whole gluons with higher- x are represented by a color charge density ρ . Figure taken from Ref. [19].

2.6 Color Glass Condensate

One of the proposed models of gluon saturation is in the framework of the Color Glass Condensate (CGC) [66, 67, 68]. It is useful to discuss the meaning of the name: *color* comes from the fact that gluons carry a color charge, *glass* describes how short lived gluons with low- x see the surrounding higher- x gluons in the dense medium as "frozen", *condensate* describes the saturated nature of the high density gluons recombining with one another. The CGC effective theory describes a model for the interaction of a high energy parton with a highly dense gluon medium described by the BFKL evolution that includes a non-linear term responsible for gluon recombination. In the schematic shown in Fig. 2.13, a low- x gluon that originated or re-scattered from other gluons with higher $x' > x$ is emitted and interacting with this gluon is a probe of the overall gluon field $A(\rho)$, where ρ is the color charge density of the nucleon. Recently, together with non-relativistic QCD, the CGC model was able to successfully describe experimental data on the cross section of J/ψ production at ALICE [69], shown in Fig. 2.14.

A measurement probing gluon saturation in nuclear gluon densities in the framework of the CGC model was proposed by measuring possible modifications of dijet azimuthal angular distributions in $p+\text{Pb}$ and pp collisions at an x down to 10^{-5} [70]. For back-to-back dijets, the gluon field in the Pb nucleus is probed at low transverse momentum where saturation effects are expected to be large. These effects are described by whether or not an incoming parton scatters individually off each gluon in the highly dense field of the lead nucleus, or recoils against the nucleus as a whole. An away-side jet is created when a constituent gluon of this dense field is knocked out of the nucleus by the scattering incoming parton. However, due to the highly dense field, the incoming parton can scatter many times, losing energy and changing trajectory. As a result, if there are two outgoing jets, one from the scattered parton, and the other jet (away side) from a knocked

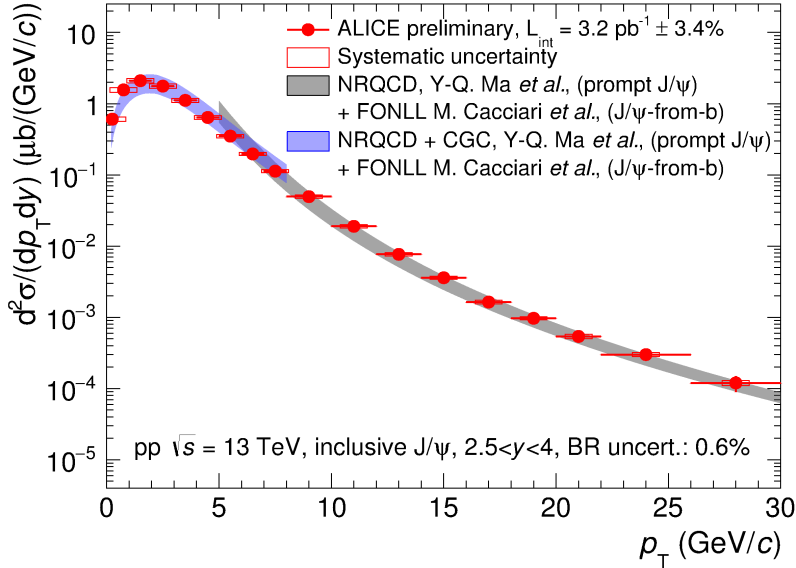


Figure 2.14: Figure taken from Ref. [69].

out gluon, they may not be perfectly back-to-back, resulting in the azimuthal broadening. The monojet signature could result from the incoming parton recoiling off the nucleus coherently [67]. The parton would not scatter with any of the individual partons, and as a result, would not produce an away-side jet. To probe these effects, one must define some observables, which will be extracted from data and presented in the latter sections of this thesis.

2.7 Measured Observables

This thesis will present a measurement of dijet production at forward rapidity with the ATLAS detector. Proton-lead collisions are studied in addition to proton-proton collisions because of the enhancement of gluon densities in the Lorentz contracted lead nucleus. At the leading order, in a collision between a proton and a heavy ion nucleus with transverse momenta p_T^P and p_T^{Pb} , respectively, with the first moving in the $+z$ (proton-going) direction, and the second in the $-z$ (lead-going) direction, we will have the following relations for parton momentum fractions x_p of the proton, and x_{Pb} of the lead nucleus

$$x_p = \frac{p_T^P e^{y_p^*} + p_T^{Pb} e^{y_{Pb}^*}}{\sqrt{s}}, \quad x_{Pb} = \frac{p_T^P e^{-y_p^*} + p_T^{Pb} e^{-y_{Pb}^*}}{\sqrt{s}}. \quad (2.12)$$

The center-of-mass rapidities ($y^* \equiv y - \Delta y$) of the outgoing partons are y_p^* and y_{Pb}^* , and Δy accounts for the rapidity shift of the center-of-mass frame of the $p+Pb$ system relative to the ATLAS laboratory frame. This shift is due to different beam energies for protons and lead nuclei in $p+Pb$ data taking. From these

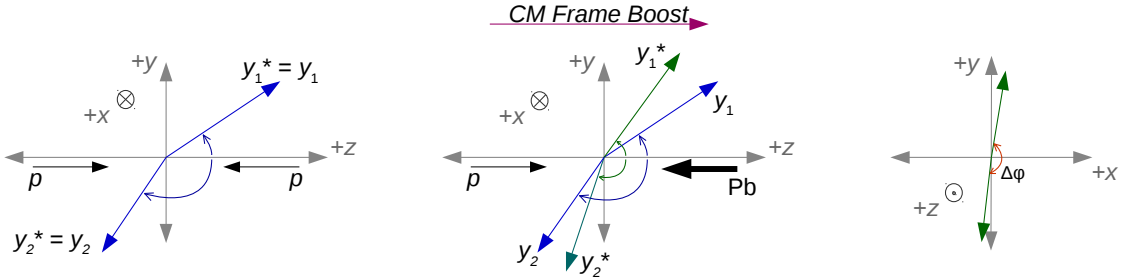


Figure 2.15: Example of a collision in the $y-z$ plane in $p\bar{p}$ where $y = y^*$ (left), a collision in the $y-z$ plane in $p+Pb$ where $y^* \equiv y - \Delta y$ (middle) to account for the boost (Δy) of the center-of-mass system, and a collision in the $x-y$ plane showing the difference in azimuthal angle $\Delta\phi$ between two jets (right).

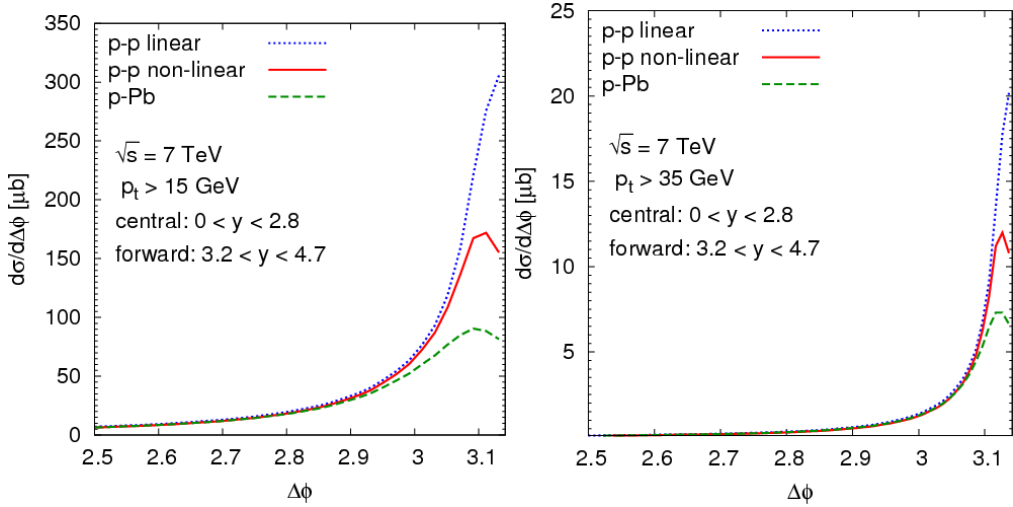


Figure 2.16: Dijet azimuthal angular correlations from theoretical models for central-forward $p\bar{p}$ and $p+Pb$ collisions as a function of $\Delta\phi$ between two jets in different p_T bins. Figure taken from Ref. [71].

equations, it is clear that to probe a lower x_2 of the lead nucleus, two forward (high y_1^* and y_2^*) particles are preferred. An example of a collision in the two systems and the difference between rapidity y and center-of-mass rapidity y^* in $p\bar{p}$ and $p+Pb$ is shown in Figure 2.15.

The final observables in this analysis are dijet azimuthal angular $\Delta\phi$ distribution widths and conditional yields of dijets. Example dijet $\Delta\phi$ distributions are shown from theoretical models in Figure 2.16. The measurement is performed in different intervals of y_1^* , y_2^* , $p_{T,1}$, and $p_{T,2}$, where y_1^* , $p_{T,1}$ is the center-of-mass rapidity and transverse momentum of the leading jet, and y_2^* , $p_{T,2}$ the center-of-mass rapidity and transverse momentum of the sub-leading jet. The leading jet, which is required to be in the forward (defined as proton-going) direction, has the highest p_T in the event, and the sub-leading jet has the second highest p_T in the event. This is a measurement of dijets probing the lowest- x of the lead nucleus at the hardest scattering scale so far. The azimuthal angular correlation functions, C_{12} , which are normalized to the number of leading

jets, are defined as

$$C_{12} = \frac{1}{N_1} \frac{dN_{1,2}}{d\Delta\phi}, \quad (2.13)$$

where N_1 is the number of leading jets, $N_{1,2}$ is the number of dijets, and $\Delta\phi$ is the lower azimuthal angle between the leading and sub-leading jets. The C_{12} distributions are fitted and their widths W_{12} defined by the root-mean-square (RMS) of the fit: $W_{12} = \text{RMS}(C_{12})$.

In addition to dijet azimuthal angular distributions, the dijet conditional yields, I_{12} , are measured and defined as

$$I_{12} = \frac{1}{N_1} \frac{dN_{1,2}}{dy_1^* dy_2^* dp_{T,1} dp_{T,2}}. \quad (2.14)$$

where $p_{T,1}$, $p_{T,2}$, y_1^* , and y_2^* are the transverse momenta and center-of-mass rapidities of the leading and sub-leading jets, respectively.

The azimuthal angular correlations and conditional yields evaluated in $p+\text{Pb}$ and pp collisions are compared and the ratios in W_{12} and I_{12} between the two systems are calculated as:

$$\rho_W^{p\text{Pb}} = \frac{W_{12}^{p+\text{Pb}}}{W_{12}^{pp}}, \quad \rho_I^{p\text{Pb}} = \frac{I_{12}^{p+\text{Pb}}}{I_{12}^{pp}}. \quad (2.15)$$

Finding a broadening in the dijet angular correlation distribution for $p+\text{Pb}$ collisions compared to pp collisions probes for nuclear effects in the jet formation and scattering off individual gluons of the highly dense gluon field. A suppression of the conditional yields in $p+\text{Pb}$ compared to pp could be an indicator of the mono-jet or jet quenching event signature due to the coherent scattering off the lead nucleus as a whole.

To closer follow next-to-leading-order (NLO) calculations, a minimum $\Delta p_T = p_{T,1} - p_{T,2}$ is required on the dijets [72, 73, 74]. However, techniques such as Sudakov re-summation [75] can take into account the absence of Δp_T requirements. Also, comparisons with fixed-order calculations and soft gluon re-summation, which involve transverse momentum dependent PDFs, instead of collinear PDFs, are better suited for scenarios not requiring any minimum Δp_T cut. The results of the measurement are therefore presented both without any requirement on Δp_T , as well as with the requirement of $\Delta p_T > 3$ GeV.

Chapter 3

ATLAS Required Qualification Work

In order to qualify as an author in the ATLAS collaboration a task must be completed as a contribution to the experiment. The assigned task was to study the impact of service material from the recent Insertable B-Layer (IBL) upgrade on the transverse momentum reconstruction in the forward region. Throughout this task, a large portion of the software required for the thesis analysis was developed because this specific qualification work was chosen with the currently proposed analysis in mind.

The IBL was installed during LS1 between 2013 and 2015. This new pixel detector was needed to achieve better vertex resolution during the higher luminosity Run 2. The service materials, which run out azimuthally from the beam-pipe in high pseudorapidity regions were found to have very high radiation lengths compared to the material previously there. This could have a negative impact on the forward calorimeter's performance.

In order to better understand the effect of the IBL services on forward physics, specifically forward jet measurements, the azimuthal dependence of $\Delta\phi$, and relative p_T response in a forward-central dijet system, as well as azimuthal jet yields were looked at in 5.02 TeV pp data and MC samples. Additionally, jet response and $\Delta\phi$ correlations between truth and reconstructed jets in MC were also studied.

3.1 Event Selection and Cuts

Data from the heavy ion 5.02 TeV pp run in 2015 was used and selected by forward High Level Triggers. The Monte-Carlo samples used were generated by PYTHIA 8 [76], with leading order PDFs, and simulated by GEANT4 [77, 78].

The relative azimuthal angular correlation, $\Delta\phi$, between forward and central, leading and sub-leading jets, was studied at as a function of the central jets' azimuthal angle ϕ . A 20 GeV p_T cut was placed on the central jet, and different cuts were placed on the forward jets. Three jet events were rejected if 40% of the average p_T of the two leading jets was less than the p_T of the third jet. Initially, jets were required to be isolated such that if two jets fall within a cone of $R = 1.0$, then one jet has to have at least twice the

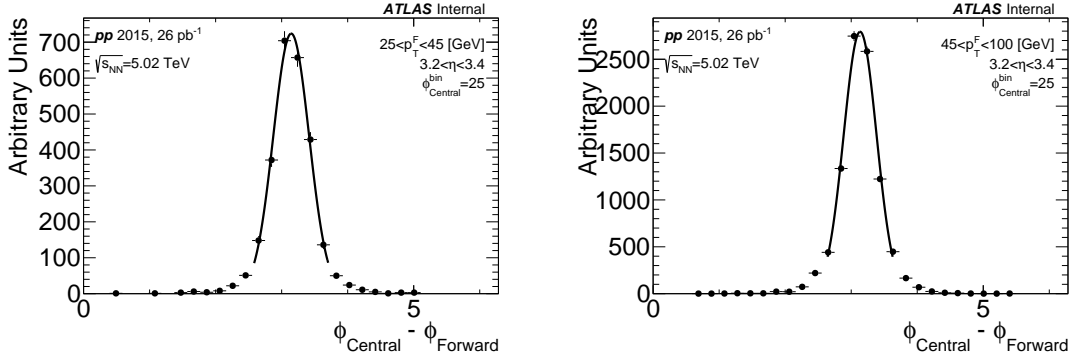


Figure 3.1: Examples of Gaussian fitted $\Delta\phi$ distributions in various η , $p_T^{Forward}$, and $\phi_{Central}$ bins.

transverse momentum of the second jet.

3.2 Procedure

Throughout this study, using the specified data and MC samples, jets were reconstructed using the anti- k_T algorithm with a radius of $R = 0.4$ [50]. Topological towers with a $\Delta\eta \times \Delta\phi = 0.1 \times 0.1$ were constructed from calorimeter information and used as input into the clustering jet reconstruction algorithm. The HI jet calibration was used along with standard event selection cuts. This is the same calibration used in the main thesis analysis and will be discussed in more detail in Chapter 4.

Azimuthal jet yields in bins of pseudorapidity, azimuth, and transverse momentum were normalized to the mean in each bin to get the normalized azimuthal jet yield.

$$\text{Normalized Yield}(p_T, \eta, \phi) = \frac{\text{Yield}(p_T, \eta, \phi) - \text{Mean Yield}(p_T, \eta)}{\text{Mean Yield}(p_T, \eta)} \quad (3.1)$$

Both the $\Delta\phi$ and relative p_T distributions were filled in bins of η , $p_T^{Forward}$, and $\phi_{Central}$. For every $\phi_{Central}$ bin, the respective distribution was fitted to a Gaussian, as shown in Figure 3.1, with some $\Delta\phi$ fits as an example, to yield the final azimuthal distributions.

3.3 Results

For both IBL and non-IBL regions, one forward p_T bin is selected and the normalized yield distributions are plotted for both data and MC in Figure 3.2. The magnitude of the variation in the IBL and non-IBL regions is similar in the data, while in MC it is flat in the non-IBL region, but oscillates in the IBL region. In the data, however, there is even some modulation in the non-IBL region.

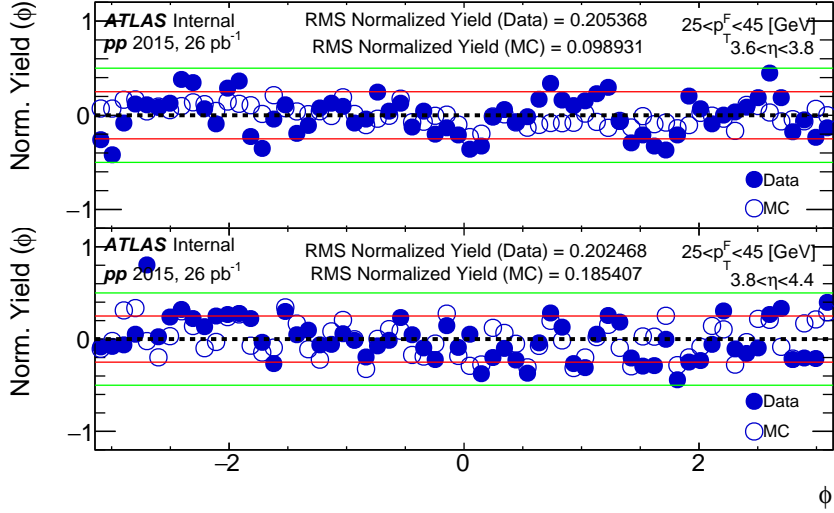


Figure 3.2: Normalized azimuthal jet yields for the forward jet p_T bin $25 < p_T^{Forward} < 45 \text{ GeV}$ is shown in the IBL region ($3.6 < \eta < 3.8$), and non-IBL region ($3.8 < \eta < 4.4$), for both data and MC. Red lines indicate a 25% deviation, and green lines indicate a 50% deviation.

Looking at the RMS of the projections onto the y-axis, in the non-IBL region ($3.6 < \eta < 3.8$) the data has an $RMS = 0.20$ while the MC has an $RMS = 0.098$, and the IBL region ($3.8 < \eta < 4.4$) the data has an $RMS = 0.21$ and the MC an $RMS = 0.16$. This shows that in the data, the two regions are not so different, but they are in the MC. This is due to the IBL services being described differently in the MC than what is actually seen in the data.

There is some difference seen in normalized yields between IBL and non-IBL regions. It is also important to study the $\Delta\phi$ and relative p_T response as functions of the central jet's azimuthal angle in data and MC. The $\Delta\phi$ between forward and central jets is shown in Figure 3.3. The distribution in the data exhibits a saw-tooth pattern which is not well understood, but there does not appear to be a major difference between the IBL and non-IBL regions overall. Relative p_T response in the forward-central dijet system is shown in Figure 3.4. Jets were required to be back-to-back, $2.5 < \Delta\phi < 3.8$. As with the $\Delta\phi$ distributions, no strong difference is seen between IBL and non-IBL regions.

3.4 Conclusion

The IBL service material is found to have no significant impact on the relative p_T response and $\Delta\phi$ azimuthal angular difference in the forward-central dijet system. This is important for the proposed thesis analysis because the forward calorimeter will be one of the most important detectors, and this study shows that the IBL material will not harm the current calibration or affect the important physical quantities.

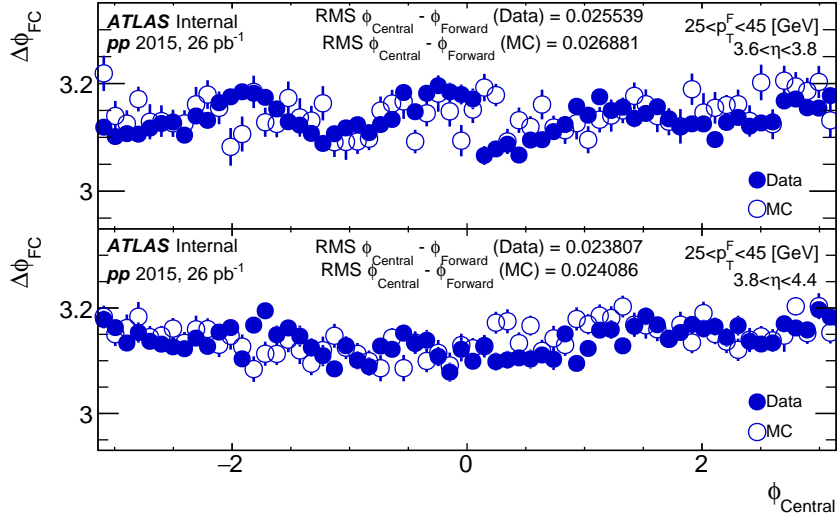


Figure 3.3: As a function of the central jet azimuthal angle, the $\Delta\phi$ distribution for the forward jet p_T bin $25 < p_T^{\text{Forward}} < 45 \text{ GeV}$ is shown in the IBL region ($3.6 < \eta < 3.8$), and non-IBL region ($3.8 < \eta < 4.4$), for both data and MC.

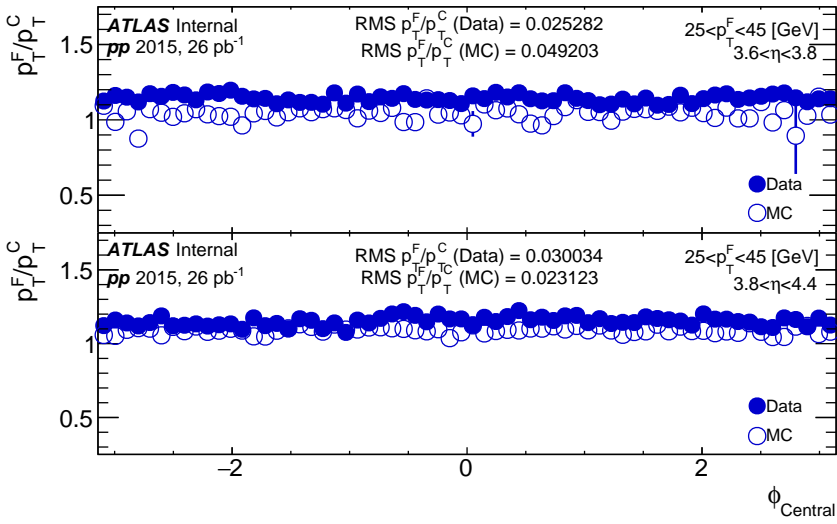


Figure 3.4: As a function of the central jet azimuthal angle, the relative p_T distribution for the forward jet p_T bin $25 < p_T^{\text{Forward}} < 45 \text{ GeV}$ is shown in the IBL region ($3.6 < \eta < 3.8$), and non-IBL region ($3.8 < \eta < 4.4$), for both data and MC.

Chapter 4

Measurement of Dijet Azimuthal Correlations

4.1 Overview

This chapter gives a detailed outline for the analysis of azimuthal correlations in pp and $p+\text{Pb}$ data taken with the ATLAS detector. First, in Section 4.2, an overview of the size and type of data and simulation samples used in the analysis is given. Next, in Section 4.3, the rules for event selection in these respective data and MC samples are discussed. This is including but not limited to simple phase-space cuts or trigger requirements in data. Since jets are the observables used in this analysis, a detailed overview of the jet reconstruction is given in Section 4.4. As with all analysis done in ATLAS, the proper performance of the detector must be verified before the beginning of the physics measurement. Any irregularities that are identified must later be corrected for in order to have a proper physics measurement. Detector performance is evaluated using MC samples and is later used as input into any known systematics that should be taken into account for a precise physics measurement. Next, in Section 4.5, the main analysis procedure is described. This section goes step-by-step through all parts of the analysis, explaining why things were done, and backs up every part with respective plots. Systematic uncertainties, which are very important and a large part of the analysis are presented in Section 4.6. Finally, everything is put together and the results and discussion of the measurements are presented in Section 4.7. A summary of these analysis steps, with their respective sections are below:

- Data sets - Section 4.2
- Trigger and Event Selection - Section 4.3
- Jet Selection and Reconstruction Performance - Section 4.4
- Analysis Procedure - Section 4.5
- Systematic Uncertainties- Section 4.6
- Results - Section 4.7

4.2 Data Sets

The $p+\text{Pb}$ data used in this analysis were recorded in 2016 and the samples used are shown in Table A.1 in the appendix. The LHC was configured with a 4 TeV proton beam and a 1.57 TeV per nucleon Pb beam producing collisions with $\sqrt{s_{\text{NN}}} = 5.02$ TeV and a rapidity shift of the nucleon-nucleon center-of-mass frame $\Delta y = -0.465$ relative to the lab frame. The data collected had one beam configuration with the Pb beam traveling to the positive pseudorapidity direction and the proton beam to the negative pseudorapidity direction. To be consistent with previous $p+\text{Pb}$ physics measurements [56, 79], the positive center-of-mass rapidity direction, $y^* > 0$ is chosen as the proton beam direction. The physical detector is described in terms of η and is consistent with conditions used during data-taking while the center-of-mass rapidity y^* is the physics quantity in which results are presented. The integrated luminosity of the 2016 $p+\text{Pb}$ data taken is $360 \mu b^{-1}$. The pp data used in this measurement was recorded in 2015 with the LHC configured to collide two equal energy proton going beams at a center-of-mass energy of $\sqrt{s} = 5.02$ TeV. These pp and $p+\text{Pb}$ data samples are shown in Table A.1 in the appendix. The instantaneous luminosity conditions provided by the LHC during $p+\text{Pb}$ data taking resulted in an average number of interactions per bunch crossing of 0.03. During pp data taking, the average number of interactions per bunch crossing varied from 0.6 to 1.3.

The performance for measuring azimuthal angular correlations and conditional yields in both the 2015 pp and 2016 $p+\text{Pb}$ data samples is evaluated with a 5.02 TeV pp MC sample simulated using PYTHIA 8.212 [76]. Hard scattering pp events with the A14 [80] tune and the next-to-next order NNPDF23LO PDF set [81] are used. The detector response is then simulated using GEANT4 [77, 78]. The pp samples used for this analysis contain approximately 12 million events, and are listed with their respective number of events in the top Table A.2 in the appendix. Corresponding $p+\text{Pb}$ MC samples are obtained by overlaying minimum-bias $p+\text{Pb}$ data events recorded during the 2016 data-taking period with simulated 5.02 TeV pp events generated with the same MC tune as for the pp MC sample but with a rapidity shift equivalent to that in the $p+\text{Pb}$ collisions. Detector response is also modeled using GEANT4. Due to the forward rapidity filtering, approximately 3 million events were used in the $p+\text{Pb}$ MC samples. These samples are listed in the middle of Table A.2 in the appendix, along with their respective number of events. Additionally, approximately 5 million events of the 5.02 TeV pp HERWIG++ [82] MC simulation are used to compare with the pp PYTHIA8 performance to determine the uncertainties on position resolution. The samples used in the HERWIG++ MC, with their respective number of events are listed in the bottom of Table A.2 in the appendix.

The MC samples used in this analysis are split into so called cross-section weighted slices. This is done in order for different analysis to be able to the p_T regions of phase space that they are interested in for their

JZN	$R = 0.4 p_T^{\text{truth}}$ [GeV]	$\sigma [\text{nb}] \times \epsilon (pp)$	$\sigma [\text{nb}] \times \epsilon (p+\text{Pb})$
1	$20 - 60$	$8.15 \times 10^7 \times 2.83 \times 10^{-3}$	$6.79 \times 10^7 \times 3.85 \times 10^{-4}$
2	$60 - 160$	$6.40 \times 10^5 \times 4.28 \times 10^{-3}$	$8.96 \times 10^5 \times 2.53 \times 10^{-3}$

Table 4.1: Summary of p_T ranges, cross-section weights σ , and filtering efficiencies ϵ in JZN slices for pp and $p+\text{Pb}$ MC samples.

measurement. Some measurements require high p_T jets and some require the lower end of the spectra. The slices are numbered JZN , where N is an integer indicating the p_T interval covered by that sample. Each slice has a cross section weight σ_i and a filtering efficiency ϵ_i which represents the generator level filtering that was implemented to select the appropriate p_T of jets for each JZ sample. This analysis uses the $JZ1$ and $JZ2$ cross section weighted slices. Their respective cross section weights and filtering efficiencies are summarized in Table 4.1. Transverse momentum intervals for each JZ slice are consistent between pp and $p+\text{Pb}$ MC samples, but filtering efficiencies and cross section weights are different. If a wide interval of jet p_T is used in an analysis, covering the ranges of multiple JZ slices, a cross section re-weighting must be implemented when combining slices in order to guarantee a smooth jet p_T spectra. If an observable ω in some bin is a counted quantity, the prescription for combined counts over all cross section weighted slices i with cross section weights σ_i and filtering efficiencies ϵ_i is:

$$\omega = \frac{\sum \omega_i \sigma_i \epsilon_i}{\sum \sigma_i \epsilon_i}. \quad (4.1)$$

If an observable ω is a result of a calculation, the prescription for getting a final cross section weighted value also depends on the number of entries n_i in each bin of the observable and the total number of events N_i^{ev} in each JZ slice:

$$\omega = \frac{\sum \omega_i \sigma_i \epsilon_i \frac{n_i}{N_i^{ev}}}{\sum \sigma_i \epsilon_i \frac{n_i}{N_i^{ev}}}. \quad (4.2)$$

4.3 Trigger and Event Selection

4.3.1 General Cuts

For the analysis of pp and $p+\text{Pb}$ data samples, the first level of filtering is via a Good Runs List (GRL) which is used to clean bad luminosity blocks (lumiblocks). All the data from every run is split up into these lumiblocks, which can hold thousands of events. The GRL is compiled by the collaboration after data quality studies identifying issues with data-taking conditions have been performed after each run. The next step of filtering is at the event level where there is a minimum of one reconstructed vertex required for an event

to pass. Additionally, DAQ errors due to the Scintillator Detector, Tile Calorimeter, and Liquid Argon calorimeters are checked for every event. If any of these detectors are flagged, or a primary vertex is not identified, the event is skipped. Next, events are chosen based on trigger decision.

4.3.2 Trigger Selection

The ATLAS trigger discussed in Section 1.2.1 was used to select minimum-bias and jet events. Jet events were selected by the HLT with L1 seeds from jet, minimum bias, and total-energy triggers. In order to efficiently distribute the limited bandwidth of the trigger to the various physics streams, a procedure known as seeding was used. This relies on having minimum requirement for a given trigger to be considered for processing. This requirement is usually a smaller threshold or minimum-bias trigger firing, which selects less common events more efficiently. The HLT jet trigger, used both in $p+\text{Pb}$ collisions and pp collisions, refined the selection of minimum-bias, level one total energy (L1TEx), or level one jet triggers (LIJx) with various thresholds. The total-energy trigger required a total transverse energy measured in the calorimeter of greater than 5 GeV. The L1 jet trigger required jets with transverse momenta greater than 12 GeV to be reconstructed at the hardware level. The forward jet triggered $p+\text{Pb}$ events were seeded by minimum-bias events by requiring at least one hit in the MBTS detector on each side of the interaction point at the L1 trigger. The HLT jet trigger operated a jet reconstruction algorithm similar to that applied in the offline analysis and selected events containing jets with transverse energy thresholds of 15 GeV in $p+\text{Pb}$ collisions and up to 85 GeV in pp collisions. In both pp and $p+\text{Pb}$ collisions, the highest threshold jet trigger sampled the full delivered luminosity. The trigger selecting minimum-bias events required a track above 200 MeV in the pp data-taking. For $p+\text{Pb}$ data-taking, the minimum-bias trigger required the same conditions at the L1 level in the MBTS that were used to seed forward jet triggered events.

Table 4.2 lists the triggers used during pp data-taking both in the forward ($3.2 < |\eta| < 4.4$), and central ($|\eta| < 3.2$) regions, the corresponding p_T range where the trigger is 99% efficient, and the average prescale used. In pp data-taking, both forward and central triggers are used. Jet trigger efficiencies during pp data-taking for forward and central triggers are shown in Fig.s 4.1 and 4.2. These efficiencies are obtained by comparing jet spectra of various triggers to spectra of MinBias triggers or other lower p_T triggers. A small inefficiency is seen for the lowest forward jet trigger HLT_J25_320ETA490_L1TE5 due to the jet area overlap with the region between forward and central triggers at $|\eta| = 3.2$.

During $p+\text{Pb}$ data-taking, only one forward, unprescaled jet trigger was used because the y^* interval from 2.7 to 4.0 for the leading jet corresponds to a pseudorapidity interval from -3.2 to -4.4. The efficiency plot for this forward jet trigger is shown in Fig. 4.3. This trigger was seeded by the L1 MBTS trigger and

2015 pp Forward ($3.2 < \eta < 4.4$) Trigger	p_T	Efficiency Range [GeV]	Average Prescale
HLT_j25_320eta490_L1TE5		28 —— 42	290.476
HLT_j35_320eta490_L1TE10		42 —— 52	74.11
HLT_j45_320eta490		52 —— 65	1.413
HLT_j55_320eta490		65 —— 90	1.413
2015 pp Central ($ \eta < 3.2$) Trigger	p_T	Efficiency Range [GeV]	
HLT_j20		28 —— 35	5827.311
HLT_j30_L1TE5		35 —— 44.5	297.388
HLT_j40_L1TE10		44.5 —— 59	73.183
HLT_j50_L1J12		59 —— 70	14.225
HLT_j60_L1J15		70 —— 79	10.807
HLT_j75_L1J20		79 —— 89	1.012
HLT_j85		89 —— 90	1.002

Table 4.2: List of pp triggers with associated p_T ranges where the trigger is over 99% efficient.

2016 $p+Pb$ Forward ($-4.4 < \eta < -3.2$) Trigger	p_T	Efficiency Range [GeV]	Average Prescale
HLT_j15_ion_n320eta490_L1MBTS_1_1		28 —— 90	1.02

Table 4.3: Un-prescaled $p+Pb$ trigger with associated p_T ranges where the trigger is over 99% efficient.

2016 $p+Pb$ Min-Bias Trigger
HLT_mb_sptrk_L1MBTS_1_OVERLAY
HLT_noalg_L1TE5_OVERLAY
HLT_noalg_L1TE20_OVERLAY

Table 4.4: List of 2016 $p+Pb$ triggers used to tag events for the MC data overlay.

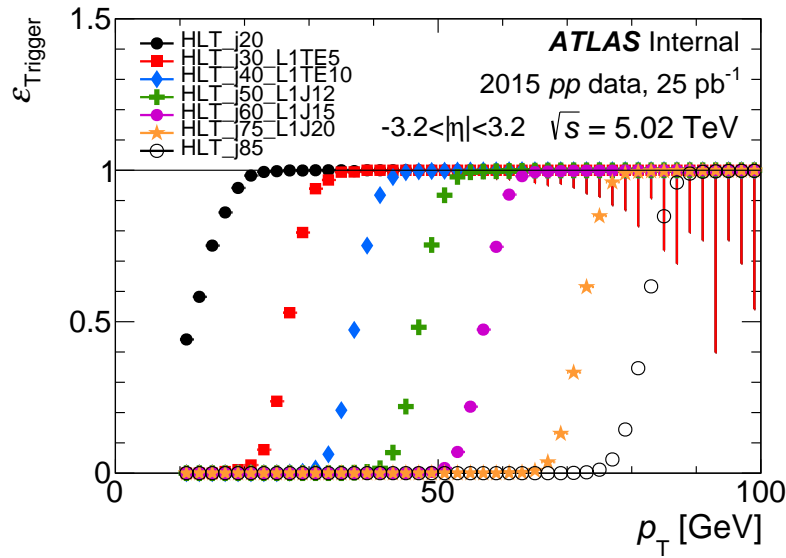


Figure 4.1: Jet trigger efficiency for pp central triggers in the pseudorapidity range $-3.2 < |\eta| < 3.2$.

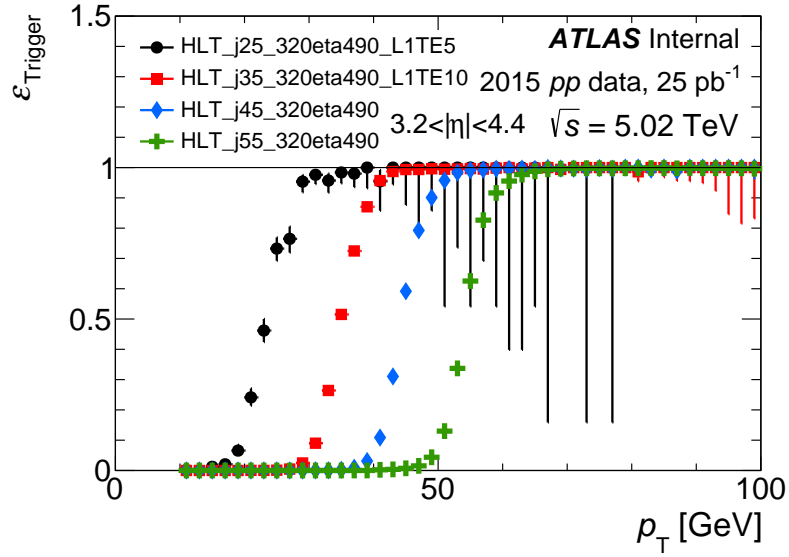


Figure 4.2: Jet trigger efficiency for pp forward triggers in the pseudorapidity range $3.2 < |\eta| < 4.4$. A small inefficiency is seen for the lowest forward jet trigger HLT_J25_320ETA490_L1TE5 due to the jet area overlap with the region between forward and central triggers at $|\eta| = 3.2$.

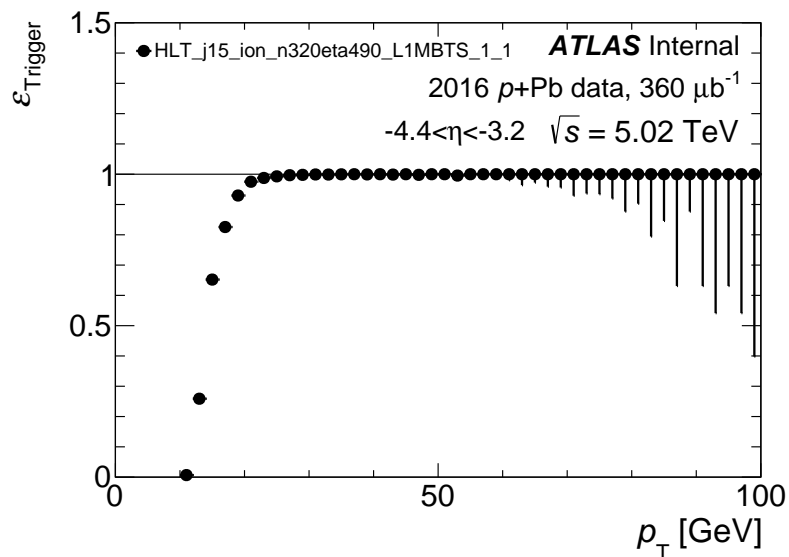


Figure 4.3: Jet trigger efficiency for $p+\text{Pb}$ forward triggers in the pseudorapidity range $3.2 < |\eta| < 4.4$.

its corresponding p_T range used is shown in Table 4.3. The $p+Pb$ triggers used to produce the data overlay for the $p+Pb$ MC are shown in Table 4.4. For the data overlay, entire events were selected based solely on the MB trigger decision with no requirement on jets.

To check that the performance of jet triggers was consistent across runs in pp and $p+Pb$ data-taking, the number of jets in some $p_{T,1}$ and y_1^* intervals were counted and divided by the prescale-corrected luminosity of each run. Plotted as a function of run number, this ratio should be relatively uniform and is shown for central and forward pp triggers and forward $p+Pb$ trigger in Fig. 4.4. The large luminosity uncertainty during the $p+Pb$ data taking contributed to the statistical fluctuations seen this ratio for the forward jet trigger.

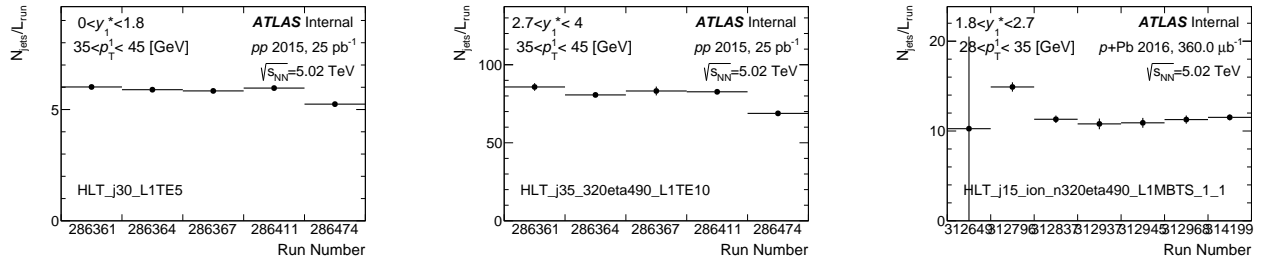


Figure 4.4: Number of jets in some $p_{T,1}$ and y_1^* interval divided by prescale-corrected luminosity for each run. Central pp trigger (left), forward pp trigger (center), and forward $p+Pb$ trigger (right).

4.3.3 Disabled HEC in $p+Pb$ Data-taking

During the 2016 $p+Pb$ data-taking period, part of the HEC in the lead going direction was disabled in the pseudorapidity and azimuthal intervals $-3.2 < \eta < -1.3$ and $-\pi < \phi < -\pi/2$, respectively. Reconstructed dijets where the sub-leading jet area overlaps with the disabled HEC region are excluded from the analysis in $p+Pb$ data and MC samples. Plots of jet multiplicity in $\eta \times \phi$ space for the $p+Pb$ data, MC signal, and MC with data overlay samples for the lowest jet p_T interval $25 < p_T < 35$ GeV are shown in Fig. 4.5. In the signal MC simulation, which does not include any data overlay, there appears to be a small cavity in the region covered by the HEC. This is also seen in the $p+Pb$ data. However, in the MC simulation with data overlay, this region is not disabled. To account for the jet radius $R = 0.4$ the excluded region is increased to not include jets with jet axes in $-3.6 < \eta < -0.9$ in pseudorapidity, and $-\pi < \phi < (-\pi/2 + 0.4)$ and $(\pi - 0.4) < \phi < \pi$ in azimuth. This detector inefficiency is corrected by a procedure that will be described in a later section.

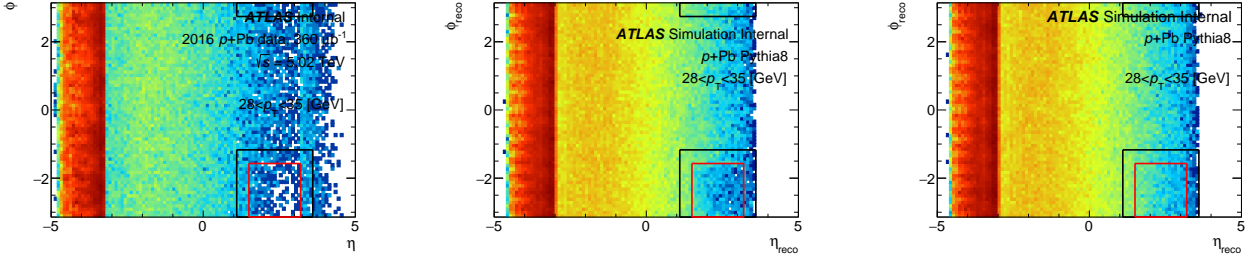


Figure 4.5: Maps of ϕ vs η shown for lowest p_T interval $25 < p_T < 35$ GeV for the $p+\text{Pb}$ data (left), $p+\text{Pb}$ MC with only signal included (center), and $p+\text{Pb}$ MC with data overlay (right). A depletion is seen in the data for the region covered by the HEC detector in the lead going direction (negative η), and a minor cavity is seen in the signal MC in the same region. No apparent effect is seen in the MC with data overlay. The red box indicates the HEC region which was turned off. Due to the jet radius $R = 0.4$ the excluded region is increased, and is indicated by the black box.

4.4 Jet Selection and Reconstruction Performance

Jets are reconstructed using a heavy ion reconstruction procedure developed for previous jet measurements in Pb+Pb and $p+\text{Pb}$ collisions [56, 79]. The jet reconstruction is first run in four-momentum recombination mode, on $\Delta\eta \times \Delta\phi = 0.1 \times 0.1$ calorimeter towers with the anti- k_t algorithm [50] with $R = 0.4$. Energies in the towers are obtained by summing the energies of calorimeter cells at the electromagnetic energy scale within the tower boundaries. Then, an iterative procedure is used to estimate the layer and η -dependent underlying event (UE) transverse energy density, while excluding the regions populated by jets. The UE transverse energy is subtracted from each calorimeter tower and the four-momentum of the jet is updated accordingly. Jets which do not overlap with the region included in the UE background subtraction also have a small correction applied on the order of a few percent. Then, a jet η - and p_T -dependent correction factor derived from the simulation samples is applied to correct for the calorimeter response. These factors are derived by the ATLAS Jet E_T Miss (JetEtMiss) group and are standard corrections used in all analyses. An additional data driven correction based on *in situ* studies of the momentum balance of jets recoiling against photons, Z bosons, and jets in other regions of the calorimeter is also applied [83, 84].

Jets are selected in the transverse momentum range of $28 < p_T < 90$ GeV and a center-of-mass rapidity of $-4.0 < y^* < 4.0$. This is the largest symmetric overlap between the two colliding systems for which most forward jets can be reconstructed using the FCal with full coverage for $R = 0.4$ jets. All reconstructed jets are required to have a p_T such that the jet trigger efficiency is greater than 99%. As a result, no trigger efficiency correction is applied.

The MC samples are used to evaluate the jet reconstruction performance and to correct the measured distributions for detector effects. This is done independently for both pp and $p+\text{Pb}$ collisions. In the

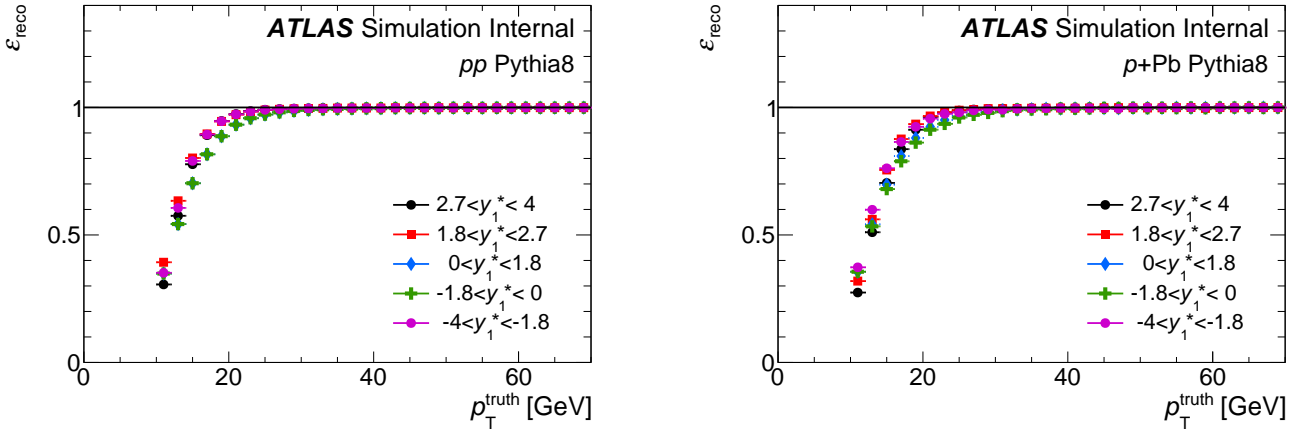


Figure 4.6: Jet reconstruction efficiency evaluated in the pp (left) and $p+\text{Pb}$ (right) PYTHIA8 MC samples.

MC samples, the generator level jets are reconstructed from primary particles¹ with the anti- k_t algorithm with radius $R = 0.4$. Using the pseudorapidity and azimuthal angles η_{truth} , ϕ_{truth} , η_{reco} , and ϕ_{reco} of the generated and reconstructed jets, respectively, generator level jets are matched to reconstructed jets by requiring $\Delta R < 0.2$, where $\Delta\eta = |\eta_{\text{reco}} - \eta_{\text{truth}}|$, and $\Delta\phi = |\phi_{\text{reco}} - \phi_{\text{truth}}|$.

The efficiency of reconstructing jets in pp and $p+\text{Pb}$ collisions is evaluated using the PYTHIA8 MC samples by determining the probability of finding a reconstructed jet associated with a generator level jet. The jet reconstruction efficiencies are shown in Fig. 4.6 for pp and $p+\text{Pb}$ MC samples in different y^* and p_T regions. The jet reconstruction efficiency is greater than 99% for jets with $p_T > 30$ GeV over the selected y^* range $-4.0 < y^* < 4.0$ and drops to 95% at a jet $p_T = 28$ GeV. The variation of the jet reconstruction efficiency with y^* is due to jets having a higher total energy for a given transverse energy as compared to more central regions.

The ratios of transverse momenta of generated and reconstructed jets, p_T^{truth} and p_T^{reco} respectively, determine the relevant jet energy scale (JES) $p_T^{\text{reco}}/p_T^{\text{truth}}$, and jet energy resolution (JER) $\sigma(p_T^{\text{reco}}/p_T^{\text{truth}})$, which characterize the jet energy reconstruction performance. The JES and JER are plotted as a function of p_T^{truth} , in intervals of generated jet pseudorapidity η^{truth} in Fig. 4.7, 4.8 for pp and $p+\text{Pb}$ MC samples, respectively. The means and standard deviations of the $p_T^{\text{reco}}/p_T^{\text{truth}}$ distributions, along with their errors are extracted from fits of the distributions to Gaussian function. The JES shows a very small dependence on η^{truth} , with a maximum deviation of $\pm 3\%$ from unity at $p_T^{\text{truth}} = 30$ GeV and a minimum of -3% deviation from unity at $p_T^{\text{truth}} = 50$ GeV. The JES decreases with p_T^{truth} , and with decreasing η .

¹Primary particles are defined as particles with a mean lifetime $\tau > 0.3 \times 10^{-10}$ s, excluding muons and neutrinos, which are weakly interacting and do not leave significant energy deposits in the calorimeters.

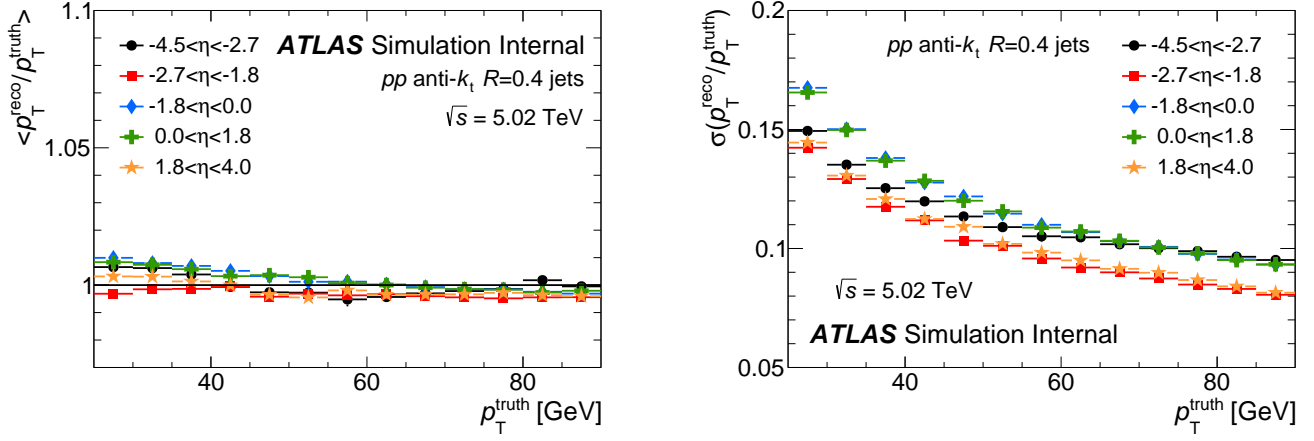


Figure 4.7: JES (left) and JER (right) evaluated in pp MC samples and plotted as a function of p_T^{truth} .

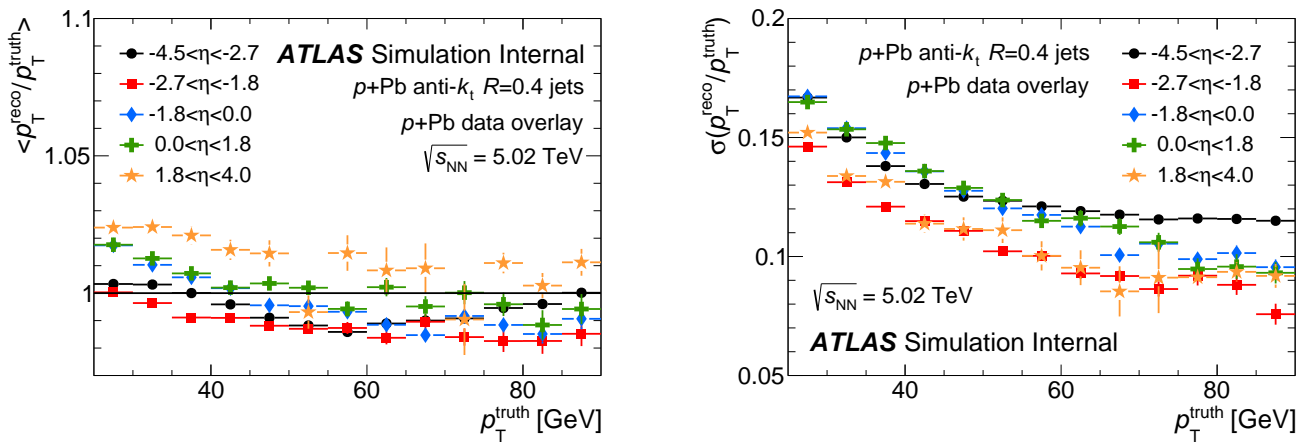


Figure 4.8: JES (left) and JER (right) evaluated in $p+Pb$ MC samples and plotted as a function of p_T^{truth} .

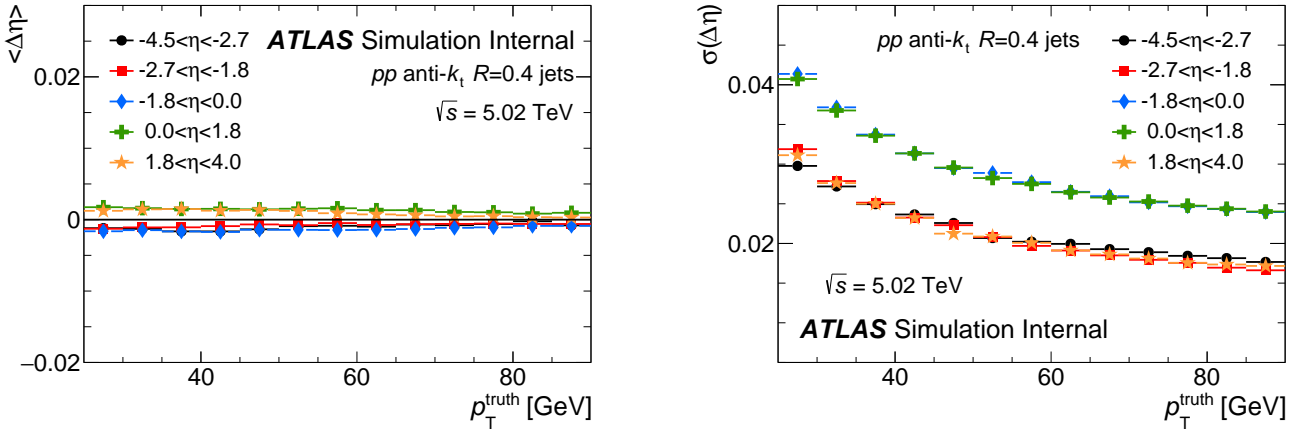


Figure 4.9: The mean angular distance $\langle \Delta\eta \rangle$ (left) and resolution $\sigma(\Delta\eta)$ (right) between truth and reconstructed jets evaluated in pp MC samples and plotted as a function of p_T^{truth} .

The mean angular distance $\langle \Delta\eta \rangle$ and jet angular resolution (JAR) for pseudorapidity $\sigma(\Delta\eta)$ between truth and reconstructed jets $\Delta\eta = \eta_{\text{reco}} - \eta_{\text{truth}}$ is plotted in Fig.s 4.9, 4.10 for the pp and $p+\text{Pb}$ MC samples respectively. Similarly, mean angular distance $\langle \Delta\phi \rangle$ and azimuthal JAR $\sigma(\Delta\phi)$ between truth and reconstructed jets $\Delta\phi = \phi_{\text{reco}} - \phi_{\text{truth}}$ is plotted in Fig. 4.11 and 4.12 in pp and $p+\text{Pb}$ MC samples respectively. Similar to the procedure used for extracting the JER and JES, means and standard deviations are extracted from fits with a Gaussian function. For both pseudorapidity and azimuth, $\langle \Delta\eta \rangle$ and $\langle \Delta\phi \rangle$ are consistent with zero in the pp MC sample. In the $p+\text{Pb}$ MC sample, $\langle \Delta\phi \rangle$ is consistent with zero but there is a shift of less than 0.01 in $\langle \Delta\eta \rangle$ from the underlying event contribution. This is a result of the UE pulling the reconstructed jet in the lead going direction, however it is a negligible effect which is less than 1/10 of the tower size. The angular resolution $\sigma(\Delta\eta)$ and $\sigma(\Delta\phi)$ decreases as a function p_T^{truth} as expected.

Performance Study of $p+\text{Pb}$ MC

The wrongly configured HEC condition in the $p+\text{Pb}$ MC sample with data overlay raised questions about other possible discrepancies in detector conditions. One way check the reliability of the MC reconstruction conditions is to use tracks reconstructed in the inner detector tracker, which is very precise, and compare the results against jets. This is done by studying the comparison of r_{trk} distributions as a function of jet p_T in data and MC. r_{trk} is defined as:

$$r_{\text{trk}} = \frac{\sum p_{\text{T}}^{\text{trk}_i}}{p_{\text{T}}^{\text{jet}}} \quad (4.3)$$

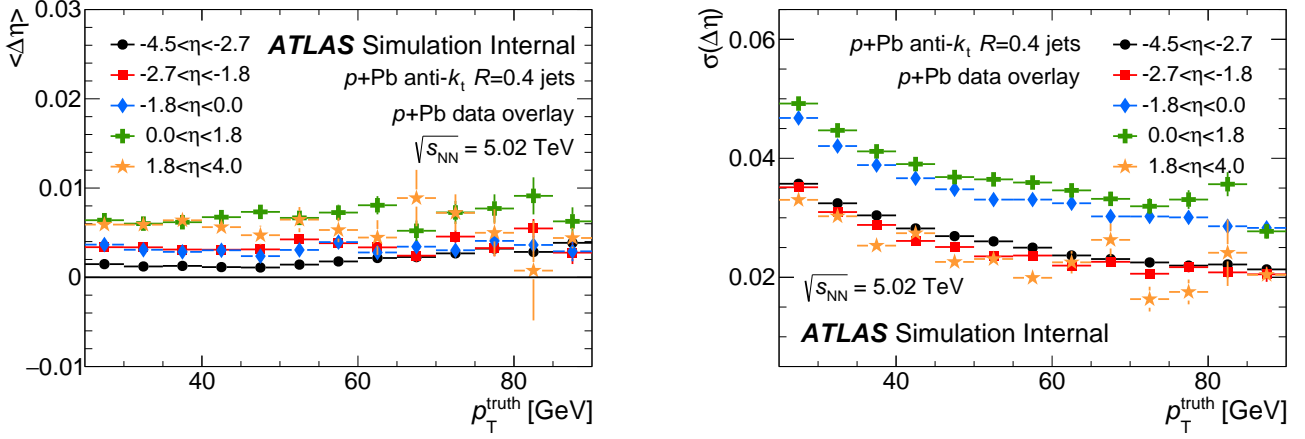


Figure 4.10: The mean angular distance $\Delta\eta$ (left) and resolution $\sigma(\Delta\eta)$ (right) between truth and reconstructed jets evaluated in $p+\text{Pb}$ MC samples and plotted as a function of p_T^{truth} .

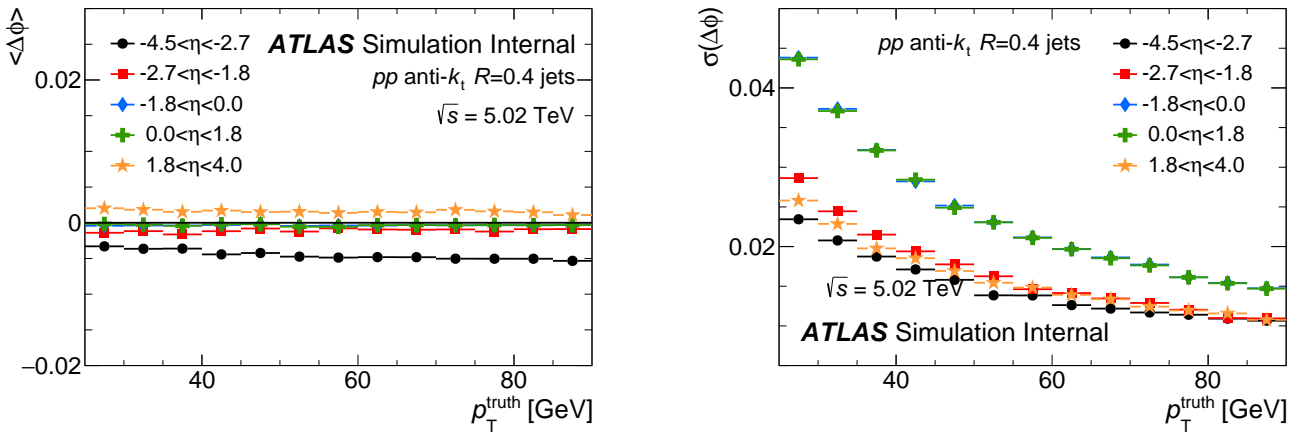


Figure 4.11: The mean angular distance $\Delta\phi$ (left) and resolution $\sigma(\Delta\phi)$ (right) between truth and reconstructed jets evaluated in pp MC samples and plotted as a function of p_T^{truth} .

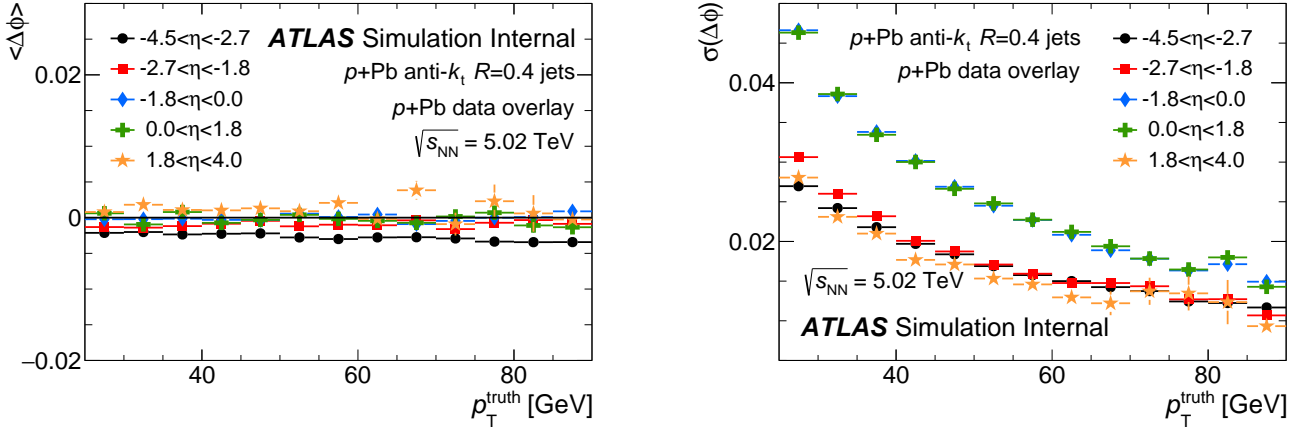


Figure 4.12: The mean angular distance $\Delta\phi$ (left) and resolution $\sigma(\Delta\phi)$ (right) between truth and reconstructed jets evaluated in $p+\text{Pb}$ MC samples and plotted as a function of p_T^{truth} .

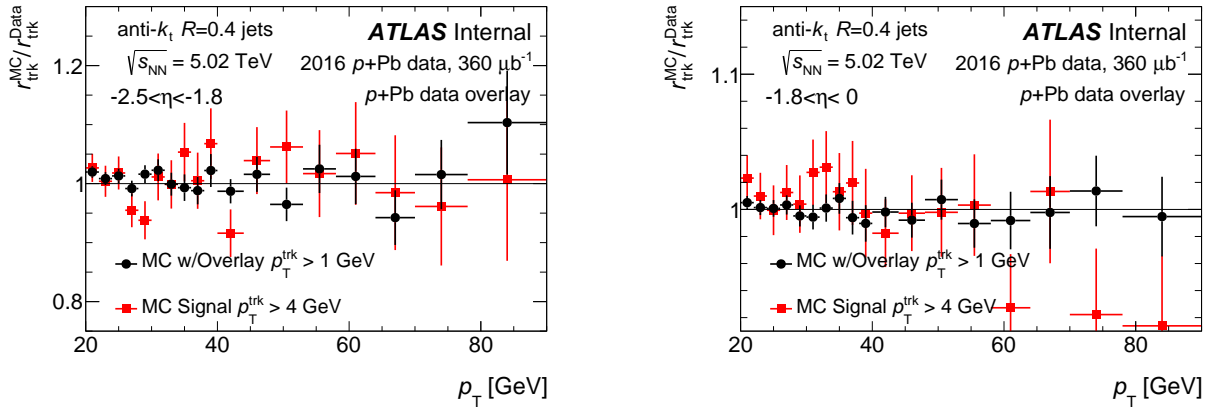


Figure 4.13:

where $\sum p_T^{\text{trki}}$ is the sum of transverse momenta of all tracks that fall within a reconstructed jets area. If the ratio of r_{trk} between data and MC samples is consistent with unity, the test acts as a data-driven check that the MC conditions are consistent with those during the data-taking. This ratio is shown in Figure 4.13 for two proton going direction ranges of pseudorapidity in a region of the detector where the tracker can be used. The figures show the ratio of r_{trk} between data and MC samples for the $p+\text{Pb}$ MC sample with data overlay, as well as the $p+\text{Pb}$ signal sample alone. The results in the central part of the barrel $-1.8 < \eta < 0$ show good closure. The results in the extended barrel $-2.5 < \eta < -1.8$ have high statistical fluctuations, but are consistent with unity at lower p_T . The jet radius of $R = 0.4$ near the edge of the tracker $\eta = -2.5$ also introduces uncertainties as not all of the tracks in the jet pass through the tracker. This test still shows that the conditions in the $p+\text{Pb}$ data and MC samples are consistent.

$p_{\text{T},1}$ Bins [GeV]	$p_{\text{T},2}$ Bins [GeV]	y_2^* Bins
$28 < p_{\text{T},1} < 35$	$28 < p_{\text{T},2} < 35$	$2.7 < y_{\text{jet}}^* < 4.0$
$35 < p_{\text{T},1} < 45$	$35 < p_{\text{T},2} < 45$	$1.8 < y_{\text{jet}}^* < 2.7$
$45 < p_{\text{T},1} < 90$	$45 < p_{\text{T},2} < 90$	$0.0 < y_{\text{jet}}^* < 1.8$ $-1.8 < y_{\text{jet}}^* < 0.0$ $-4.0 < y_{\text{jet}}^* < -1.8$

Table 4.5: Transverse momentum and y^* binning for leading and sub-leading jets. For the leading jet, only the $2.7 < y_1^* < 4.0$ bin is used.

4.5 Analysis Procedure

4.5.1 Overview

In both the pp and $p+\text{Pb}$ MC and data samples, two highest p_{T} jets are used to study azimuthal angular correlations. The measurement uses jets with transverse momentum between 28 GeV to 90 GeV. Due to the jet radius $R = 0.4$, the full coverage of the forward detector up to $|\eta| = 4.9$ is reduced to cover only up to 4.5 in pseudorapidity. Furthermore, due to the center-of-mass rapidity shift of $\Delta y=0.465$ in the $p+\text{Pb}$ collision system, the corresponding y^* interval that is studied is approximately $-4.0 < y^* < 4.0$. The y^* interval used in the measurement is consistent in the pp and $p+\text{Pb}$ collision systems. The final observables in this analysis are widths of dijet C_{12} distributions and conditional yields. The widths are sensitive to broadening between the leading and sub-leading jets and the yields show the number of dijets, given a leading jet in each p_{T} and y^* kinematic region.

The binning of this measurement is summarized in Table 4.5 and is composed of different combinations of y_1^* , y_2^* , $p_{\text{T},1}$, and $p_{\text{T},2}$, where y_1^* and $p_{\text{T},1}$ is the position and transverse energy of the leading jet, and y_2^* and $p_{\text{T},2}$ is the position and transverse energy of the sub-leading jet. Since the measurement aims to probe low-x partons, only the interval $2.7 < y_1^* < 4.0$, which is the proton going direction in $p+\text{Pb}$ is used. The y^* binning is chosen to be consistent with the center of mass rapidity boundary between forward and central triggers in $p+\text{Pb}$ data taking. The transverse momentum binning was chosen to be on the boundaries of the p_{T} intervals used for different triggers in pp data taking.

The C_{12} distributions are evaluated as a function of $\Delta\phi$ in combinations of y_1^* , y_2^* , $p_{\text{T},1}$, and $p_{\text{T},2}$ bins, unfolded, and normalized by the leading jet p_{T} spectra. Leading jet $p_{\text{T},1}$ spectra are estimated in different y_1^* bins and are also unfolded. The azimuthal correlation distributions are fitted to extract their widths W_{12} and integrated of over their full range to extract the conditional yields I_{12} . The correct normalization by number of leading jets is important for the measurement of I_{12} and thus must be analyzed carefully.

To account for detector affects, the distributions in data have to be unfolded using MC information. The method used is the bin-by-bin unfolding which relies on MC information about the relationship between any

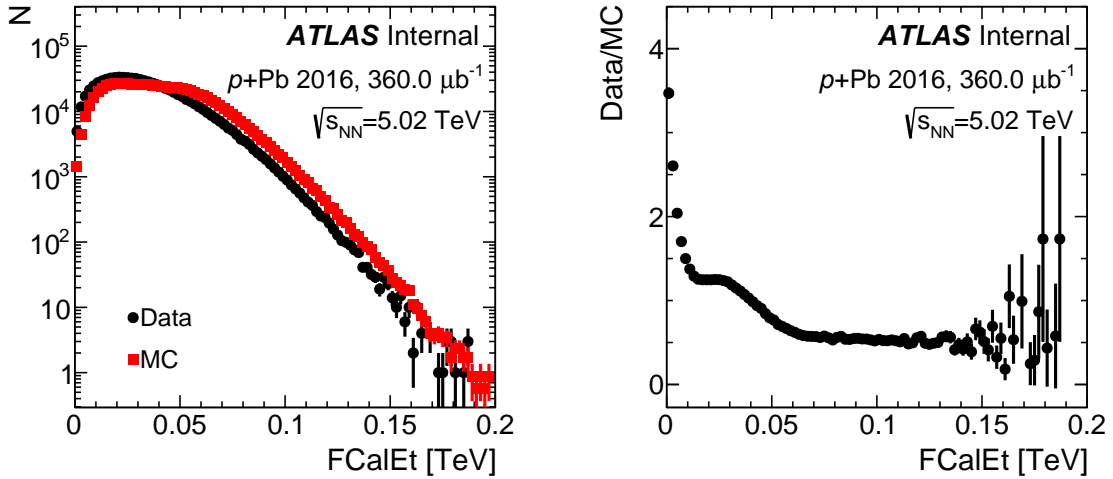


Figure 4.14: Total FCal E_T distributions in $p+Pb$ MC and data (left), and ratio MC/Data (right).

truth and reconstructed quantity. This type of unfolding is sensitive to differences in the shapes of data and MC distributions and requires a re-weighting of the MC before unfolding factors can be evaluated. The re-weighting is done in two steps: 1) weights for jet p_T spectra are evaluated; 2) when deriving weights for C_{12} distributions, the dependence on the jet p_T spectra is removed by applying the weights from the previous step. The final weight is the product of the two weights.

To better match UE levels to the data, the $p+Pb$ MC is re-weighted at the event level. The total FCal E_T distribution in MC is divided by the total FCal E_T in data to derive the event weights which are then applied to the MC. The total FCal E_T distributions in $p+Pb$ MC and data, along with the ratio between the two distributions are shown in Fig. 4.14.

4.5.2 Unfolding Procedure

Detector effects affecting the leading jet p_T spectra and $dN_{1,2}/d\Delta\phi$ distributions in pp and $p+Pb$ collisions are corrected using a bin-by-bin unfolding procedure. For more information on the this procedure see Appendix B. The unfolding procedure corrects for the effect of the migration due to the finite JER, JAR, and the jet reconstruction efficiency. The jets excluded due to the disabled HEC region in $p+Pb$ data and MC samples are naturally accounted-for using the same procedure. Two corresponding MC distributions for each of the two observables are evaluated, one using generator level jets and the other using reconstructed jets after the detector simulation. The MC response matrices are also filled using the same procedure. The diagonal elements of these matrices represent pairs of truth and reconstructed jets agree in momentum

and position intervals of the measurement. The response matrix is always a multidimensional object with twice the number of dimensions used in the phase space of the measurement. The ratio of these two MC distributions provides correction factors which are then applied to the data. The correction factors C_i are defined as:

$$C_i = \frac{T_i}{R_i}, \quad (4.4)$$

where T_i and R_i are the number of truth and reconstructed dijets, respectively. However, The reconstructed and generated distributions are manifestations of each other since they former is actually a detector reconstruction of its respective truth event. Thus, T_i and R_i are partially correlated, the resulting errors on the correction factors are defined as:

$$\delta C_i^2 = \frac{T_i^2}{R_i^3} \left(1 - \frac{M_{ii}^2}{T_i R_i} \right), \quad (4.5)$$

where M_{ii} are the diagonal elements of the response matrix. These errors take into account the correlation between the truth and reconstructed quantities. Errors on correlated quantities will be smaller than those on purely uncorrelated distributions because if there is no migration, i.e. the reconstructed quantities perfectly resemble their generator level counterparts, $M_{ii} = T_i = R_i$ and therefore $\delta C_i^2 = 0$. However, there is insignificant migration in energy and position, so the diagonal matrix elements are rarely similar to either the reconstructed or generated counts.

As mentioned previously, bin-by-bin unfolding procedure is sensitive to the shapes of the distributions from which the correction factors are derived. This method works when the shape of the data distribution matches the shape of the MC distributions. Since both the p_T spectra and C_{12} distributions are unfolded with correction factors, both distributions must first be re-weighted. The weights are estimated as ratios of distributions of Data/MC_{Reco}. The value of the weight for a given truth and reconstructed jet pair is obtained from the truth jet kinematics. This procedure is done for all jet measurements and is motivated by the need to re-weight the prior (truth) distribution. Further, re-weighting using reconstructed kinematics could introduce inefficiency to the response matrix. In the following procedure, jet p_T spectra weights are derived first. Then C_{12} weights are derived with the p_T spectra weight applied. With this intermediate re-weighting in jet p_T spectra, it is found that the C_{12} weights are invariant in p_T , allowing extrapolation into underflow and overflow bins in p_T , and reducing statistical fluctuations. Final C_{12} weights are derived only as a function of $\Delta\phi$ in bins of y^* , removing the p_T dependence. The product of p_T spectra weights and the C_{12} weights is applied to the final MC distributions when deriving the correction factors.

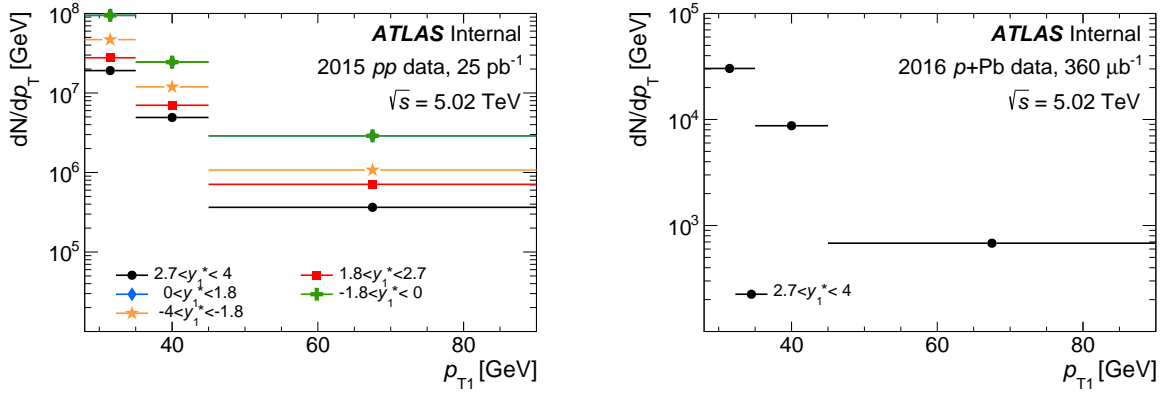


Figure 4.15: Single-jet p_T spectra for jets in pp data (left) and $p+Pb$ data (right) in bins of y^* .

From the re-weighted MC truth and reconstructed distributions, correction factors are derived and applied to data both for the p_T spectra and $dN_{1,2}/d\Delta\phi$ distributions. The unfolded $dN_{1,2}/d\Delta\phi$ data distributions are scaled by the unfolded leading jet p_T spectra information to obtain C_{12} and are then fitted to the exponentially modified Gaussian function. The widths are extracted from fit results, and the conditional yields are extracted by integrating these C_{12} distributions.

4.5.3 Jet Spectra

Jets in pp and $p+Pb$ data are required to have a trigger fired, and any jet(s) are required to be in the trigger's pseudorapidity range and transverse momentum interval where the trigger efficiency is above 99%. The jets are entered with prescale weights given by the ATLAS Lumi-Calc for each trigger and run. For the $2.7 < y_1^* < 4.0$ rapidity range, the contribution of different triggers to the final spectra is shown for pp data in Fig. 4.16. The leading jet p_T spectra for pp data are presented in different forward y^* bins on the left of Fig. 4.15 and for $p+Pb$ data on the right of Fig. 4.15. In $p+Pb$ data, only one trigger with no pre-scale is used, thus, unlike the pp spectra, where there are many trigger contributions, the final spectra is composed entirely of one trigger. The p_T binning is consistent with what is shown in Table 4.5 because these spectra will eventually be used for normalization of $\Delta\phi$ distributions.

In MC, jet p_T spectra are filled separately for each cross section weighted (JZx) sample, and then combined using the cross section weights and filtering efficiencies. If no cross section weighted recombination is performed, the spectra will not be smooth and will have jumps at the jet p_T corresponding to the boundaries covered by the individual JZ samples. The smoothly falling spectra from MC show that the cross section weighted recombination is working correctly. Reconstructed and truth leading jet p_T spectra for the pp MC are shown in Fig. 4.17 and for the $p+Pb$ MC in Fig. 4.18.

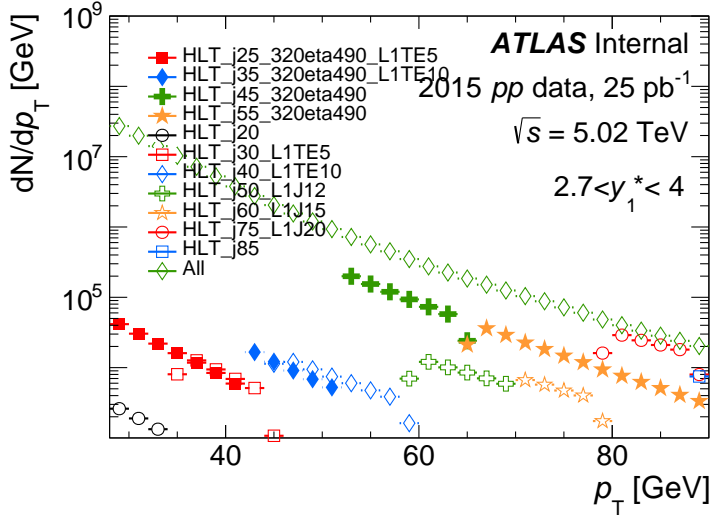


Figure 4.16: Individual triggers, and resulting jet p_T spectra for pp data for the $2.7 < y_1^* < 4.0$ rapidity range.

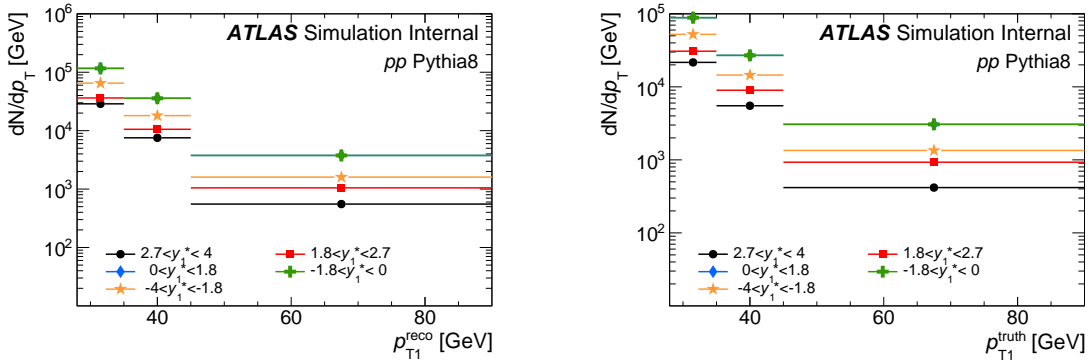


Figure 4.17: Reconstructed (left) and truth (right) level leading jet p_T spectra in pp MC in bins of y^* .

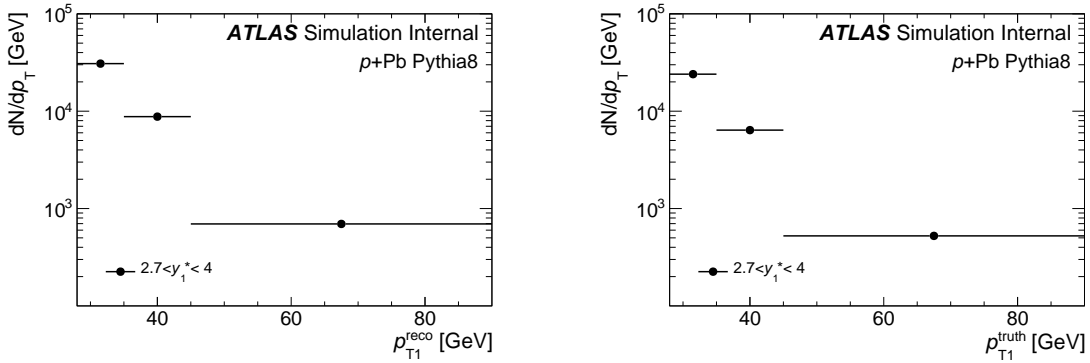


Figure 4.18: Reconstructed (left) and truth (right) level leading jet p_T spectra in $p + Pb$ MC in bins of y^* .

4.5.4 Jet Spectra Re-weighting

The leading jet p_T spectra weights in both the pp and $p+\text{Pb}$ MCs are derived as the ratio of Data/MC_{Reco} leading jet p_T spectra. The weights are derived by first scaling the Data and MC spectra to a common integral and then taking their quotient in bins of y^* . Jet p_T spectra with fine binning are used to have better sensitivity to the shape. Scaled jet p_T spectra from data and reconstructed level MC are shown as the black and red points, respectively, on the top plots of Fig. 4.19. Their ratio, which represents the jet p_T spectra re-weighting factors, is show by the blue points in the bottom plots of Fig. 4.19. Jet p_T spectra weights are consistent with unity in pp and $p+\text{Pb}$ collisions.

The shape of the re-weighted reconstructed level MC jet spectra should match the shape of the reconstructed level jet spectra from data. To check this, reconstructed jet spectra from data are compared to reconstructed jet spectra before and after re-weighting in MC. The ratio of data to re-weighted MC is consistent with unity for pp and $p+\text{Pb}$. The ratio and reconstructed jet p_T spectra as shown as the red points in Fig. 4.19.

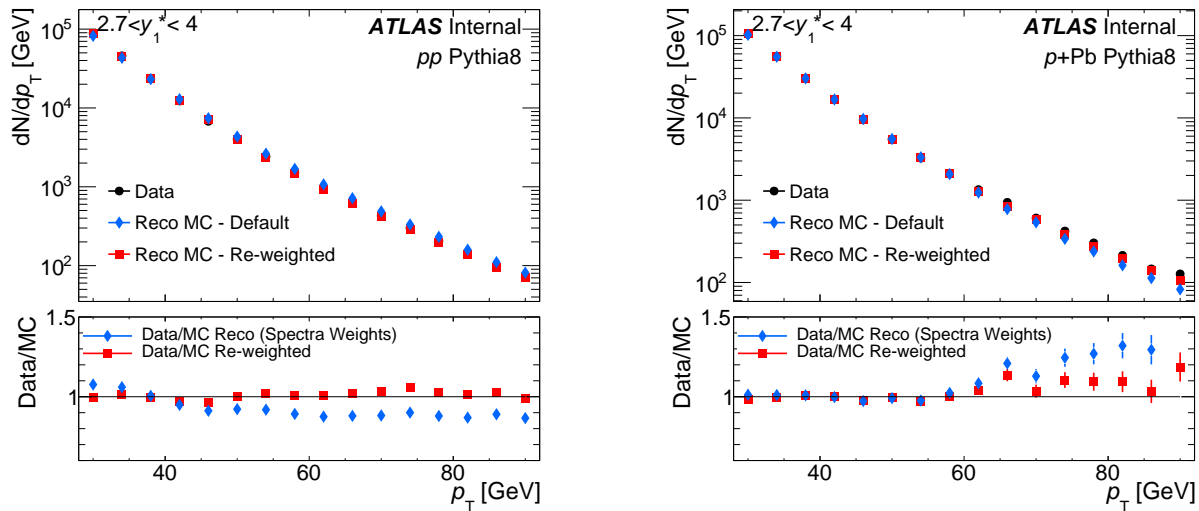


Figure 4.19: Reconstructed level data (black) and re-weighted (red) and default (blue) reconstructed jet spectra from MC, with ratios. Jet p_T spectra re-weighting factors are represented by the ratio of Data to reco MC (blue poitns in ratio). The ratio to data to re-weighted MC (red points in ratio) is consistent with unity for pp (left) and $p+\text{Pb}$ (right). Shown for $2.7 < y_1^* < 4.0$, which is the only y_1^* bin used in the analysis.

Jet spectra are not re-weighted in y^* because the effect from the JAR is much smaller than from JER and additionally, wide bins in rapidity are used. Putiry matrices for pp and $p+\text{Pb}$ MC showing migration in y^* are shown in Fig. 4.20. There is minor migration, with a purity of at least 97% indicating no significant change in the shape of the distribution as a function of y^* .

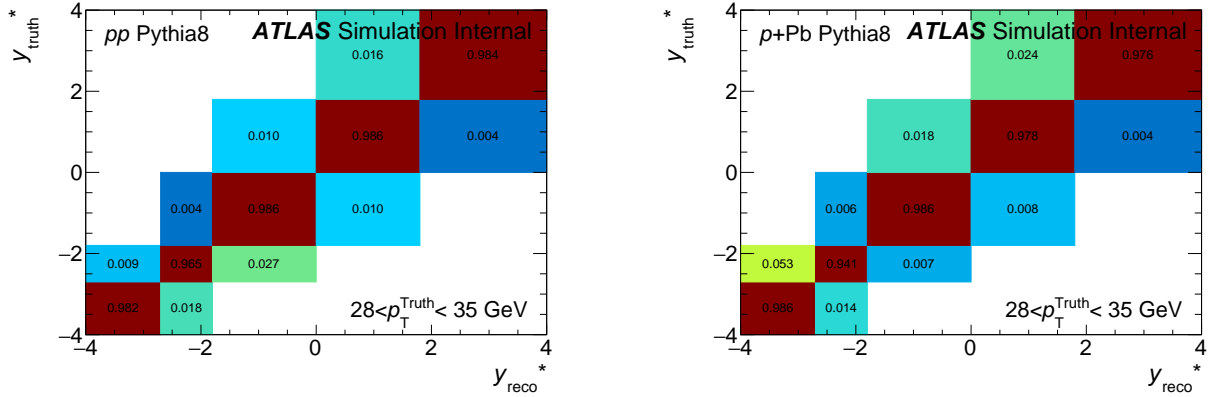


Figure 4.20: Purity matrices for y^* , shown for pp (left) and $p+Pb$ MCs. High purity indicates very minor effect on the shape of the distribution. Shown for the $28 < p_T^{\text{Truth}} < 35 \text{ GeV}$ interval.

4.5.5 Jet Spectra Unfolding

To unfold the leading jet p_T spectra, the unfolding procedure described in 4.5.2 is used with correction factors obtained from the ratio the truth to reconstructed leading jet p_T spectra. The response matrix describes the bin migration between p_T^{truth} and p_T^{reco} . The pp reconstructed and truth jet p_T spectra, with the response matrix and resulting correction factors are shown on the left of Fig. 4.21. Similarly, the $p+Pb$ reconstructed and truth jet p_T spectra, with the response matrix and resulting correction factors are shown on the right of Fig. 4.21. The correction factors and ratios of unfolded to reconstructed MC are shown as a check that the unfolding procedure is working correctly, not as a check of closure.

4.5.6 Dijet Azimuthal Distributions C_{12}

Distributions of the azimuthal correlations C_{12} of two jets are constructed from the leading and sub-leading jet kinematics. In pp and $p+Pb$ data, a trigger is required, and the leading jet is required to be in the trigger's pseudorapidity and transverse momentum range. In the dijet system there is a combinatoric contribution which comes from multi-parton scattering in both pp and $p+Pb$. This is corrected for by fitting to a constant in the range $0 < |\Delta\phi| < 1$, and subtracting the result on the full range $0 < |\Delta\phi| < \pi$. The effect of the combinatoric subtraction (CS) is small, as can be seen in Fig. 4.22, where C_{12} distributions with and without subtraction are shown, along with W_{12} and I_{12} results respectively. This is done at the reconstructed and truth levels in the same manner. The $\Delta\phi$ distributions are then normalized by the leading jet p_T spectra counts, fitted to measure the widths, and integrated to measure the yields.

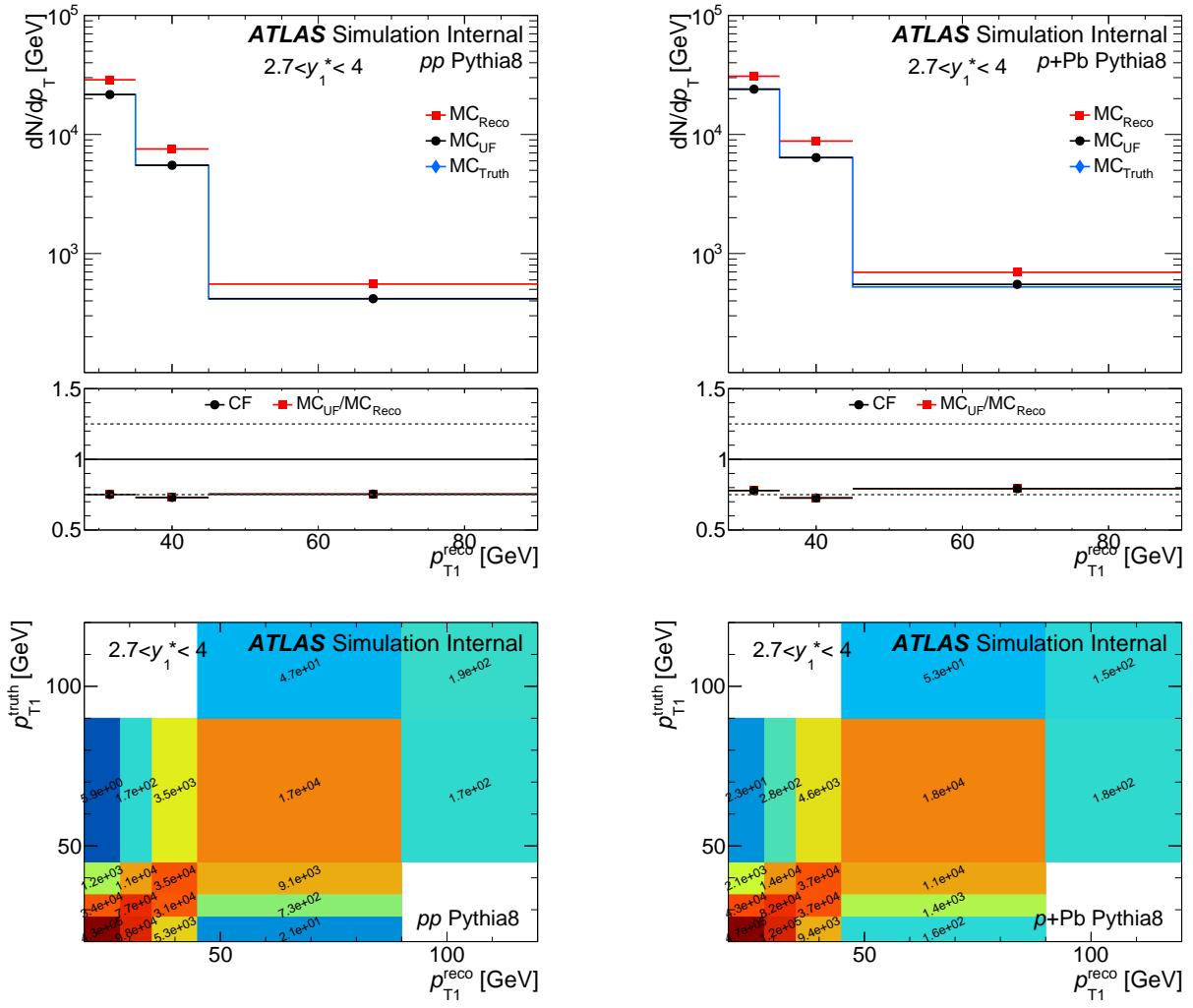


Figure 4.21: Reconstructed and truth jet p_T spectra distributions (top plot), the resulting correction factors (middle plot) and the p_T response matrix (bottom plot). Results shown for pp MC samples (left) and $p+Pb$ MC samples (right).

4.5.7 Re-weighting C_{12} Distributions

The weights for C_{12} distributions in both pp and $p+Pb$ MCs are derived as the ratios of Data to MC C_{12} distributions. This way, the p_T dependence of the azimuthal correlation distributions can be eliminated and only residual differences in shapes between data and MC distributions need to be accounted for. The pp MC C_{12} weights in all combinations of $p_{T,1}$ and $p_{T,2}$ and increasing bins in y_2^* are shown in Fig. 4.23 as a function of $\Delta\phi$. In such fine binning the weights have very high statistical fluctuations but they are invariant in p_T , so they can be combined to form weights only depending on y_2^* , as shown on the left of Fig. 4.25. To account for the still high statistical fluctuations in the tail of the distributions, the points are also smoothed.

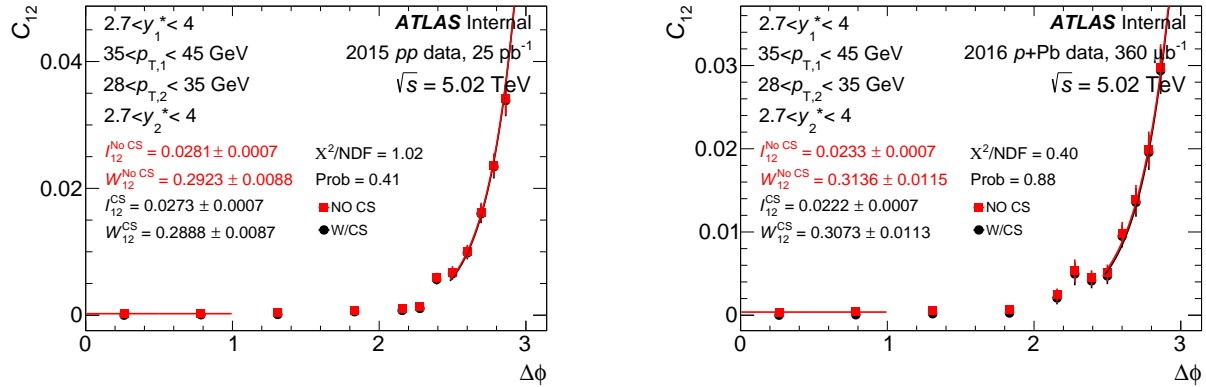


Figure 4.22: C_{12} distributions for pp and $p+\text{Pb}$ data showing the effects of the combinatoric subtraction. Red points are C_{12} distributions without combinatoric subtraction, black points are the same distributions with combinatoric subtraction. Shown from $0 < \Delta\phi < 1$ is the fit to the tail of the C_{12} distribution. The analysis uses combinatoric subtraction by default.

The $p+\text{Pb}$ C_{12} weights are evaluated with the same method. The $p+\text{Pb}$ MC C_{12} weights in all combinations of $p_{T,1}$ and $p_{T,2}$ in increasing bins in y_2^* are shown in Fig. 4.24, and the combined weights are shown on the right of Fig. 4.25, all as a function of $\Delta\phi$. The C_{12} weights are consistent with unity near the peak of C_{12} distributions, where the effect of re-weighting is largest.

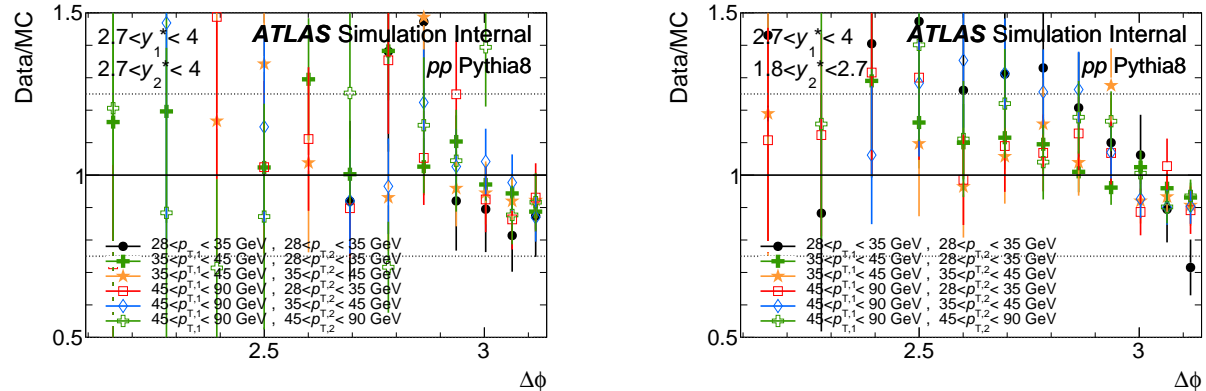


Figure 4.23: pp MC C_{12} weights shown for increasing bins of y_2^* and all possible combinations of $p_{T,1}$ and $p_{T,2}$. Weights have high statistical fluctuations but are invariant in p_T .

To properly use the re-weighting in the unfolding procedures, the shapes of re-weighted reconstructed MC distributions should be checked against those in data. There is not expected to be a complete match because the re-weighting is done as a function of truth kinematics, but it should pull the reconstructed distribution towards the data. Comparisons of the re-weighted and default MC distributions to the data are shown in Fig. 4.26 for pp and Fig. 4.27 for $p+\text{Pb}$ C_{12} distributions. The ratio of the data to re-weighted MC

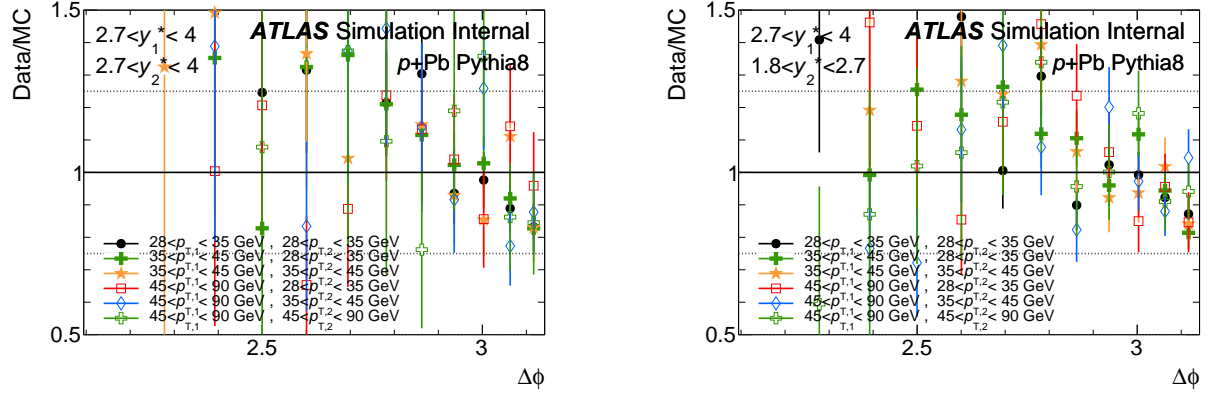


Figure 4.24: $p+Pb$ MC C_{12} weights shown for increasing bins of y_1^* and all possible combinations of $p_{T,1}$ and $p_{T,2}$. Weights have high statistical fluctuations but are invariant in p_T .

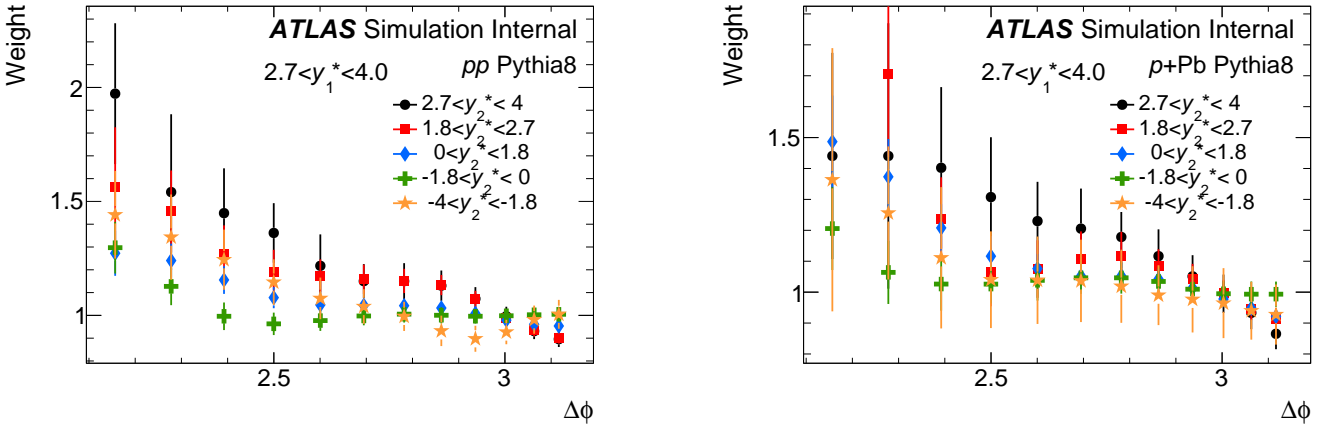


Figure 4.25: pp (left) and $p+Pb$ (right) MC samples C_{12} weights for combined p_T bins, now shown only in bins of y_2^* .

is constant in $\Delta\phi$, indicating a consistent shape. The ratio is fitted to a constant in a range where there is sufficient statistical precision ($2.5 < \Delta\phi < \pi$). In order to test fit quality, probability distributions of the fit results are shown for pp and $p+Pb$ in Fig. 4.28. The probability distributions are flat indicating a good fit to a constant function.

4.5.8 Fitting of C_{12} Distributions

The unfolded jet p_T spectra and $dN_{1,2}/d\Delta\phi$ are further used to evaluate C_{12} distributions both in pp and $p+Pb$ collisions using the procedure described until this point. The C_{12} distributions are then fitted by a

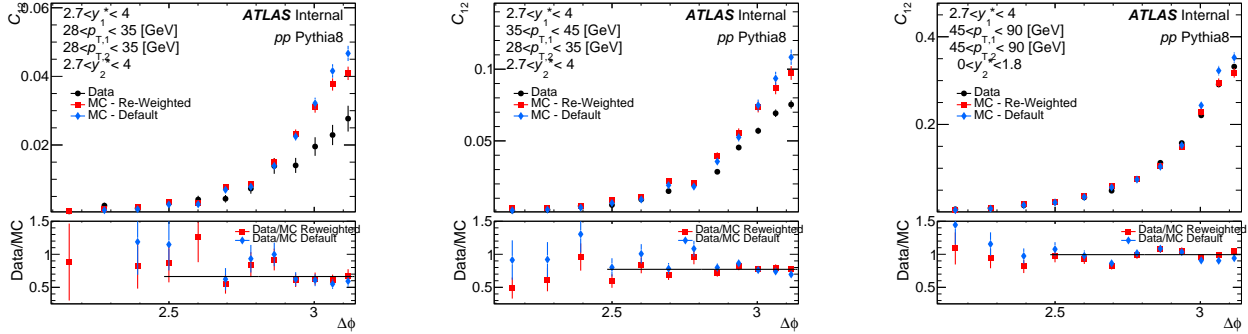


Figure 4.26: $\Delta\phi$ distributions for pp data and MC. For MC, both re-weighted and default reconstructed distributions are shown. The re-weighting makes the shapes flat in $\Delta\phi$ as indicated by the constant ratio.

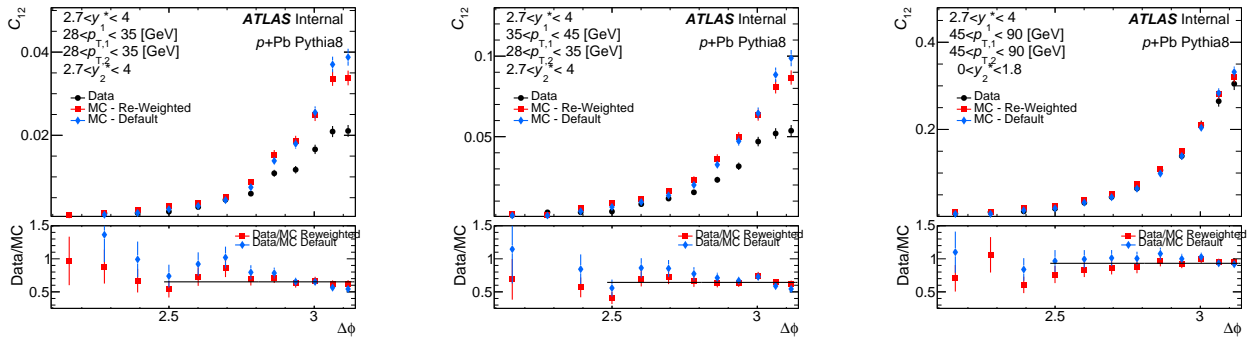


Figure 4.27: $\Delta\phi$ distributions for $p+Pb$ data and MC. For MC, both re-weighted and default reconstructed distributions are shown. The re-weighting makes the shapes flat in $\Delta\phi$ as indicated by the constant ratio.

double-exponential distribution convoluted with a Gaussian function:

$$f(\Delta\phi) = \int_{-\infty}^{\infty} d\delta \frac{e^{-\delta^2/2\sigma^2}}{\sqrt{8\pi\sigma^2\tau^2}} e^{-|\Delta\phi - \delta|/\tau} \quad (4.6)$$

where τ is the inverse slope of the exponential component and σ is the width of the Gaussian distribution. All parameters are required to be positive. Evaluating the convolution of the Gaussian and double exponential functions, the resulting fit function used in the analysis is:

$$f(\Delta\phi) = A \frac{e^{\sigma^2/2\tau^2}}{2\tau} \left(\frac{1}{2} e^{\Delta\phi/\tau} \text{Erfc} \left(\frac{1}{\sqrt{2}} \left[\frac{\Delta\phi}{\sigma} + \frac{\sigma}{\tau} \right] \right) + e^{-\Delta\phi/\tau} \left[1 - \frac{1}{2} \text{Erfc} \left(\frac{1}{\sqrt{2}} \left[\frac{\Delta\phi}{\sigma} - \frac{\sigma}{\tau} \right] \right) \right] \right), \quad (4.7)$$

where A is the overall scaling factor. From the fit function, the quantity chosen as the width is the second moment, or root-mean-square (RMS) of the probability density function in Eq 4.6:

$$W_{12} = RMS(C_{12}) = \sqrt{2\tau^2 + \sigma^2}. \quad (4.8)$$

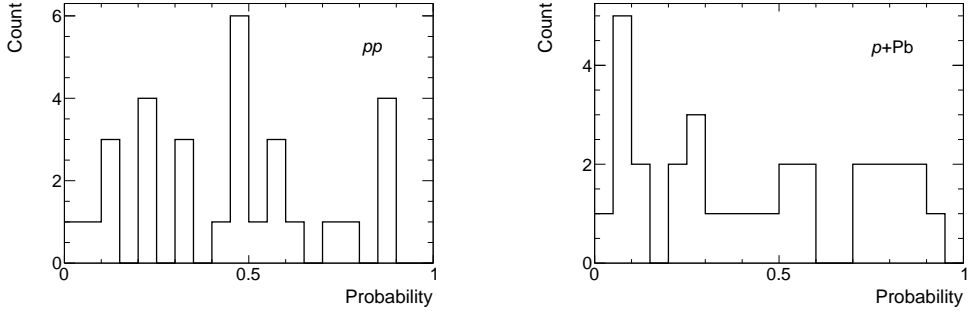


Figure 4.28: Probability distribution for constant fits to ratio of re-weighted reco MC to data $\Delta\phi$ distributions. Shown for pp (left) and $p+\text{Pb}$ (right) MCs.

The fitting procedure is performed for $2.5 < \Delta\phi < \pi$, and is similar to the one used in a previous dijet measurement [85]. However, the convolution of the Gaussian and double exponential functions is found to better describe the data around the peak of the C_{12} distributions than a pure exponential function. A fitting procedure is chosen rather than directly evaluating the RMS relative to π in order to minimize the impact of statistical fluctuations. The fit is performed for $2.5 < \Delta\phi < \pi$, similarly to the phase-space used in a previous dijet measurement [85]. Fitting is chosen rather than directly evaluating the RMS relative to π in order to minimize the impact of statistical fluctuations.

4.5.9 Unfolding C_{12} Distributions

When filling the truth and reconstructed distributions in either pp or $p+\text{Pb}$, the leading jet weights shown in Fig. 4.19, in addition to the p_T invariant C_{12} weights shown in Fig.s 4.25 for pp and $p+\text{Pb}$ samples are applied in product. Using the re-weighted truth and reconstructed C_{12} distributions, along with the respective re-weighted response matrices, new correction factors are then derived using the bin-by-bin procedure described earlier. C_{12} distributions for truth, reconstructed, and unfolded pp MC in two different bins of $p_{T,1}$ are shown on the left of Fig. 4.29, along with the correction factors and respective response matrices. Similarly, two different azimuthal correlation distributions for truth, reco, and unfolded $p+\text{Pb}$ MC distributions in different bins of $p_{T,1}$ are shown on the right of Fig. 4.29, along with the correction factors and respective response matrices. All of the correction factors derived from pp and $p+\text{Pb}$ MC samples are shown in Appendices C and D, respectively.

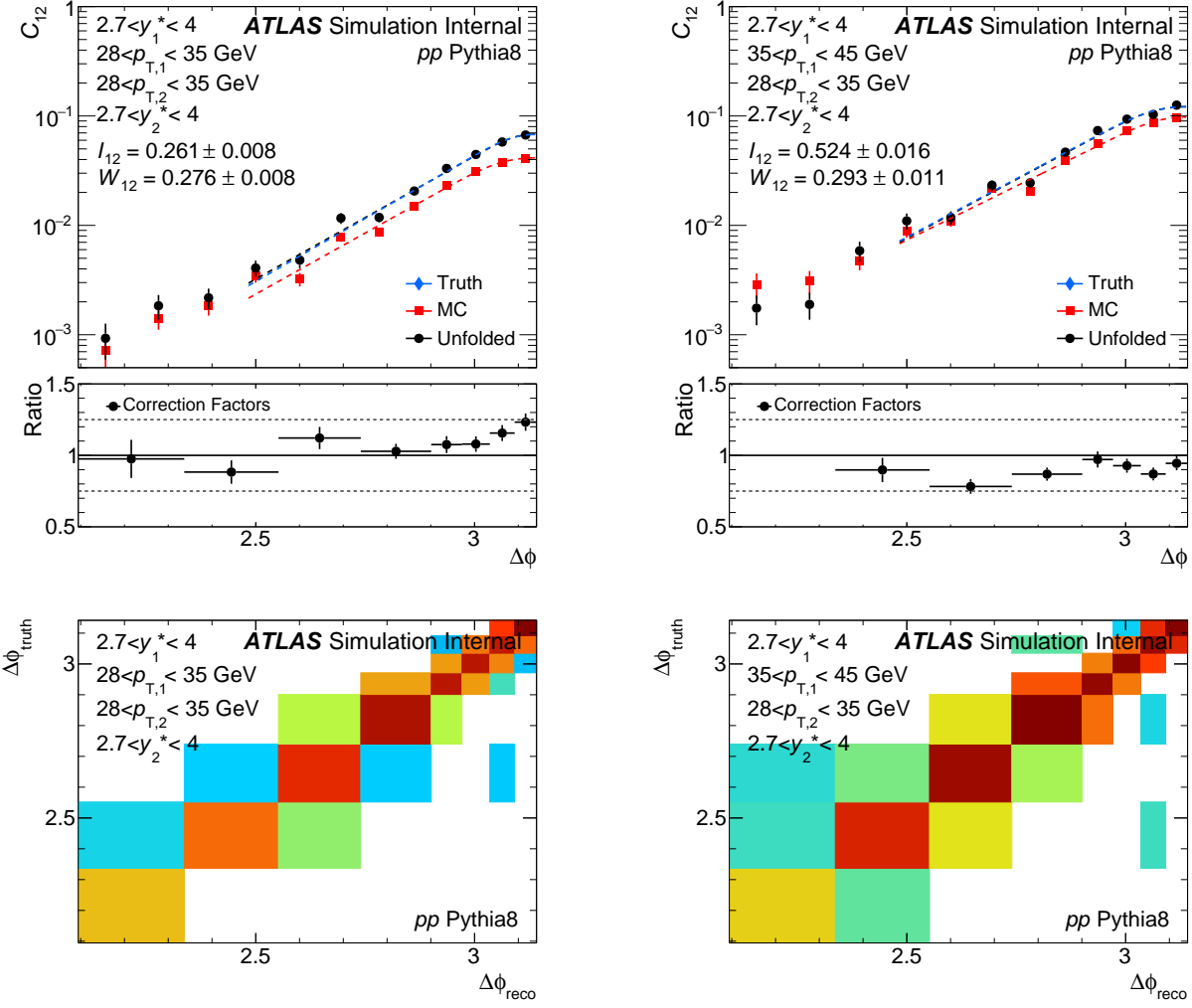


Figure 4.29: MC reconstructed, truth, and unfolded C_{12} distributions for two different bins of $p_{T,1}$, with correction factors (top row) and respective response matrices (bottom row) for pp MC samples (left) and $p+Pb$ MC samples (right).

4.5.10 MC Closure Test

As a check of the unfolding procedure, the MC reconstructed results are unfolded using the derived correction factors. Unfolded reconstructed MC distributions should resemble those at the generator level (truth level). The comparison of the pp MC truth and unfolded C_{12} distributions, and the respective ratios are shown in Fig. 4.30 in bins of $p_{T,1}$ and $p_{T,2}$. Similarly, a comparison of I_{12} in the pp MC truth and unfolded distributions is shown in Fig. 4.32. The ratios between unfolded and truth results are consistent with unity within statistical uncertainties indicating there is good closure between the unfolded and truth results. The comparison of the $p+Pb$ MC truth and unfolded widths, and the respective ratios are shown in Fig. 4.31 in

bins of $p_{T,1}$ and $p_{T,2}$. The similar comparison of conditional yields is shown in Fig. 4.33. As in the case of the pp system, the ratios between unfolded and truth results in the $p+Pb$ system are consistent with unity within statistical uncertainties indicating there is good closure between the unfolded and truth results. The few fluctuations seen in the ratios are statistical in origin.

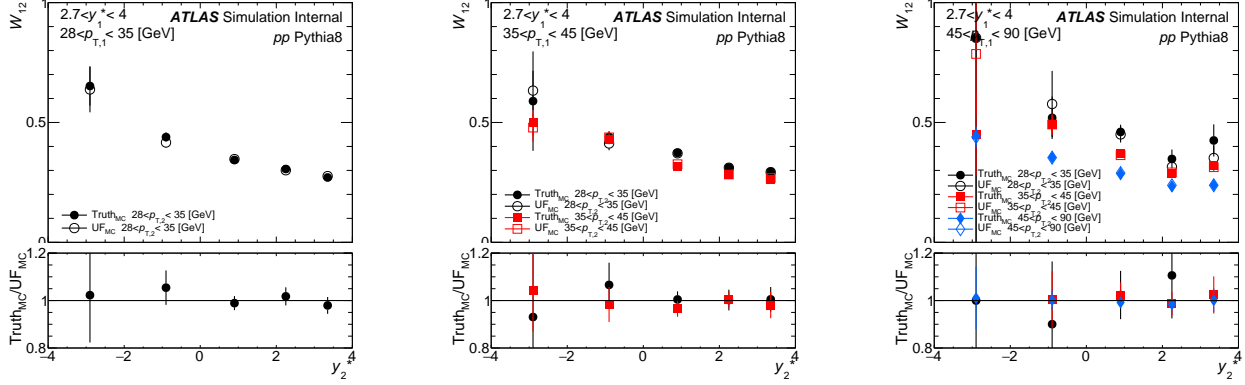


Figure 4.30: Comparison of widths from fits to C_{12} distributions between unfolded and truth results for the pp MC. Ratios are consistent with unity, indicating good unfolding closure.

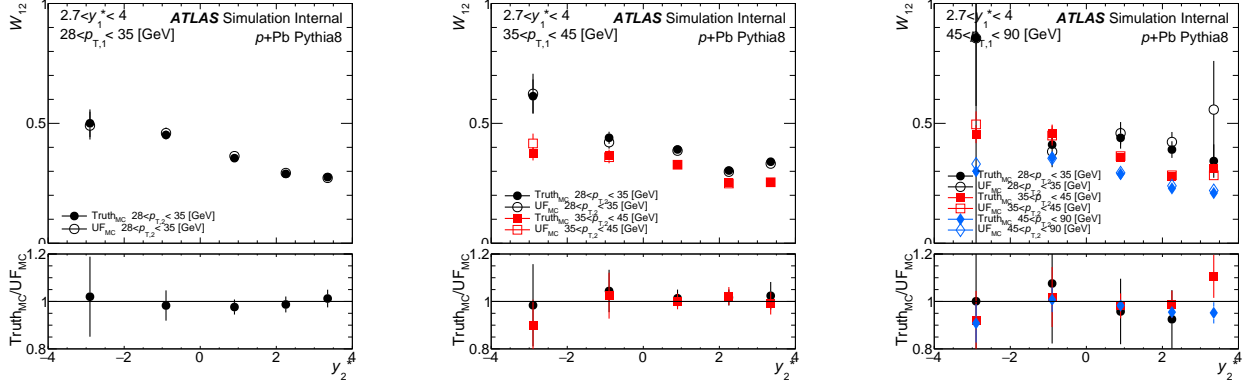


Figure 4.31: Comparison of widths fits to C_{12} distributions between unfolded and truth results for the $p+Pb$ MC. Ratios are consistent with unity, indicating good unfolding closure.

As an additional closure test, the jet p_T spectra and C_{12} correction factors derived from the PYTHIA8 MC were applied to reconstructed jets from the HERWIG++ MC. A comparison of unfolded and truth C_{12} and I_{12} between the pp HERWIG++ and PYTHIA8 MCs are shown in Fig. 4.34. For the $p+Pb$ results, there is no additional MC so this test was only done on the pp MC. Ratios of unfolded to truth distributions indicate good closure. From Table A.2 in the appendix, it is evident that the statistics in the pp HERWIG++ MC is roughly 50% of the pp PYTHIA8 MC, so the resulting fluctuations are seen as statistical.

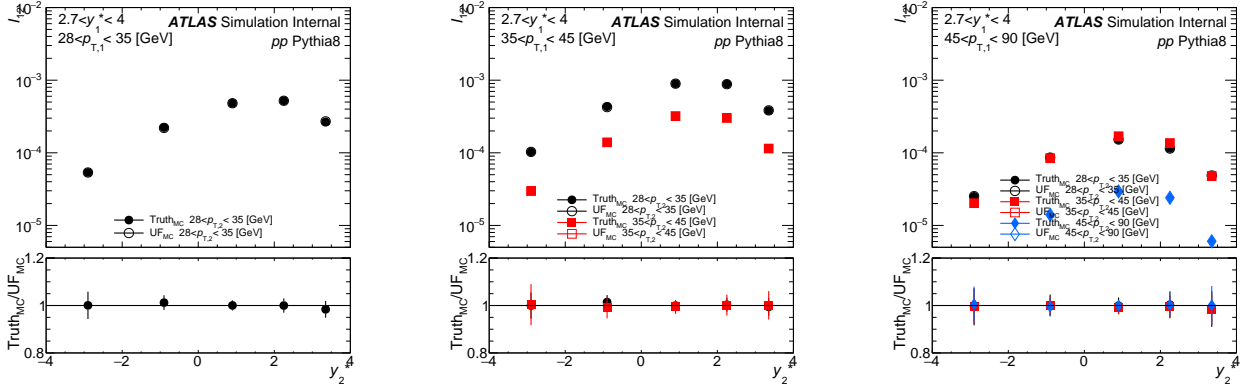


Figure 4.32: Comparison of I_{12} between unfolded and truth results for the pp MC. Ratios are consistent with unity, indicating good unfolding closure.

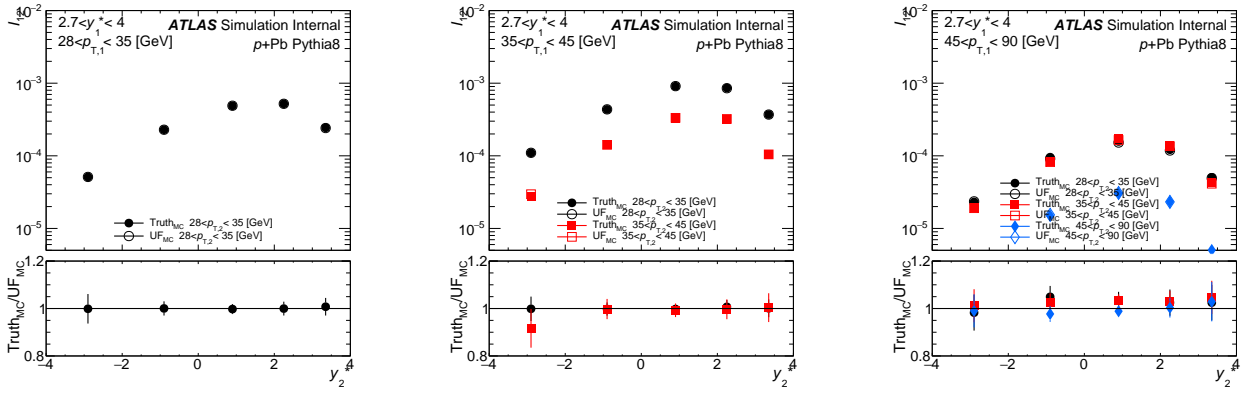


Figure 4.33: Comparison of I_{12} between unfolded and truth results for the $p+Pb$ MC. Ratios are consistent with unity, indicating good unfolding closure.

4.5.11 Isolation Requirements

Initially, jets were required to be isolated such that if two jets were separated by a distance of $\Delta R < 0.2$, they were not considered in the event. This was done to avoid potential split jet contributions to the result. However, when comparing with NLO QCD, isolation requirements cause complications and as a result they were removed. The effect of the isolation requirement on C_{12} and I_{12} distributions is very minor, as shown in Appendix E.

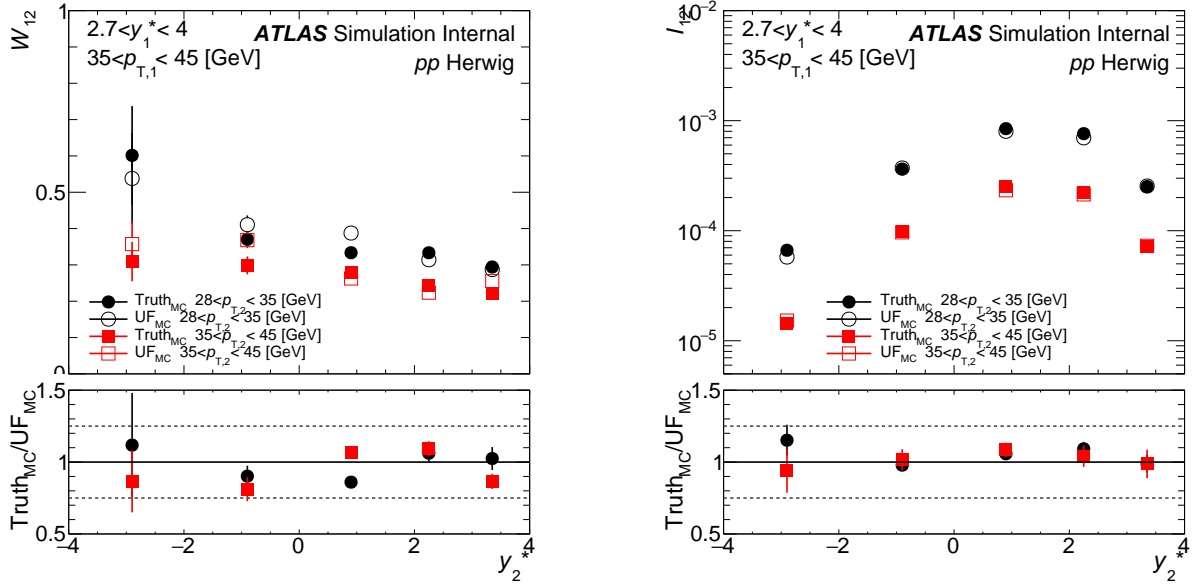


Figure 4.34: Comparison of C_{12} (left) and I_{12} (right) between unfolded and truth results for the pp HERWIG++ MC. Unfolding is done using correction factors derived from the PYTHIA8 MC. Ratios are consistent with unity, indicating good unfolding closure.

4.6 Systematic Uncertainties

4.6.1 Overview

This section gives an overview of the major sources of systematic uncertainties on the pp and $p+Pb$ azimuthal angular correlations. Careful treatment of these known variations is necessary for a precise physics result.

The systematic uncertainties in the measurement originate from:

- Jet energy scale
- Jet energy resolution
- Jet Position resolution
- Unfolding of jet p_T spectra and C_{12} distributions
- Fitting of the C_{12} distributions
- Differences in conditions between data and MC samples

The systematic uncertainties have been evaluated for the C_{12} distributions as a function of y^* for pp and $p+Pb$ collisions. For each source of systematic uncertainties, the entire unfolding and fitting procedure is repeated (1D unfolding of the C_{12} distributions as a function of $\Delta\phi$, and the 1D unfolding of leading jet p_T

spectra as a function of jet p_T) and the W_{12} , I_{12} , and ratios of these distributions, ρ_W^{pPb} and ρ_I^{pPb} , in $p+\text{Pb}$ and pp collisions are re-evaluated. The difference between the varied and nominal distributions is used as an estimate of the uncertainty. All sources of systematic uncertainty discussed in this section have been combined in quadrature to obtain the total systematic uncertainty.

4.6.2 Systematic Uncertainty Due to the Jet Energy Scale

The systematic uncertainty due to the JES is determined from *in situ* studies of the calorimeter response [83, 86, 84, 87], and studies of the relative energy scale difference between the heavy ion style jet reconstruction procedure [86] and the procedure used in pp collisions [88]. For the pp and $p+\text{Pb}$ JES uncertainties, part a globally reduced set of nuisance parameters derived by the JetEtMiss group are used. The heavy ion specific components are from the a cross calibration and the jet flavor uncertainties at 5.02 TeV. The latter uncertainties come from the fact that jets from different quark flavors will have minor differences in jet shape and fragmentation, but in the analysis all jets are treated identically. As a result, a systematic uncertainty must be introduced, and should also account for the affect of the boost in $p+\text{Pb}$ collisions. For each component of the variation the response matrices are regenerated with the shifted p_T^{jet} :

$$p_T^{*,\text{reco}} = p_T^{\text{reco}}(1 \pm U^{\text{JES}}(p_T, \eta)). \quad (4.9)$$

where U^{JES} is the uncertainty in the JES. The data is then re-unfolded with these response matrices and the variation in the widths of C_{12} distributions is taken as the systematic uncertainty.

4.6.3 Additional Systematic Uncertainty in $p+\text{Pb}$ Due to the Jet Energy Scale

The JES in the 2016 $p+\text{Pb}$ MC with data overlay differs from the 2016 $p+\text{Pb}$ signal only MC, and from the 2015 pp MC. The JES for the different configurations is show in in the top plots Fig. 4.35, and the difference in the JES between the overlay and signal MC samples, and the difference between the signal and pp MC samples is shown in the bottom plots. These two differences are used as an additional systematic on the JES in $p+\text{Pb}$, and are added together in quadrature.

The absolute effect of the additional systematic on the final uncertainties on C_{12} and I_{12} distributions is shown in Fig. 4.36, where the total uncertainty before the new JES systematics is compared to the total uncertainty with the new JES systematics. All figures showing the relative effect of the new systematics on C_{12} and I_{12} distributions are shown in Fig. F.1 and Fig. F.2 of the appendix. Generally, the effect is below 3%, with some bins having up to a 5% effect. This additional uncertainty is acceptable for the analysis and

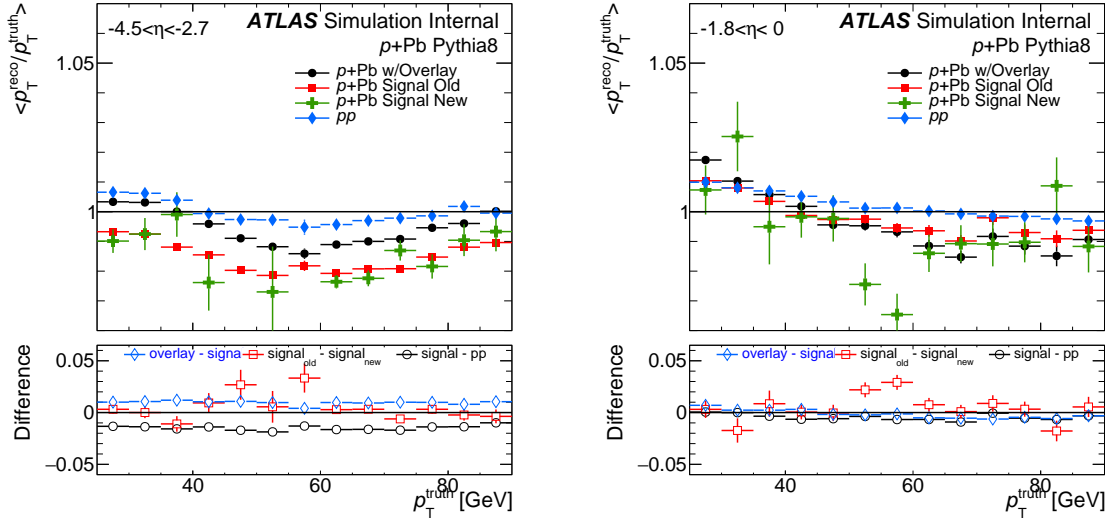


Figure 4.35: Top row shows the JES in the $p+\text{Pb}$ MC with overlay (black points), $p+\text{Pb}$ signal only MC (red points), and pp MC (blue points). Green points show recent and small validation sample where the HEC issue was fixed. This is done for testing purposes and does not have a significant effect. Bottom row shows the difference between the overlay and signal (empty blue points) and between the signal and pp (empty black points). Shown for forward, proton going direction (left plot) and barrel region (right plot). The differences are used as an additional JES systematic in $p+\text{Pb}$.

does not change the results sufficiently.

The effect of the additional systematic on ρ_W^{pPb} and ρ_I^{pPb} is shown in Fig. 4.37, where the total uncertainty on the ratio before the new JES systematics is compared to the total uncertainty on the ratio with the new JES systematics. All figures showing the relative effect of the new systematics on ρ_W^{pPb} and ρ_I^{pPb} are shown in Fig. F.3 and Fig. F.4 of the appendix. The effect is minor, not increasing any total systematic uncertainty by more than 2%.

4.6.4 Systematic Uncertainty Due to the Jet Energy Resolution

The uncertainty due to the JER is evaluated by repeating the unfolding procedure with modified correlation matrices, where an additional contribution is added to the resolution of the simulated p_T^{jet} using a Gaussian smearing procedure [88]. The smearing factor is evaluated using an *in situ* technique in 13 TeV pp data involving studies of dijet energy balance [89]. The jet p_T^{reco} is then smeared by

$$p_T^{*,\text{reco}} = p_T^{\text{reco}} \times \mathcal{N}(1, \sigma_{\text{JER}}^{\text{eff}}), \quad (4.10)$$

where $\mathcal{N}(1, \sigma_{\text{JER}}^{\text{eff}})$ is the normal distribution with the effective resolution $\sigma_{\text{JER}}^{\text{eff}} = \sqrt{(\sigma_{\text{JER}} + \sigma_{\text{JER}}^{\text{syst}})^2 - \sigma_{\text{JER}}^2}$.

An additional uncertainty is included to account for differences between the heavy ion style jet recon-

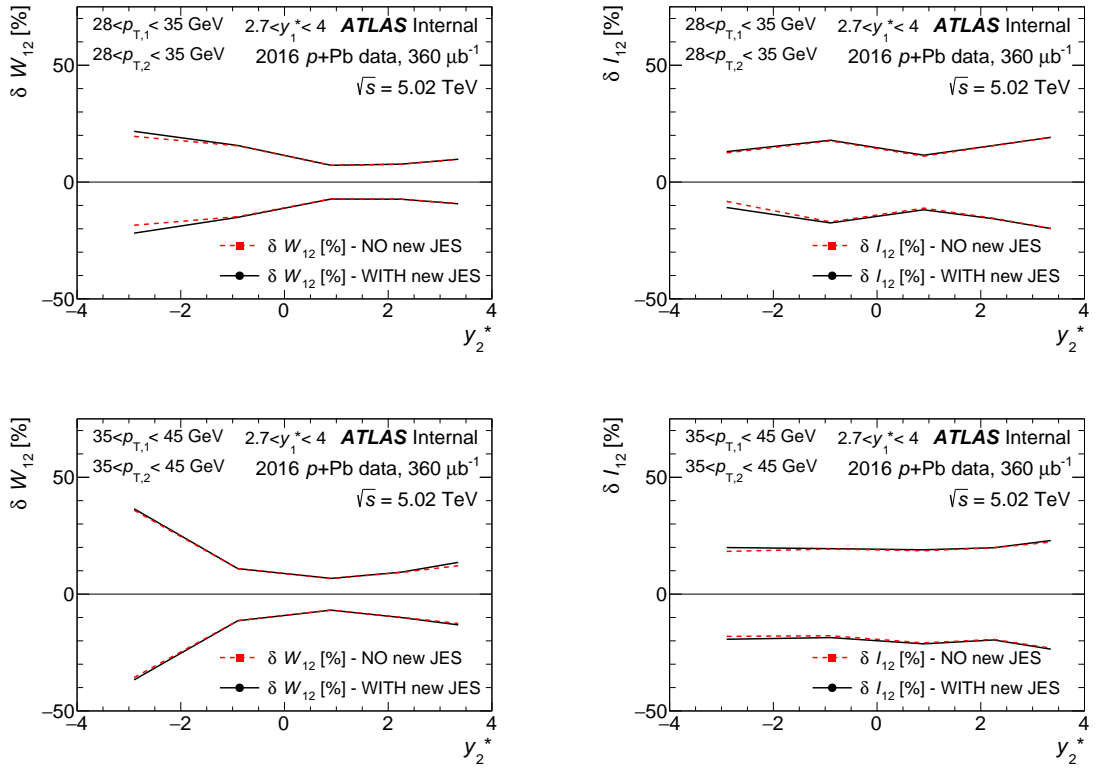


Figure 4.36: Effect on total systematic uncertainty on C_{12} (left) and I_{12} (right) after adding new JES uncertainties. Shown for two different bins of $p_{T,1}$ and $p_{T,2}$. Generally the relative effect is below 10%, with some bins reaching 25%. Fig.s in all bins of p_T and y^* are shown in Appendix F.

struction and that used in the analyses of 13 TeV pp data. The resulting uncertainty from the JER is symmetrized to account for negative variations of the JER. The size of the resulting uncertainty due to the JER on the I_{12} distributions reaches up to 30% and is typically below 10% in the W_{12} distributions.

4.6.5 Systematic Uncertainty Due to the Jet Angular Resolution

To account for the systematic uncertainties due to the disagreement between JAR in data and MC, the procedure used in previous measurements [90] based on the comparison of relative angular resolutions between calorimetric jets and track jets in the data and the MC cannot be used due to the limited pseudorapidity coverage of the ID. The uncertainty in this analysis is derived as the difference in the JARs evaluated using the two different MC generators. Jets from HERWIG++ and PYTHIA8 MC samples are used. The comparison of pseudorapidity and azimuthal angular resolutions between pp HERWIG++ and PYTHIA8 MC performance for forward and central bins of y^* are shown in Fig. 4.38. Since the $p+Pb$ MC sample utilizes the overlay procedure, ensuring that the underlying event is the same in the MC and data, the pp MC is used for the

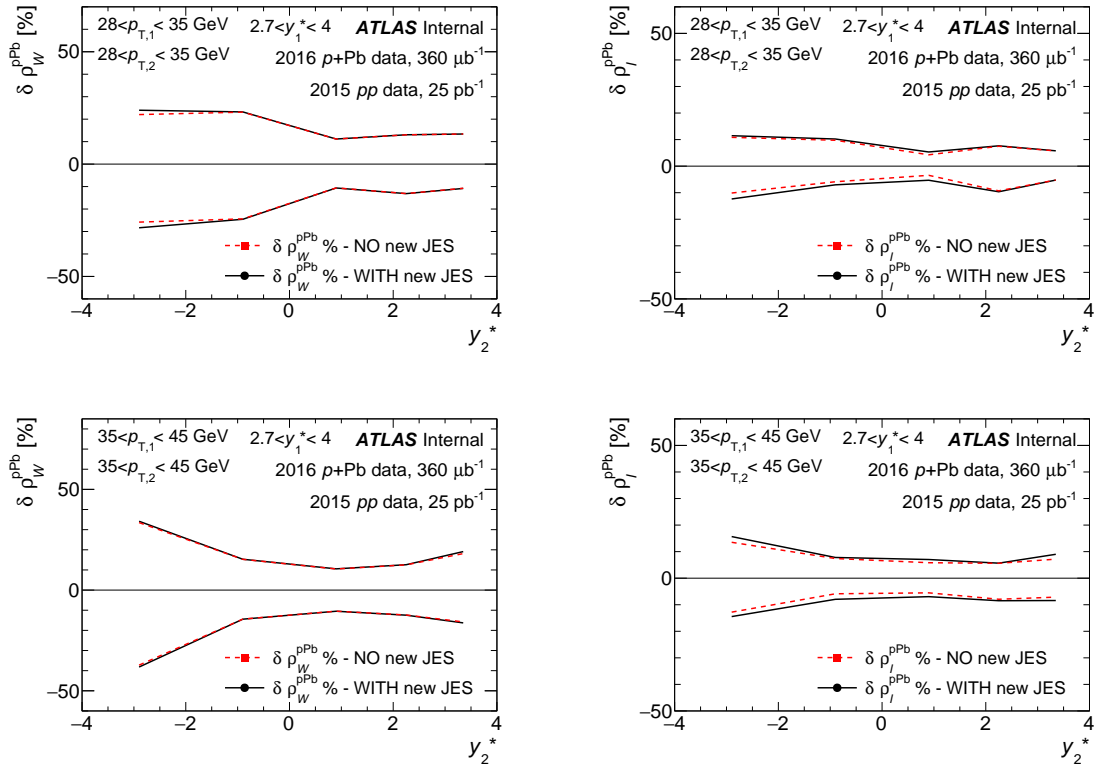


Figure 4.37: Difference between total systematic uncertainty on $\rho_W^{p\text{Pb}}$ (left) and $\rho_I^{p\text{Pb}}$ (right) before and after adding new JES uncertainties. The total systematic uncertainty on the ratio before the addition of the new JES uncertainties is shown as the dotted red line, and after the addition of the new JES uncertainties in the solid black line. Overall effect on uncertainties on the ratios is small, with the difference in uncertainties generally below 2%, with one bin reaching 5%. Fig.s in all bins of p_T and y^* are shown in Appendix F.

uncertainty on the $p+\text{Pb}$ JAR. The difference in pseudorapidity and azimuthal angular resolutions between PYTHIA8 and HERWIG++ MC samples is less than 0.5% in both the forward and central directions.

The uncertainty on the the widths of azimuthal correlation distributions associated with the jet angular resolution in η and ϕ is estimated similarly to the uncertainty in JER. A modified response matrix where the reconstructed jet angular in η and ϕ is smeared to reflect uncertainties on the JAR evaluated in previous paragraphs. The Gaussian probability density function is estimated for each jet p_T and jet y^* . The new unfolded results are compared with the original distributions and the difference is used as an estimate of the systematic uncertainty.

4.6.6 Systematic Uncertainty Due to Unfolding

The systematic uncertainty associated with the unfolding procedure is connected with its sensitivity to the choice of input distributions. The default version of the unfolding uses the MC reweighted such that the

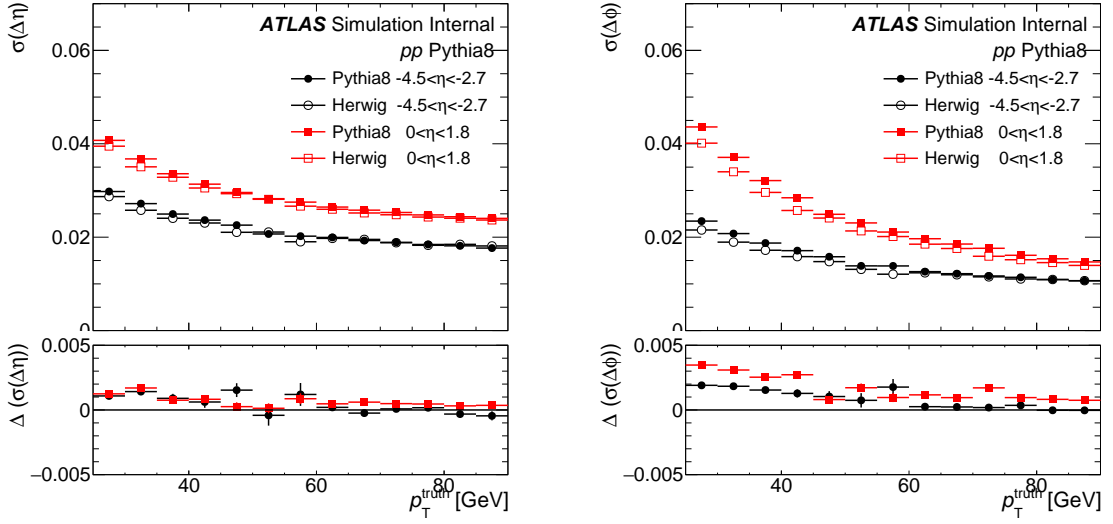


Figure 4.38: Comparison of angular resolutions in η (left) and ϕ (right) between PYTHIA8 and HERWIG++.

reconstructed MC is matched to the reconstructed data in the shapes of the C_{12} distributions. Conservatively, the systematic is evaluated by using the MC without re-weighting. A comparison of correction factors with and without re-weighting is shown for two different phase space bins for the pp and $p+\text{Pb}$ MCs in Fig. 4.39. The effect on the correction factors is minor (below 5%) and the resulting uncertainty on the measurement is also below 5%. This indicates that the correction factors are robust against re-weighting.

4.6.7 Systematic Uncertainty Due to Fitting

The systematic uncertainty due to the fitting to C_{12} distributions is associated with the sensitivity of the measured widths to the choice of fit range. The default fitting is in the range $2.5 < \Delta\phi < \pi$, and a varied fit range of $2.1 < \Delta\phi < \pi$ is used to evaluate the systematic uncertainty. This systematic only affects the C_{12} widths, not the normalized yields where no fitting is used. Resulting widths, with two different fit ranges are shown for pp and $p+\text{Pb}$ data in Fig. 4.40. The changes in the widths of azimuthal correlation distributions are below 8% in most bins. However, there are large statistical uncertainties in some fit results and the resulting statistical fluctuations in turn affect the resulting systematic uncertainty, which is related to the ratio between the results using two different fit ranges. To account for this, the ratios, shown in the bottom of Fig. 4.40, are fitted to a constant. The resulting systematic uncertainty is conservatively taken as the fit result plus error on the fit. For reference, results in all combinations of $p_{T,1}$ and $p_{T,2}$ are shown in Appendix G.

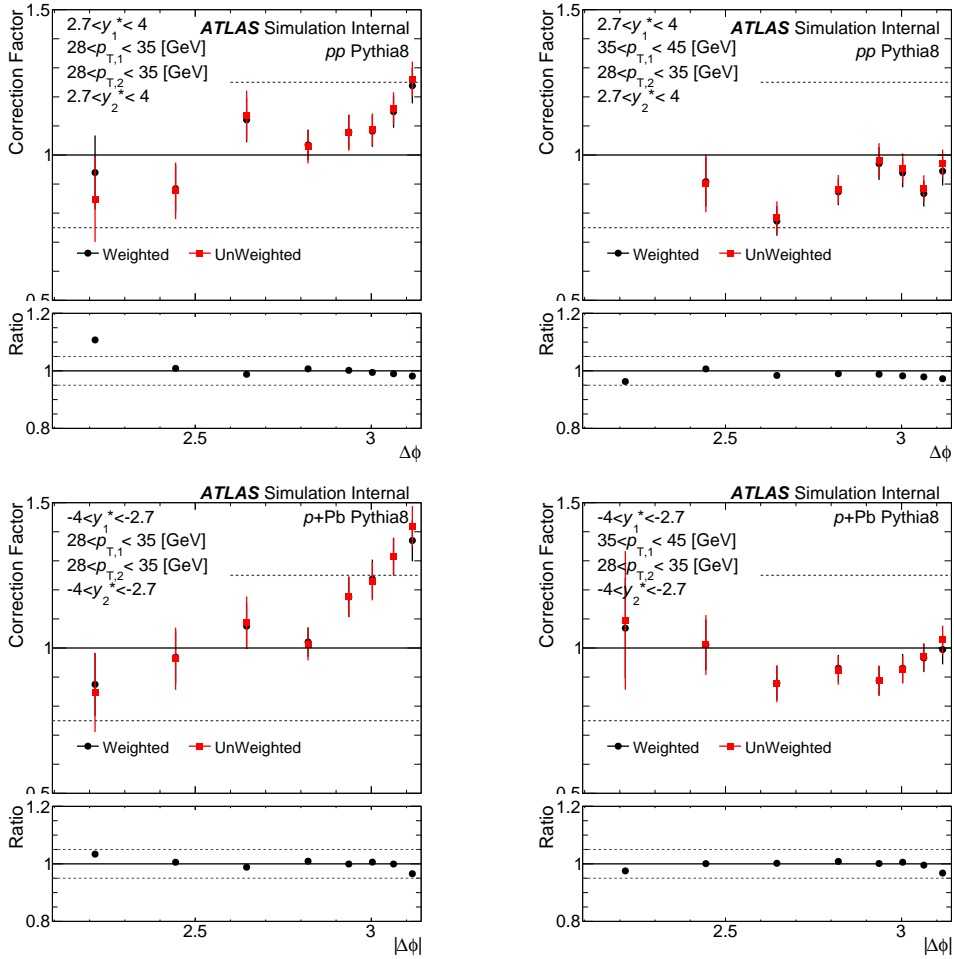


Figure 4.39: Comparison of correction factors with and without re-weighting for the pp MC (top row) and the $p+Pb$ MC (bottom row)

4.6.8 Systematic Uncertainty Due to the HEC

The systematic uncertainty associated with excluding reconstructed level jets that are in the region covered by the lead-going HEC, as discussed in Section 4.3.3, is taken by increasing excluded region by 0.1 in all directions in azimuth and pseudorapidity. This number was chosen to introduce some variation and at the same time not drastically decrease the sampled statistics. The resulting widths and yields, with default HEC region excluded, and with the increased region excluded, shown for two bin in $p_{T,2}$ for C_{12} and I_{12} in Fig. 4.41. The effect on the widths is consistent with unity, and on the yields, there is up to a 10% effect in the most negative y_2^* bin, which are the two the center-of-mass rapidity bins affected by the HEC issue.

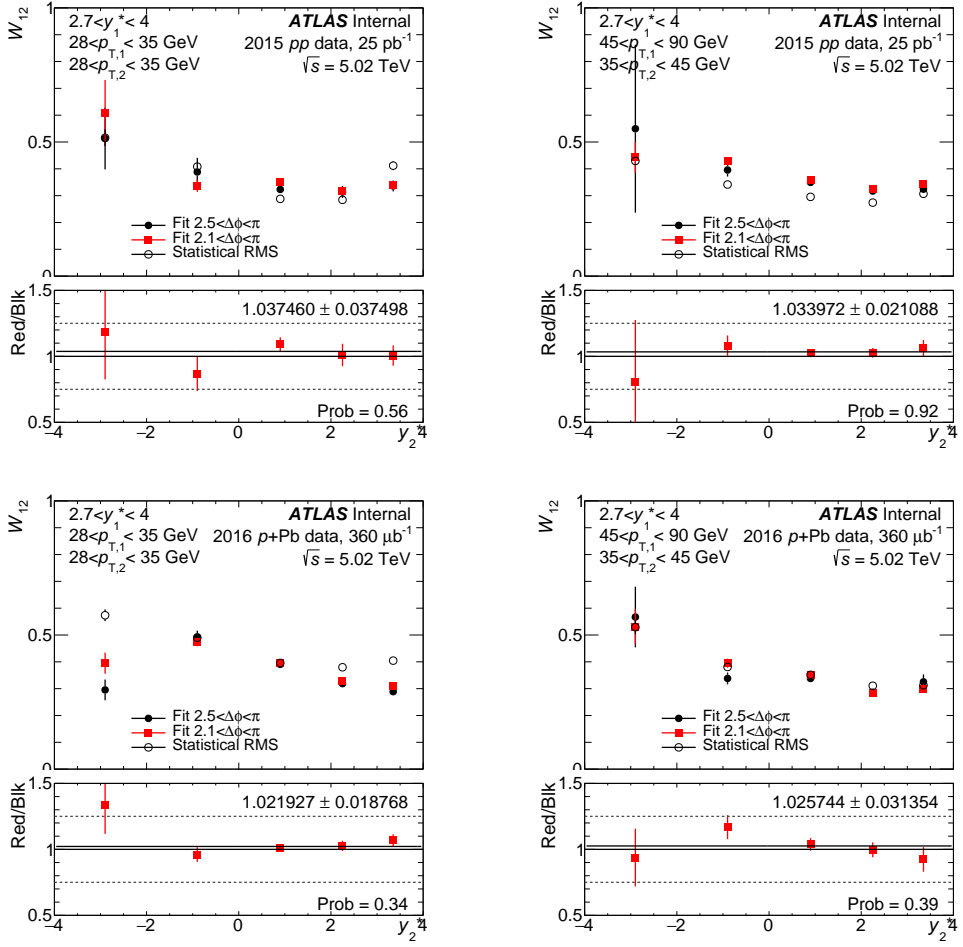


Figure 4.40: Comparison widths from fitting on two different ranges, $2.5 < \Delta\phi < \pi$ for the solid black points, and $2.1 < \Delta\phi < \pi$ for the open red points, and their respective ratios. Shown for pp data (top row) and $p+Pb$ data (bottom row). Empty black points show result of statistical RMS calculation.

4.6.9 Summary of Systematic Uncertainties

The total and individual systematic uncertainties on the pp widths are shown in 4.42, and on the pp yields in 4.43. Similarly, the total and individual systematic uncertainties on the $p+Pb$ widths are shown in 4.44, and for the yields in 4.45.

The correlations between the various systematic components are considered in evaluating the $p+Pb$ to pp ratios ρ_W^{pPb} and ρ_I^{pPb} for widths and yields respectively. The unfolding and fitting are taken to be uncorrelated between the two collision systems and are added in quadrature. The new JES and HEC detector condition systematics are present in $p+Pb$ only and by construction considered to also be uncorrelated between the two collision systems. All other uncertainties associated with the JES, JER, and JAR are taken to be correlated. The ratios are re-evaluated by applying the variation to both collision systems and the resulting variations of

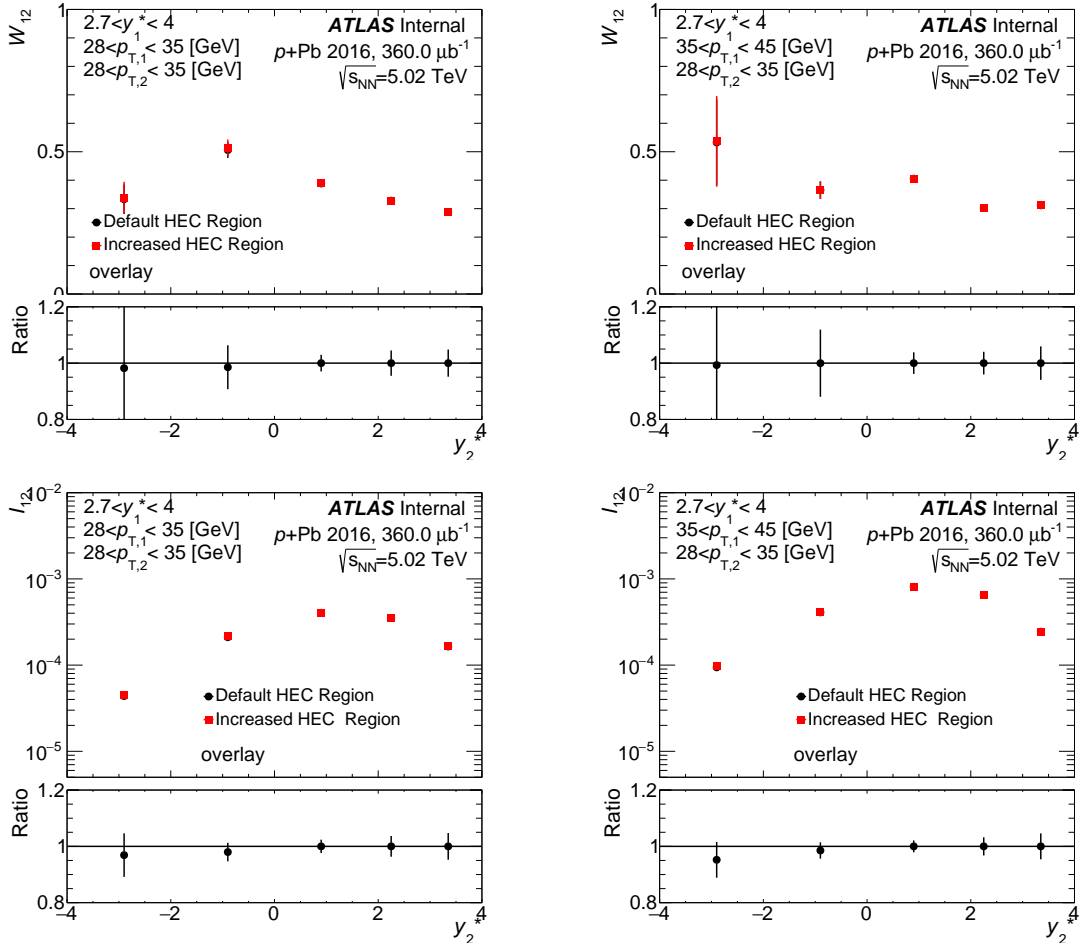


Figure 4.41: Effect of using removing jets that are in the default region that the HEC affects (black points), and with the region with 0.1 increase in all directions in azimuth and pseudorapidity (red points). The uncertainty is represented by the ratio of results using the two different excluded regions.

the ratios from their central values is used as the correlated systematic uncertainty from a given source. The summary of systematic uncertainties on $\rho_W^{p\text{Pb}}$ and $\rho_I^{p\text{Pb}}$ distributions is presented in Fig. 4.46 and Fig. 4.47, respectively. The systematic uncertainty due to the JES is dominant (up to 20%) on both $\rho_W^{p\text{Pb}}$ and $\rho_I^{p\text{Pb}}$ distributions.

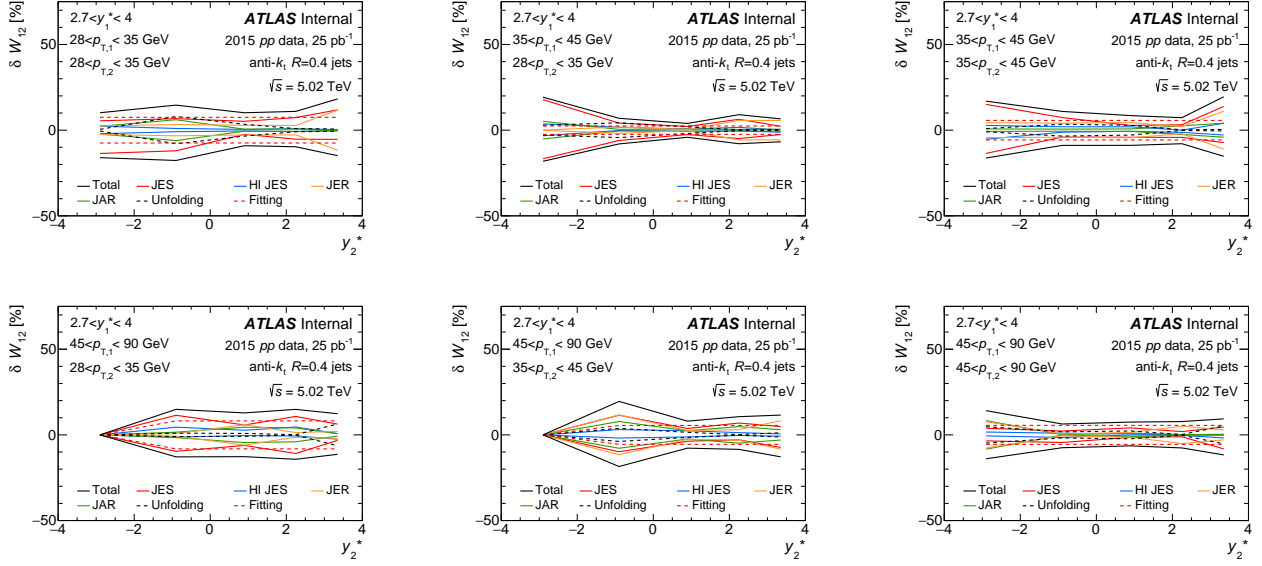


Figure 4.42: Total and individual systematic uncertainties on the widths of C_{12} distributions in pp data. Some bins have been removed due to very high statistical and systematic uncertainties in those bins.

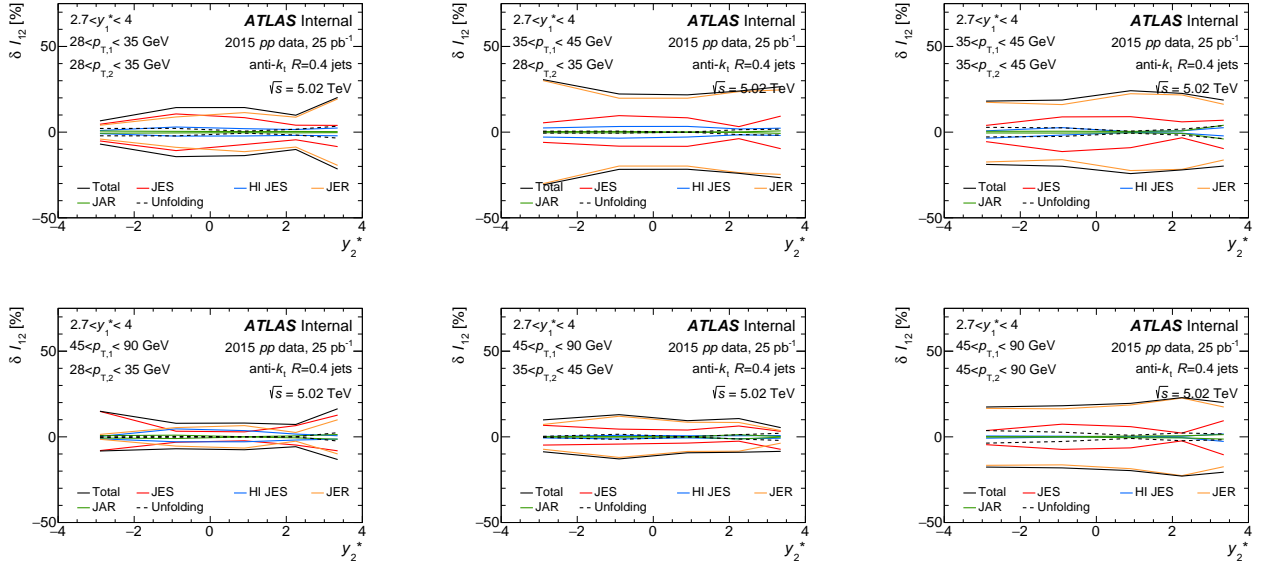


Figure 4.43: Total and individual systematic uncertainties on the dijet conditional yields in pp data.

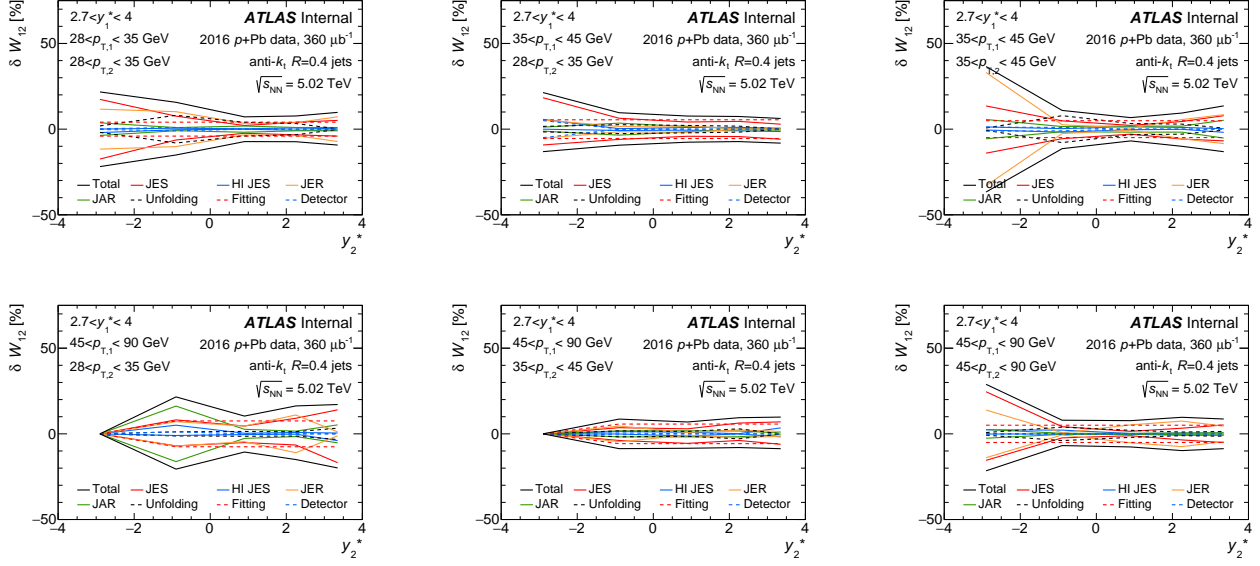


Figure 4.44: Total and individual systematic uncertainties on the widths of C_{12} distributions in $p+Pb$ data.

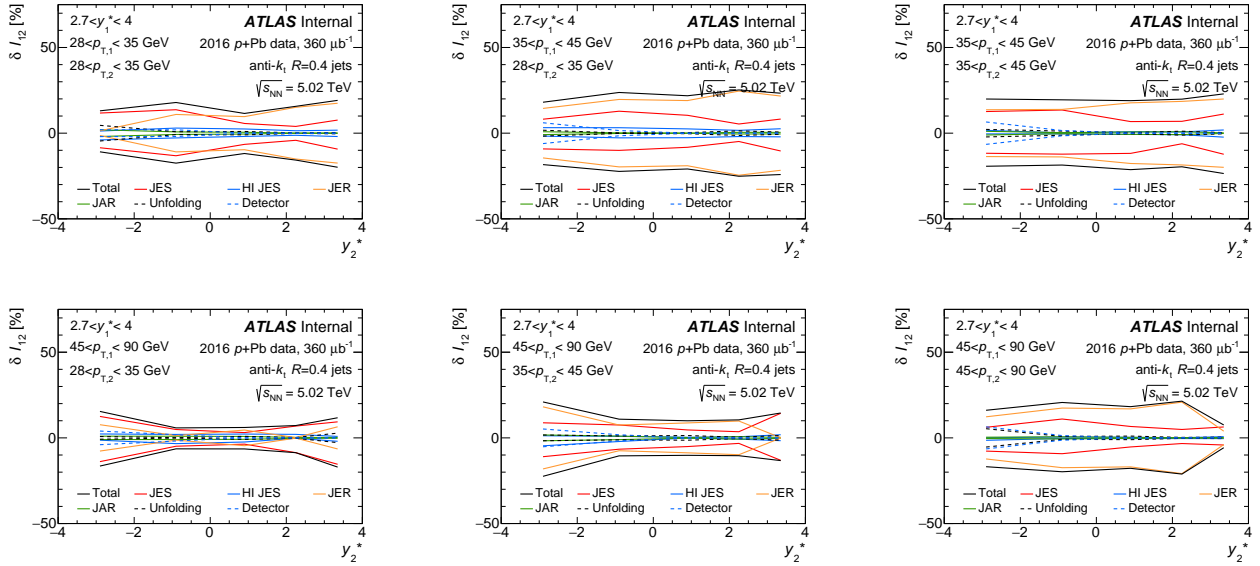


Figure 4.45: Total and individual systematic uncertainties on the dijet conditional yields in $p+Pb$ data.

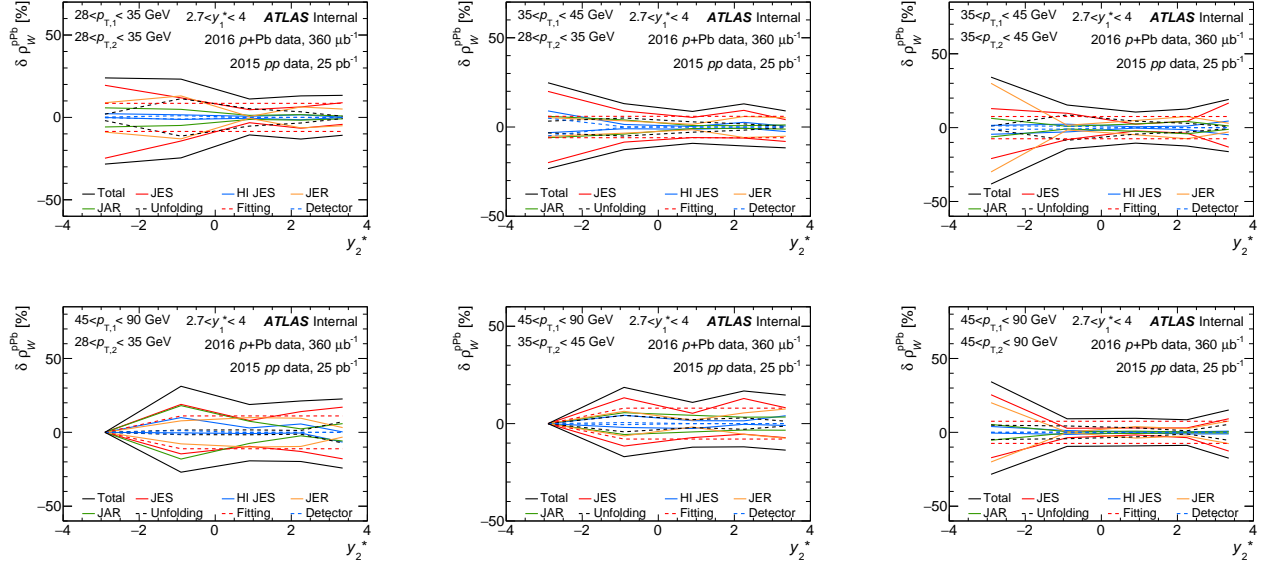


Figure 4.46: Total and individual systematics on $\rho_W^{p\text{Pb}}$. Some bins have been removed due to very high statistical and systematic uncertainties in those bins.

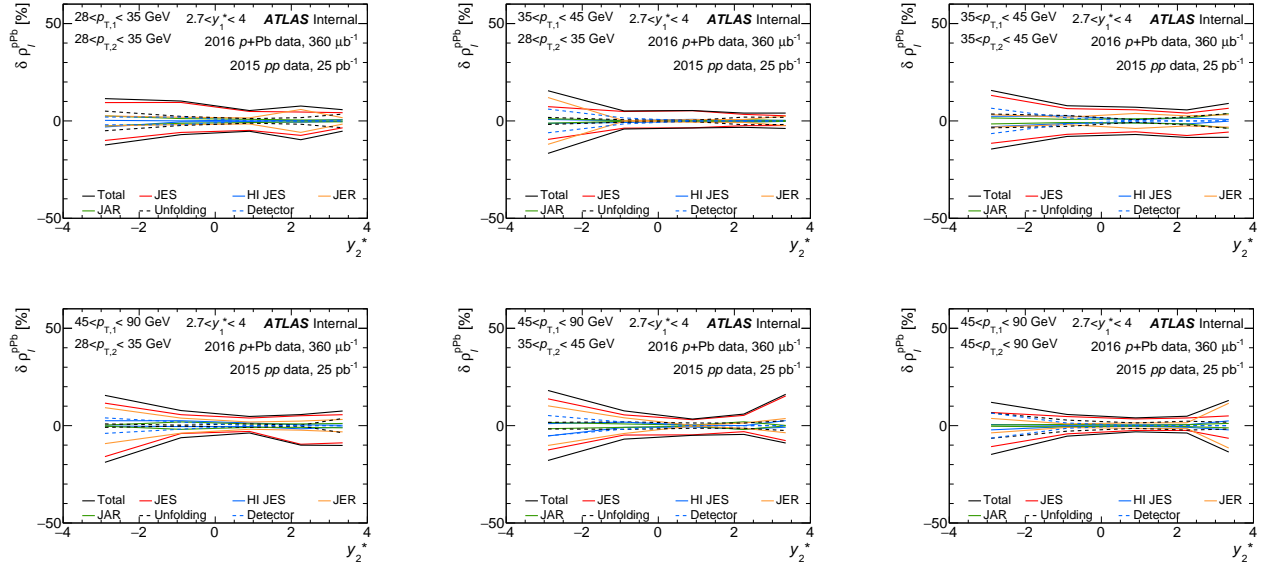


Figure 4.47: Total and individual systematics on $\rho_I^{p\text{Pb}}$. Some bins have been removed due to very high statistical and systematic uncertainties in those bins.

4.7 Results

4.7.1 C_{12} Distributions and Their Fits

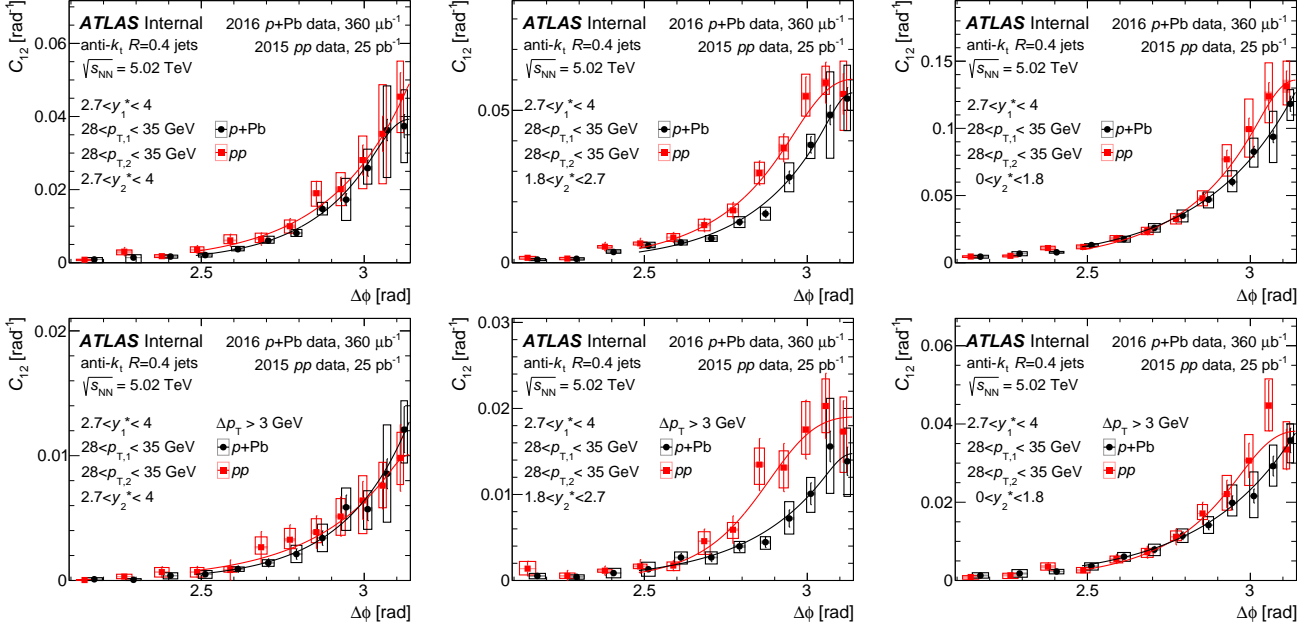


Figure 4.48: Unfolded C_{12} distributions in pp (red symbols) and $p+Pb$ (black symbols) collisions for different selections of $p_{T,1}$, $p_{T,2}$, and y_2^* as a function of $\Delta\phi$. Lines represent results of the fit (for more details see the text). Open boxes represent correlated systematic uncertainties and vertical error bars represent statistical uncertainties. Results are presented with no Δp_T requirement (top row) and with a requirement of $\Delta p_T > 3$ GeV (bottom row).

This section presents results for W_{12} and the I_{12} distributions, and ratios, $\rho_W^{p\text{Pb}}$ and $\rho_I^{p\text{Pb}}$, of these distributions in $p+Pb$ and pp collisions in order to explore the effects of saturation of gluon distribution functions. These distributions are measured for pairs of leading and sub-leading jets in transverse momentum range of $28 < p_T < 90$ GeV. Leading jets are measured in the center-of-mass rapidity region $2.7 < y_1^* < 4.0$ and sub-leading jets in the center-of-mass rapidity of $-4.0 < y_2^* < 4.0$.

Examples of unfolded C_{12} distributions with systematic uncertainties in different intervals of y_2^* , $p_{T,1}$, and $p_{T,2}$ evaluated in pp and $p+Pb$ collisions are shown in Fig. 4.48 together with the fit results. These results are presented with and without a requirement of $\Delta p_T > 3$ GeV. All the C_{12} distributions used in the analysis, with systematic uncertainties and fit result are shown for pp and $p+Pb$ collisions with and without the Δp_T requirement in Appendix H. The C_{12} distributions exhibit an exponential behavior, with a flattening, described by the Gaussian, near the peak at $\Delta\phi = \pi$. Fit quality is validated from the χ^2/NDF probability distribution shown in Figure 4.49. Since there is no physics motivation behind the fit function, a uniform probability distribution is not expected.

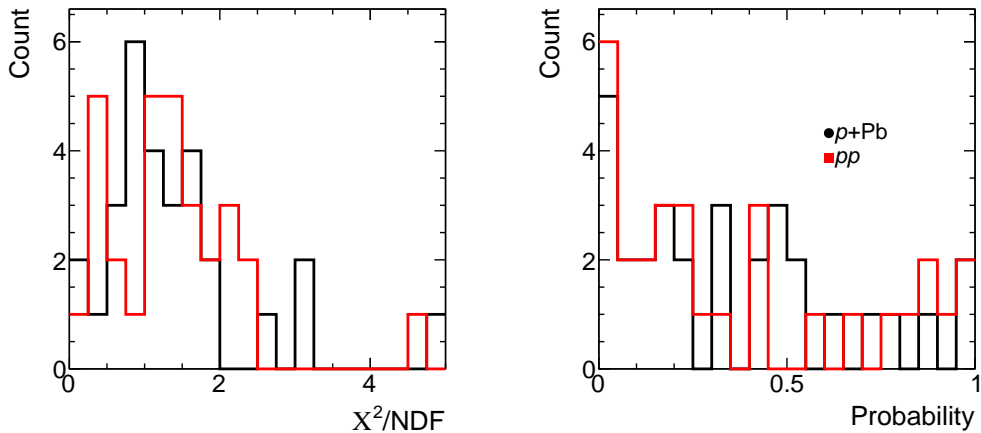


Figure 4.49: Comparison of fit quality of unfolded pp (red) and $p+Pb$ (black) results.

4.7.2 Widths and Conditional Yields With no Δp_T Requirement

The results of measurements of W_{12} in $p+Pb$ collisions and pp collisions for different ranges of $p_{T,1}$ and $p_{T,2}$ as a function of y_2^* are presented in left panels of Fig. 4.50. The W_{12} distribution increases with increasing rapidity separation between the leading and sub-leading jets both in the pp and $p+Pb$ collisions. Further, the W_{12} increases with imbalance in p_T between the leading and sub-leading jets. From the pQCD BFKL equation, the probability of additional soft radiation increases with larger rapidity separation between dijets, leading to a stronger $\Delta\phi$ decorrelation [91]. The results of the measurement of conditional yields I_{12} in $p+Pb$ and pp collisions are shown in the right panels of Fig. 4.50. The I_{12} distribution increases with the increasing rapidity separation between the two jets reaching a maximum for sub-leading jets in the $0 < y_2^* < 1.8$ interval and decreases for larger rapidity separations between the two jets. This is attributed to the dijet cross section falling off faster at forward rapidities compared to the inclusive jet cross section. The shapes of the I_{12} distributions for pp and $p+Pb$ collisions are similar for all $p_{T,1}$ and $p_{T,2}$ combinations.

The ratios ρ_W^{pPb} between $p+Pb$ collisions and pp collisions for different ranges of $p_{T,1}$ and $p_{T,2}$ as a function of y_2^* are consistent with unity and are presented in the left panel of Fig. 4.52. The ratios ρ_I^{pPb} between $p+Pb$ collisions and pp collisions in the same bins of rapidity and transverse momenta are shown in the right graph of Fig. 4.52. The uncertainty on both ρ_W^{pPb} and ρ_I^{pPb} is dominated by systematic uncertainties, which are correlated in jet p_T and y^* . The ratios ρ_I^{pPb} are consistent with unity for sub-leading jets in the lead-going direction. However, the ratio of conditional yields of jet pairs in the proton-going direction in $p+Pb$ collisions compared to pp collisions is suppressed by approximately 20%, with no significant dependence on jet p_T and rapidity of the sub-leading jet y_2^* . In the most forward-forward configuration, with both jets

in the lowest jet p_T interval $28 < p_{T,1}, p_{T,2} < 35$, the approximate x range probed is $1.5 \times 10^{-4} < x < 10^{-3}$. The suppression is an indication of possible nuclear effects including saturation.

4.7.3 Widths and Conditional Yields With a $\Delta p_T > 3$ GeV Requirement

Results for the W_{12} and the I_{12} distributions from $p+\text{Pb}$ collisions and pp collisions with a $\Delta p_T > 3$ GeV requirement are shown in Fig. 4.51. The C_{12} distributions are unaffected by the Δp_T cut, but the conditional yields I_{12} are smaller than the results with no Δp_T cut. This is expected because in bins of p_T with a width of 7 GeV to 10 GeV, a requirement that the leading and sub-leading jets have a $\Delta p_T > 3$ GeV will affect a significant portion of the statistics. Results for the ratios ρ_W^{pPb} and ρ_I^{pPb} with a $\Delta p_T > 3$ GeV requirement are shown in Fig. 4.51. The ratios ρ_W^{pPb} and ρ_I^{pPb} are both unaffected by the Δp_T cut indicating that having such a requirement does not have an impact on the study of possible saturation effects since both pp and $p+\text{Pb}$ collisions are identically affected.

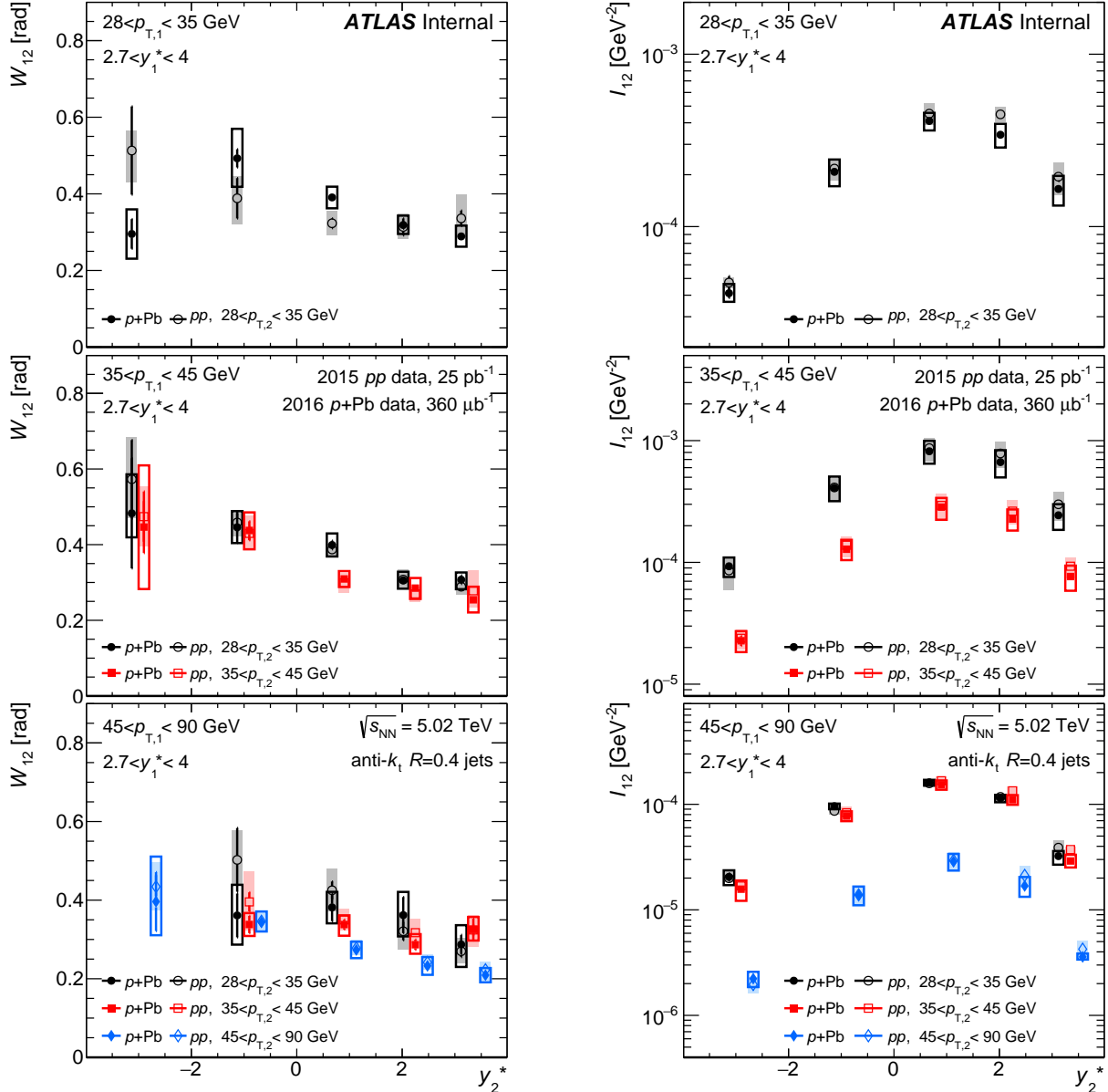


Figure 4.50: Comparison of W_{12} (left) and I_{12} (right) distributions in pp (open symbols) and $p+Pb$ (closed symbols) collisions for different selections of $p_{T,1}$ and $p_{T,2}$ as a function of y_2^* . The shaded and empty boxes indicate systematic uncertainties and vertical error bars represent statistical uncertainties. Results are presented with no Δp_T requirement.

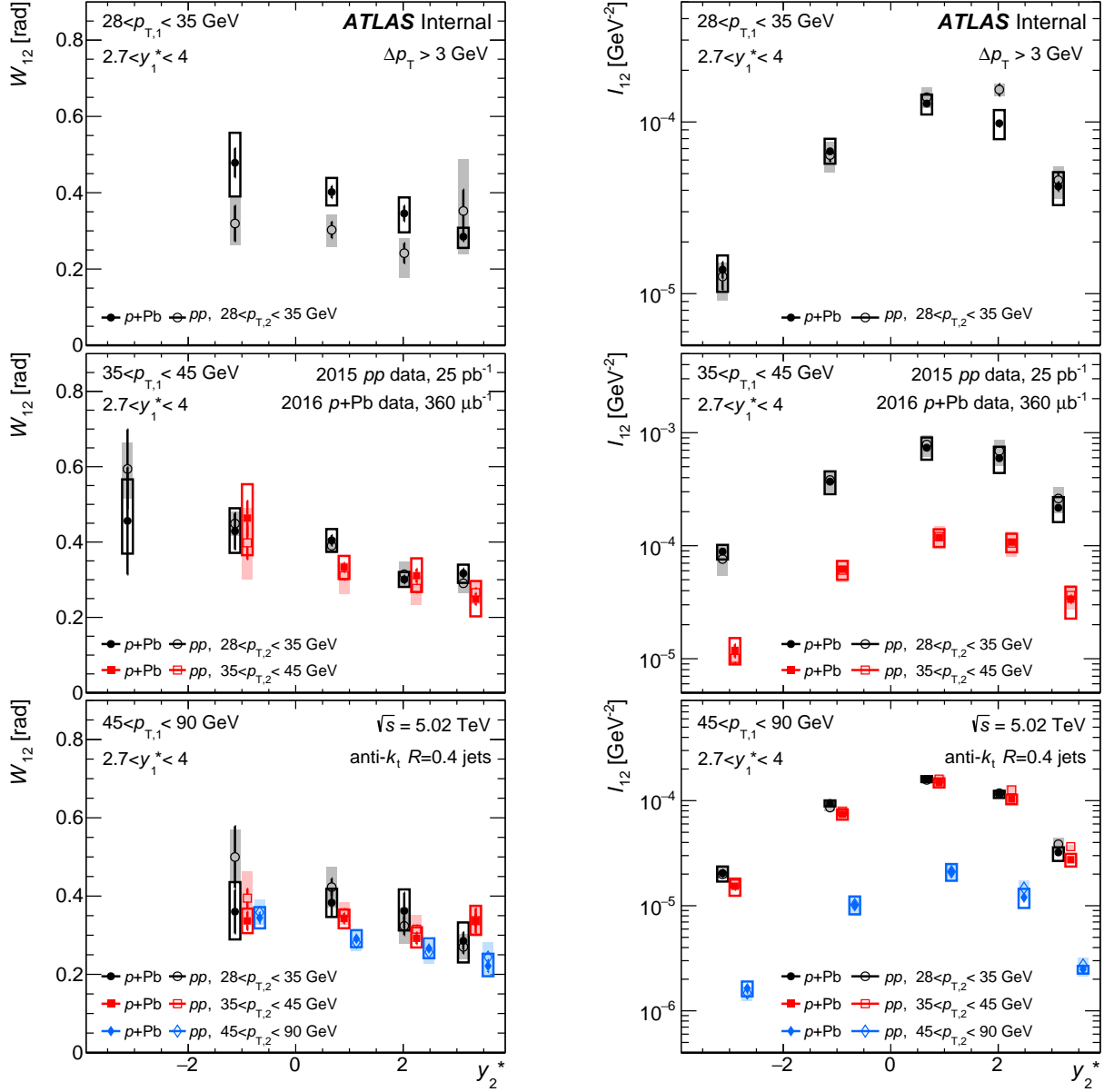


Figure 4.51: Comparison of W_{12} (left) and I_{12} (right) distributions in pp (open symbols) and $p+Pb$ (closed symbols) collisions for different selections of $p_{T,1}$ and $p_{T,2}$ as a function of y_2^* . The shaded and empty boxes indicate systematic uncertainties and vertical error bars represent statistical uncertainties. Some points have been removed due to high statistical uncertainties. Results are presented with a requirement of $\Delta p_T > 3$ GeV.

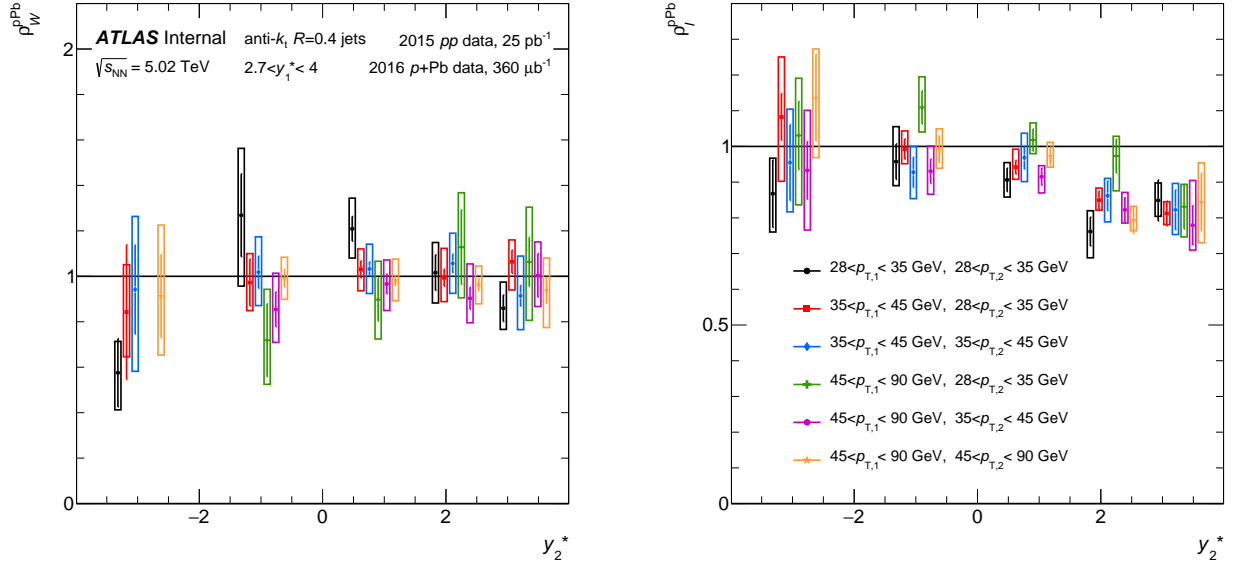


Figure 4.52: Ratios $\rho_W^{p\text{Pb}}$ of W_{12} (left) and $\rho_I^{p\text{Pb}}$ of I_{12} (right) between $p+\text{Pb}$ collisions and pp collisions for different selections of $p_{T,1}$ and $p_{T,2}$ as a function of y_2^* . The open boxes indicate systematic uncertainties and vertical error bars represent statistical uncertainties. Results are presented with no Δp_T requirement.

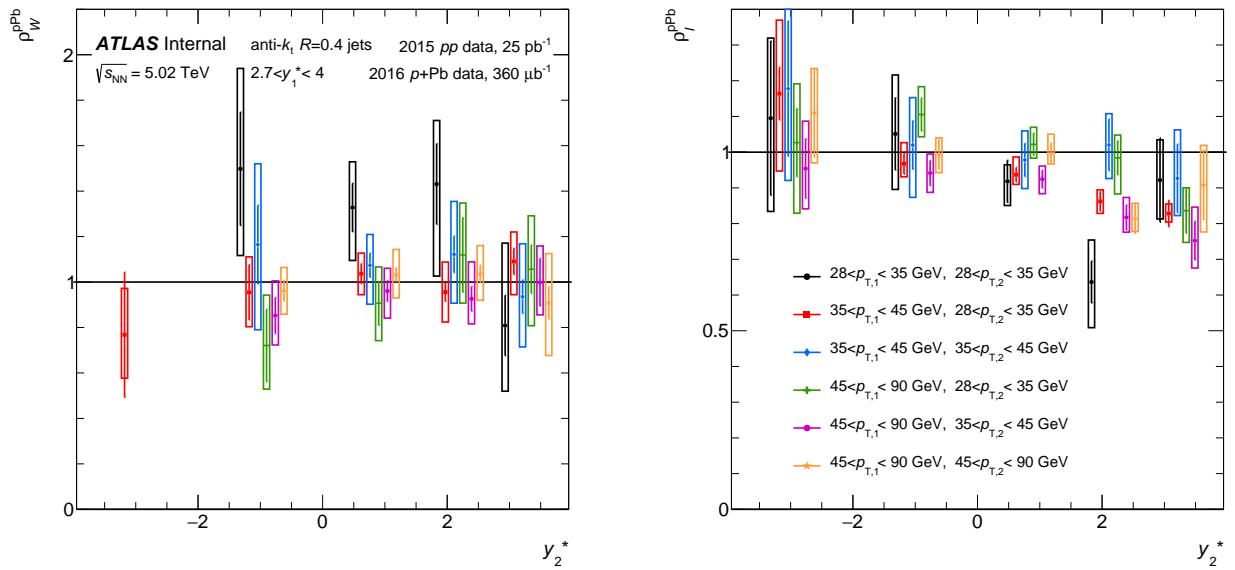


Figure 4.53: Ratios $\rho_W^{p\text{Pb}}$ of C_{12} (left) and $\rho_I^{p\text{Pb}}$ of I_{12} (right) between $p+\text{Pb}$ collisions and pp collisions for different selections of $p_{T,1}$ and $p_{T,2}$ as a function of y_2^* . The open boxes indicate systematic uncertainties and vertical error bars represent statistical uncertainties. Data points in the rapidity interval of $-4.0 < y_2^* < 1.8$ are not presented due to limited statistical precision. Results are presented with a requirement of $\Delta p_T > 3 \text{ GeV}$.

Chapter 5

Summary

This dissertation presents measurements of dijet azimuthal angular correlations along with their widths and the conditional yields of leading and sub-leading jets in $p+\text{Pb}$ collisions and pp collisions at $\sqrt{s} = 5.02 \text{ TeV}$. The measurement utilizes pairs of leading and sub-leading $R = 0.4$ anti- k_t jets in the transverse momentum range of $28 < p_T < 90 \text{ GeV}$. The shapes of azimuthal angular correlations, C_{12} for forward-forward and forward-central dijets and conditional yields could be sensitive to possible effects of gluon saturation at low- x [92, 93]. Dijets where both jets are very far forward probe $x \approx 10^{-5}$ at this collision energy.

The widths of the azimuthal correlations are found to be smaller for pairs of jets with higher $p_{T,1}, p_{T,2}$ and the widths increase with the increasing rapidity interval between the leading and sub-leading jet. No significant broadening of azimuthal angular correlations is observed for forward-forward and forward-central dijets in $p+\text{Pb}$ compared to pp collisions within the uncertainties. However, the measurement of conditional yields of jet-pairs for forward-forward jets in $p+\text{Pb}$ collisions compared to pp collisions shows a suppression of approximately 20%, with no significant dependence on jet p_T and y^* . The uncertainty on this ratio is dominated by systematic uncertainties, which are correlated in jet p_T and y^* . The observed suppression of ρ_I^{Pb} indicates possible saturation effects for the higher gluon densities expected in the Pb-nucleus at low- x .

Currently, there are no available calculations to compare these results to. However, the hope is that the presented measurement will contribute to predictions coming from phenomenology and theory groups interested in saturation physics. There has already been significant contact with groups working on such physics, and the motivation for tuning existing models to replicate the presented measurement exists. At the time of finishing this thesis, the results presented hereof were in the final steps of public approval by the ATLAS collaboration with the goal of being shown at the Hard Probes 2018 Conference in Aux-le-Bains, France. Furthermore, once approved, the results are planned to be published in the journal Physical Review C.

Appendix A

Data Sets

2016 $p+Pb$ Data Samples		Number of Events
data16_hip5TeV.00312649.physics_Main.recon.AOD.f784_m1741		8.96e6
data16_hip5TeV.00312796.physics_Main.recon.AOD.f784_m1741		4.32e7
data16_hip5TeV.00312837.physics_Main.recon.AOD.f774_m1736		8.50e7
data16_hip5TeV.00312937.physics_Main.recon.AOD.f774_m1736		2.60e7
data16_hip5TeV.00312945.physics_Main.recon.AOD.f774_m1736		2.87e7
data16_hip5TeV.00312968.physics_Main.recon.AOD.f774_m1736		3.66e7
data16_hip5TeV.00314199.physics_Main.recon.AOD.f781_m1741		2.40e8
2015 pp Data Samples		Number of Events
data15_5TeV.periodK.physics_Main.PhysCont.AOD.repro20_v03		1.15e8
data15_5TeV.periodVdM.physics_Main.PhysCont.AOD.repro20_v03		1.27e6

Table A.1: Data samples from $\sqrt{s_{NN}}=5.02$ TeV pp and $p+Pb$ collisions collected during the 2015 and 2016 heavy ion runs, respectively.

J	2015 pp PYTHIA8 MC Samples	Number of Events
1	mc15_5TeV.420011.Pythia8EvtGen_A14NNPDF23L0_jetjet_JZ1R04.merge.AOD.e4108_s2860_r7792_r7676	5.88e6
2	mc15_5TeV.420012.Pythia8EvtGen_A14NNPDF23L0_jetjet_JZ2R04.merge.AOD.e4108_s2860_r7792_r7676	5.84e6
2016 $p+Pb$ PYTHIA8 MC Samples		Number of Events
1	mc15_5TeV.420018.Pythia8EvtGen_A14NNPDF23L0_jetjet_JZ1R04_MaxEta_m3p0.merge.AOD.e6114_d1462_r10136_r9647	1.98e6
2	mc15_5TeV.420019.Pythia8EvtGen_A14NNPDF23L0_jetjet_JZ2R04_MaxEta_m3p0.merge.AOD.e6114_d1462_r10136_r9647	1.00e6
J	2015 pp HERWIG++ MC Samples	Number of Events
1	mc15_5TeV.420031.HerwigppEvtGen_UEEE5_CTEQ6L1_jetjet_JZ1R04.merge.AOD.e4929_s2860_r7792_r7676	2.82e6
2	mc15_5TeV.420032.HerwigppEvtGen_UEEE5_CTEQ6L1_jetjet_JZ2R04.merge.AOD.e4929_s2860_r7792_r7676	2.80e6

Table A.2: 2015 pp PYTHIA8 MC Samples (top). 2016 $p+Pb$ PYTHIA8 MC samples with data overlay (middle). 2015 pp HERWIG++ Monte Carlo samples (bottom).

Appendix B

Bin-by-bin Unfolding Procedure.

In Figure B.1, we have truth and reconstructed $\Delta\phi$ distributions on the left-most plot, the response matrix M_{ij} where $\Delta\phi_{Reco}$ is along the x-axis, along the j-index, and $\Delta\phi_{Truth}$ is along the y-axis, along the i-index, and resulting correction factors with errors on the right-most.

Define T_i as the total number of entries in the i^{th} bin of the Truth distribution (blue points on left plot), and R_i as the total number of entries in the i^{th} bin of the Reconstructed distribution (red points on left plot).

In terms of the response matrix, R_j is

$$R_j = \sum_i M_{ij} = M_{jj} + \sum_{i \neq j} M_{ij} \quad (\text{B.1})$$

The last part is just the diagonal element plus the off-diagonal vertical elements of the i^{th} bin (on the x-axis).

Similarly, in terms of the response matrix, T_i is

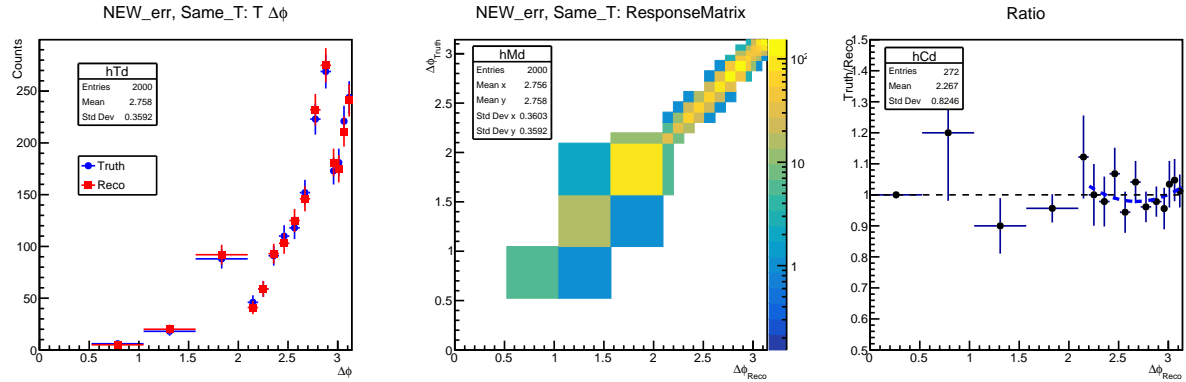


Figure B.1: $\Delta\phi$ distributions for truth and reco (left). Response Matrix M_{ij} (center). Correction factors with errors (right).

$$T_i = \sum_j M_{ij} = M_{ii} + \sum_{j \neq i} M_{ij} \quad (\text{B.2})$$

For some bin i^{th} reconstructed bin,

$$R_i = T_i - N_{Leaving} + N_{Arriving} = T_i - \sum_{k \neq i} M_{ik} + \sum_{j \neq i} M_{ji} \quad (\text{B.3})$$

We can express the number leaving and number arriving in terms of off-diagonal row or column elements of M_{ij} , or in terms of T_i , R_i , and diagonal elements of M_{ij} .

$$N_{Leaving} = T_i - M_{ii} \quad (\text{B.4})$$

$$N_{Arriving} = R_i - M_{ii} \quad (\text{B.5})$$

Now, T_i is taken as a constant. This means that reconstructed distribution can be different time to time, but the truth distribution stays the same. In the language of a toy MC, this is equivalent to generating one Truth distribution, and smearing it many different times, each time (or for each new "experiment") getting new results.

When T_i is taken as constant, the bin migration of leaving and arriving is different. The distribution of $N_{Leaving}$ is binomial, while $N_{Arriving}$ is Poisson. If T_i is fixed, there is only a certain number of entries that can leave, while the number that arrives depends on, and is a mix of the entries leaving neighboring bins.

In a toy MC ¹, for the case where the truth distribution was generated one time, but smearing applied to the reconstructed (case with "fixed" T_i), it is clear from Figure B.2 that the migration where entries are leaving is narrower than where they arrive. In the same toy MC, when for every experiment a new truth distribution was used, it is evident that the migration to and from is the same.

Correction factors C_i , which relate T_i and R_i are

$$C_i = \frac{T_i}{R_i} \quad (\text{B.6})$$

¹A Toy MC with a randomly generated exponential was generated for the truth distribution 5000 times, with smearing from the ATLAS MC response matrix applied to the reconstructed distribution. The experiment was then repeated 10,000 times to get some good statistics on correction factors, their errors, bin migration, etc.

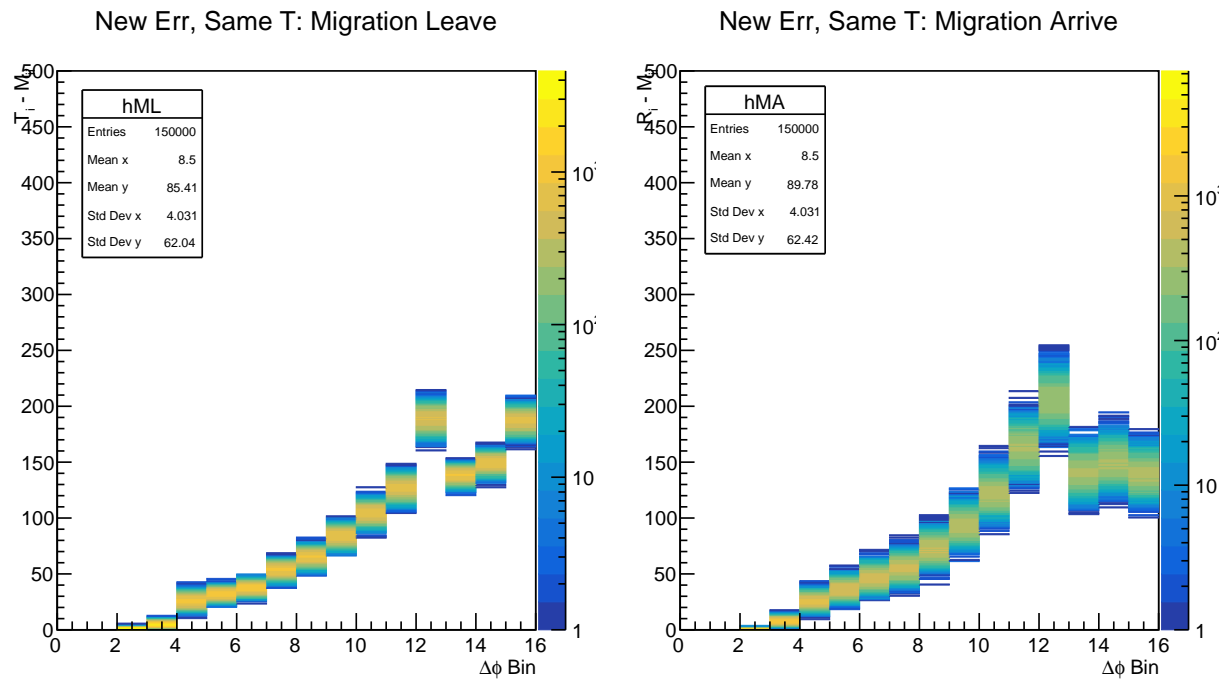


Figure B.2: For the case where for every experiment a the same generated truth distribution but differently smeared reconstructed distribution, histogram of migration between $\Delta\phi$ bins (x and y axes) for entries arriving (right) and entries leaving (left). Migration where entries leave has a binomial (narrower) distribution, while entries arriving is Poisson.

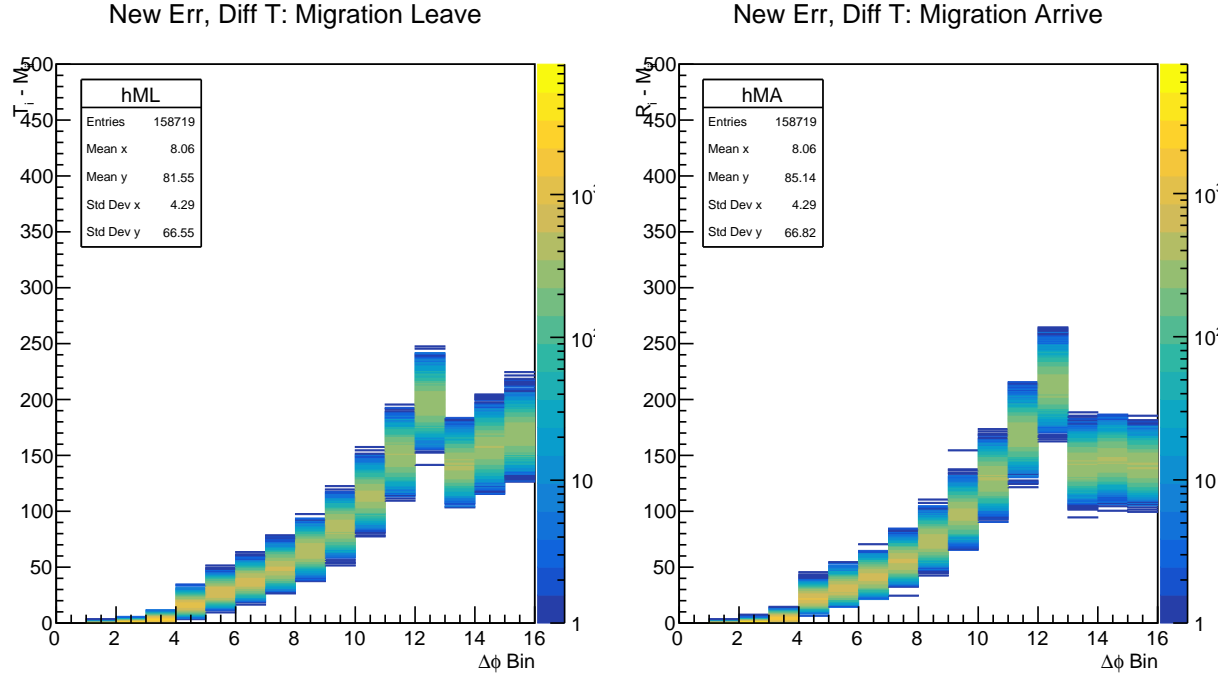


Figure B.3: For the case where for every experiment a new truth distribution is generated and the reconstructed is smeared from that, histogram of migration between $\Delta\phi$ bins (x and y axes) for entries arriving (right) and entries leaving (left). Both migrations have Poisson distributions.

and their respective errors σ_{C_i} are

$$\sigma_{C_i}^2 = \frac{C_i^2}{R_i^2} \sigma_{R_i}^2 \quad (\text{B.7})$$

Now since T_i is constant, and the entries leaving a T_i bin follow binomial statistics, while entries arriving are Poisson, we continue from Equation B.3. The error in R_i is

$$\sigma_{R_i}^2 = \sigma_{N_{Leave}}^2 + \sigma_{N_{Arrive}}^2 \quad (\text{B.8})$$

$$\sigma_{R_i}^2 = T_i \frac{T_i - M_{ii}}{T_i} \left(1 - \frac{T_i - M_{ii}}{T_i}\right) + (R_i - M_{ii}) \quad (\text{B.9})$$

$$\sigma_{R_i}^2 = T_i + R_i - 2M_{ii} - \frac{(T_i - M_{ii})^2}{T_i} \quad (\text{B.10})$$

From this, plugging into Equation B.7, the error on the correction factor is

$$\sigma_{C_i}^2 = \frac{T_i^2}{R_i^4} \left(T_i + R_i - 2M_{ii} - \frac{(T_i - M_{ii})^2}{T_i} \right) \quad (\text{B.11})$$

$$\sigma_{C_i}^2 = \frac{T_i^2}{R_i^3} \left(1 - \frac{M_{ii}^2}{T_i R_i} \right). \quad (\text{B.12})$$

Appendix C

$\Delta\phi$ Correction Factors From pp MC Samples

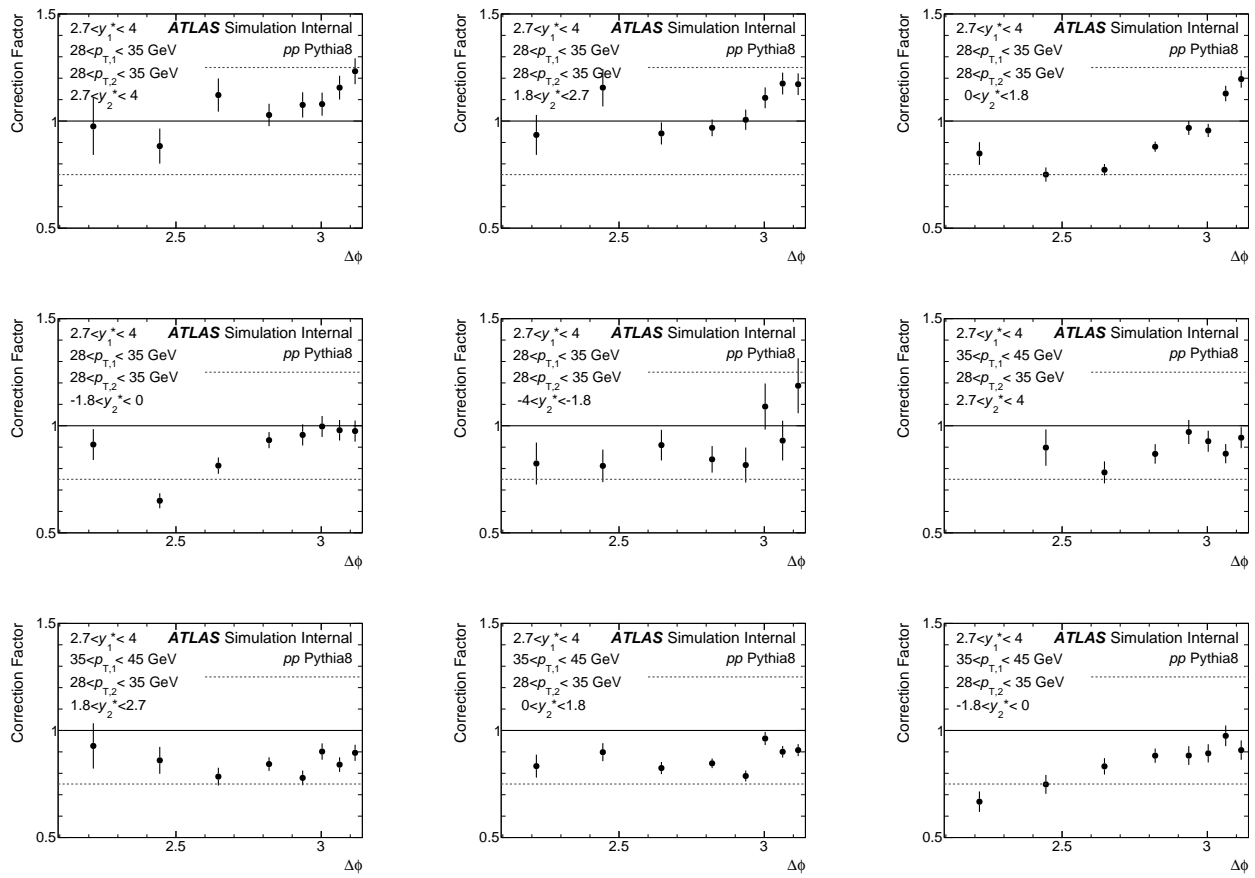


Figure C.1: Correction factors derived from pp MC samples.

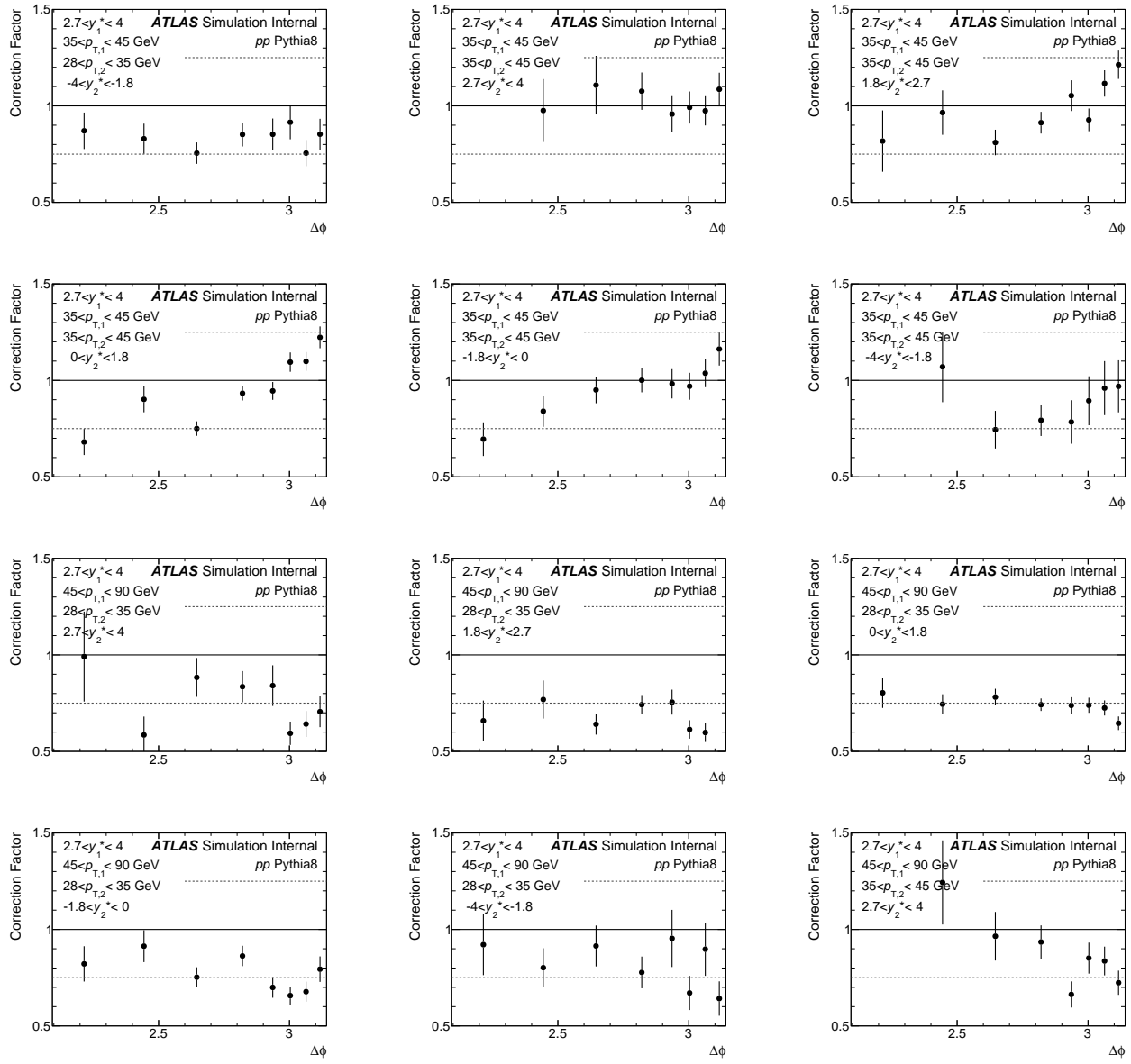


Figure C.2: Correction factors derived from pp MC samples.

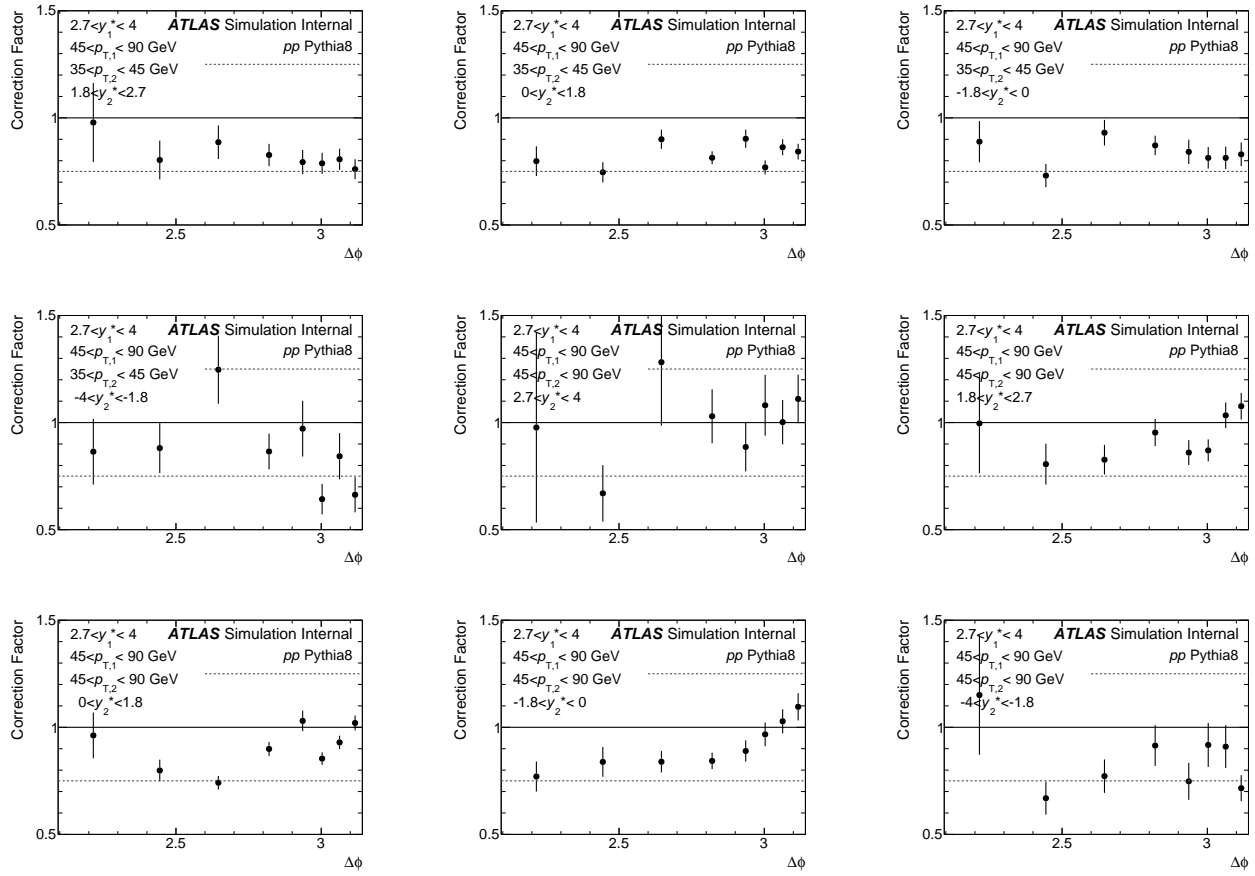


Figure C.3: Correction factors derived from pp MC samples.

Appendix D

$\Delta\phi$ Correction Factors From $p+\text{Pb}$ MC Samples

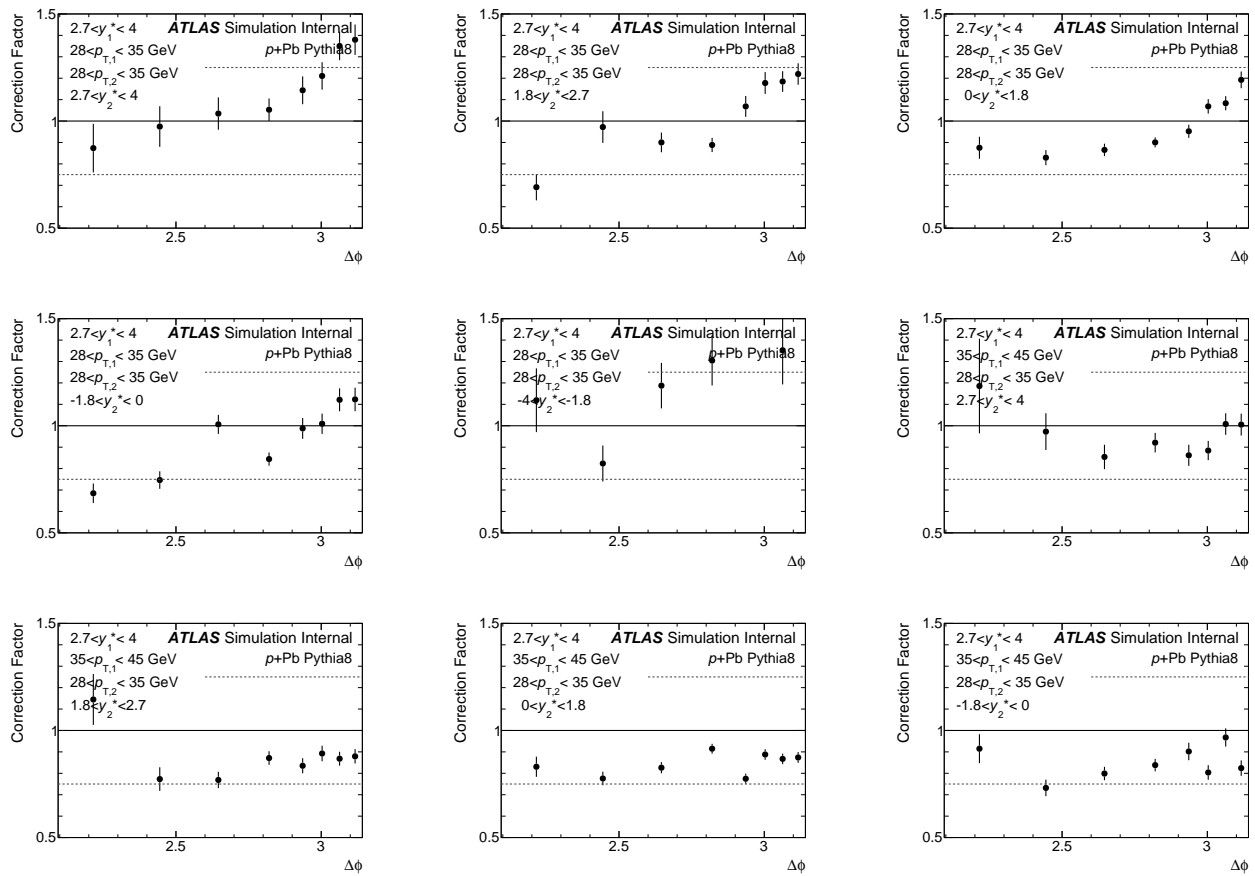


Figure D.1: Correction factors derived from $p+\text{Pb}$ MC samples.

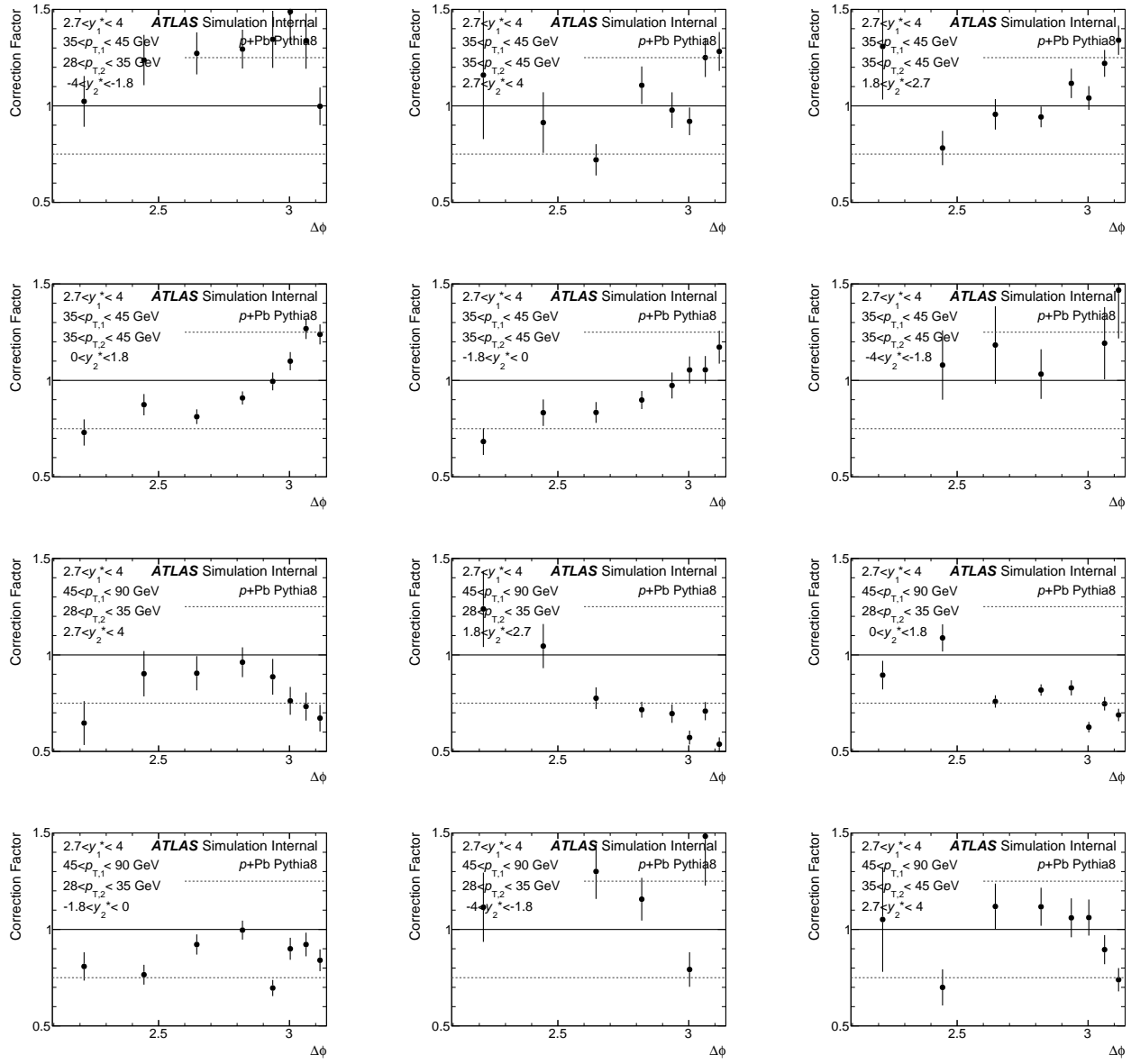


Figure D.2: Corretion factors derived from $p+Pb$ MC samples.

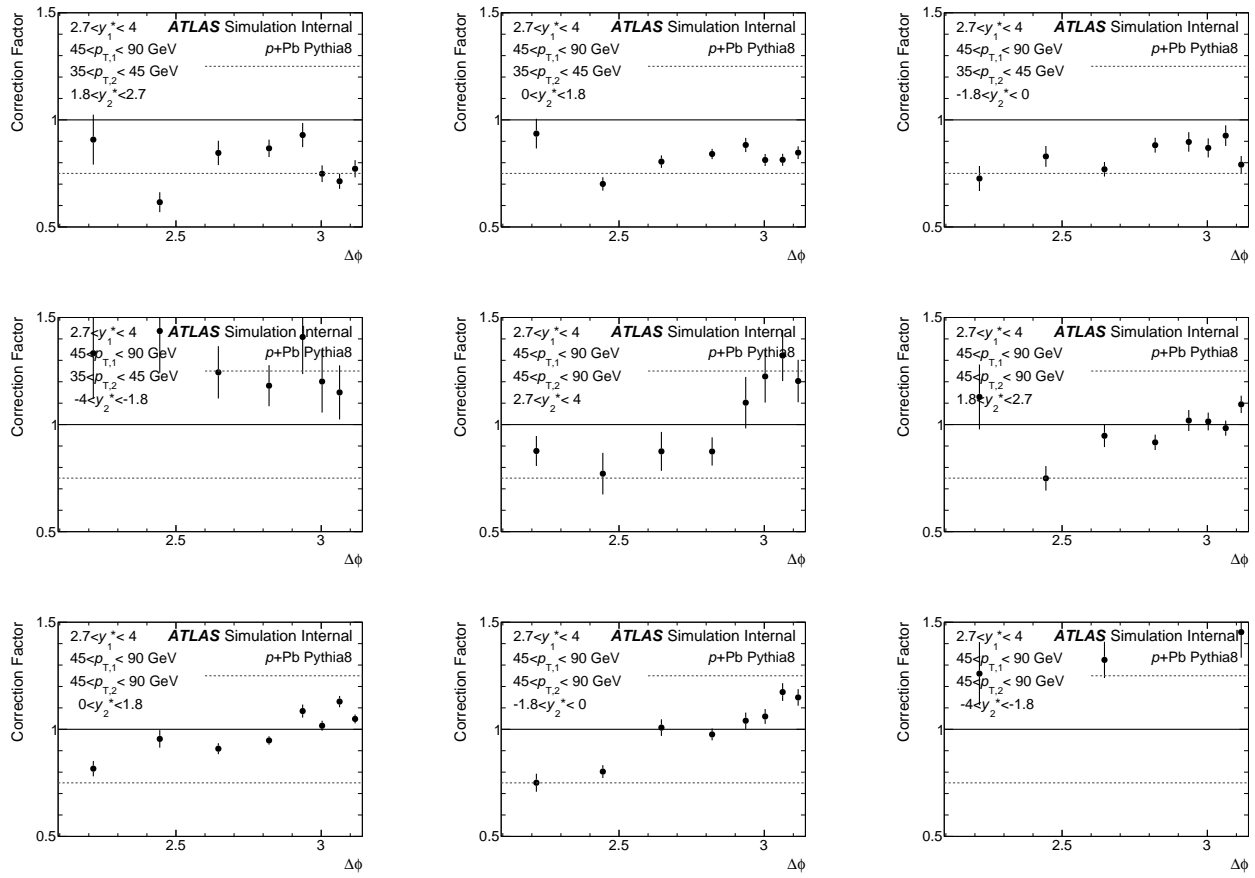


Figure D.3: Corretion factors derived from $p+Pb$ MC samples.

Appendix E

Appendix: Effect of Isolation Cuts

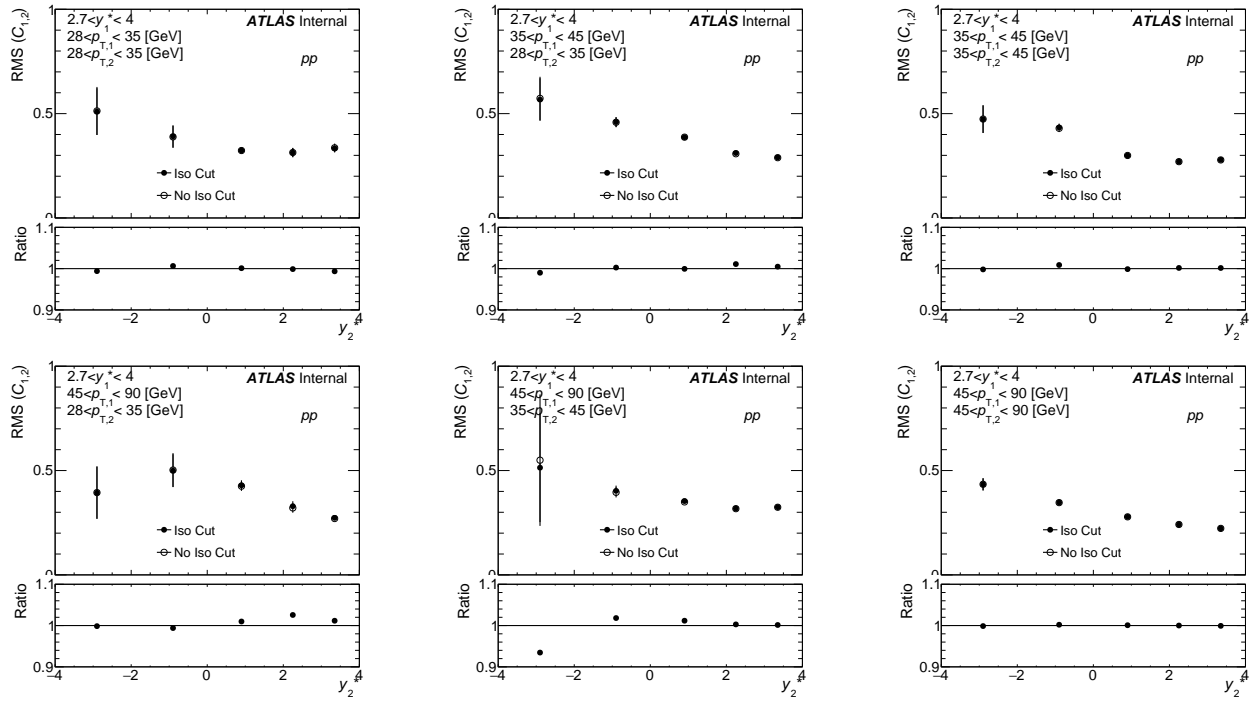


Figure E.1: Comparison of C_{12} distributions with and without isolation requirement in pp data.

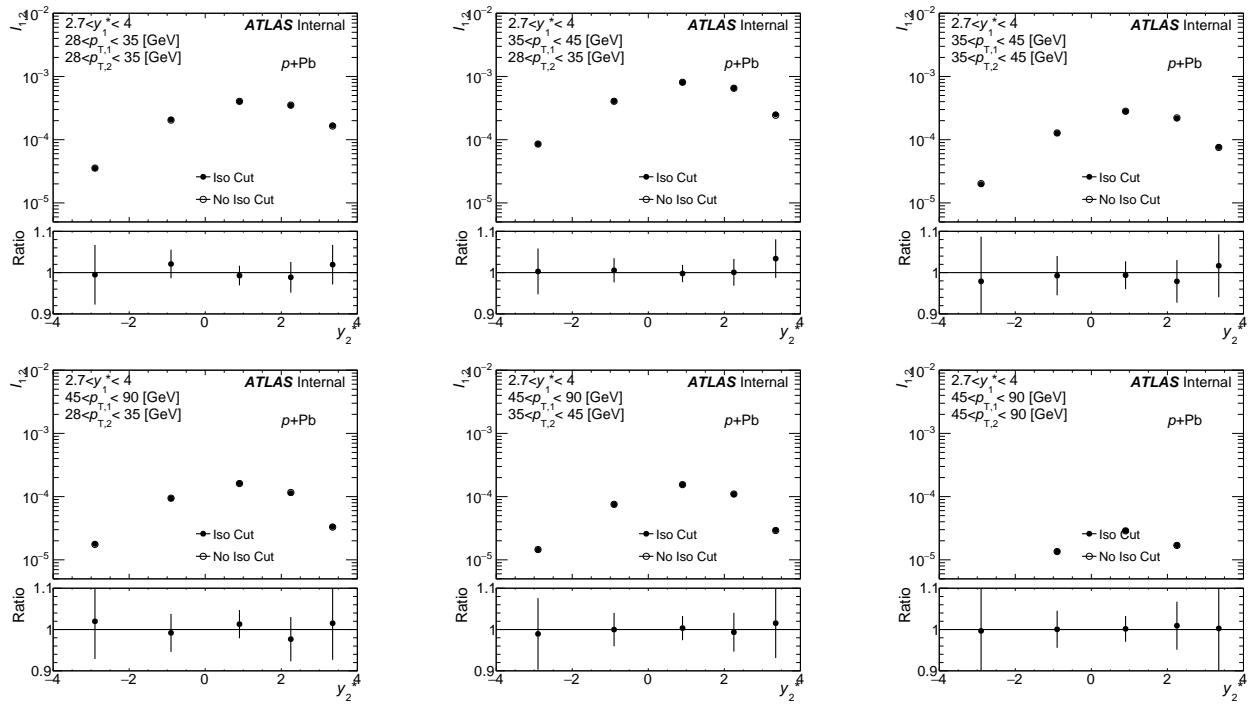


Figure E.2: Comparison of I_{12} distributions with and without isolation requirement in $p+Pb$ data.

Appendix F

Effect of New JES Systematic Uncertainties

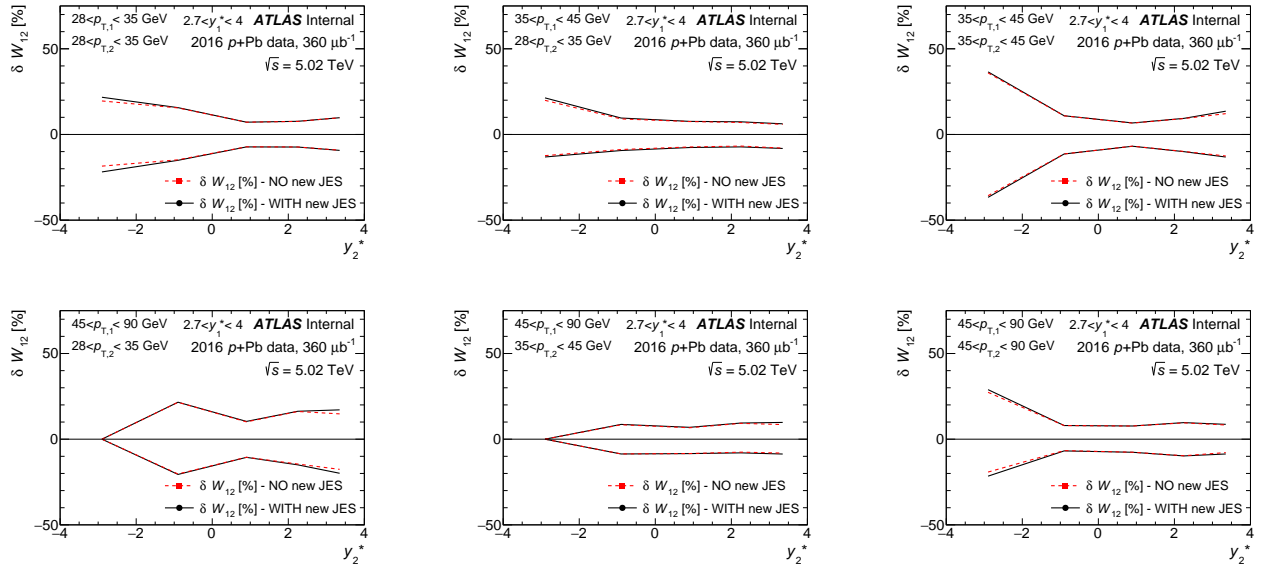


Figure F.1: Effect on total systematic uncertainty on C_{12} after adding new JES uncertainties. Generally the effect is below 10%.

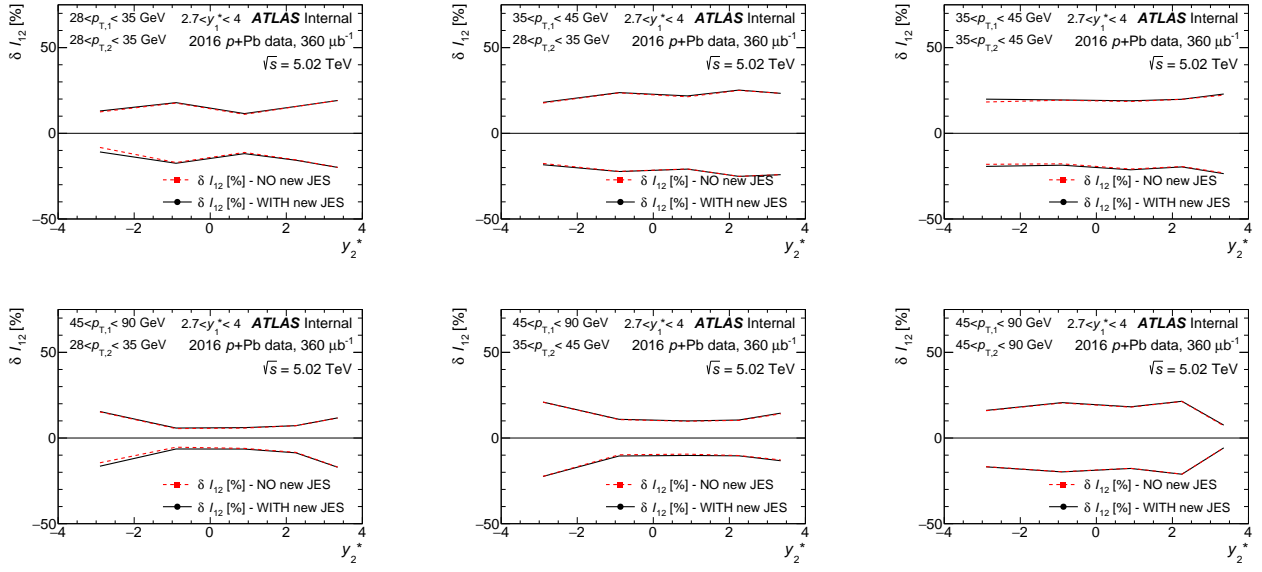


Figure F.2: Effect on total systematic uncertainty on I_{12} after adding new JES uncertainties. Generally the effect is below 10%, with some bins reaching 25%.

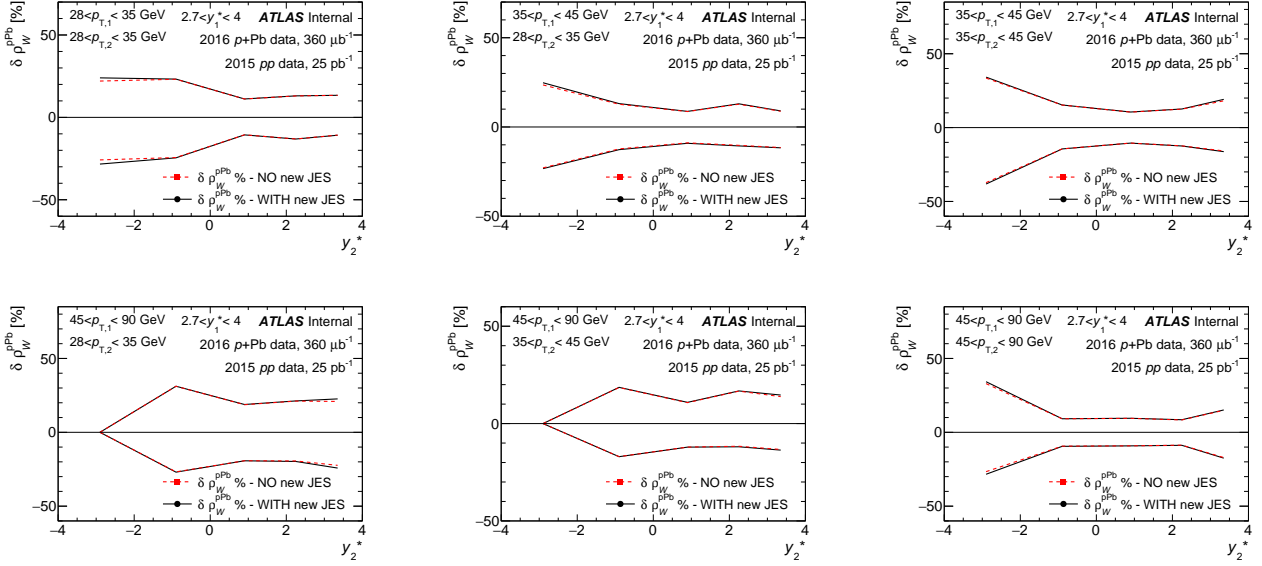


Figure F.3: Effect on total systematic uncertainty on ratio ρ_W^{pPb} after adding new JES uncertainties. The total systematic uncertainty on ρ_W^{pPb} before the addition of the new JES uncertainties is shown as the dotted red line, after the addition of the new JES uncertainties in the solid black line. Generally the absolute difference is below 2%.

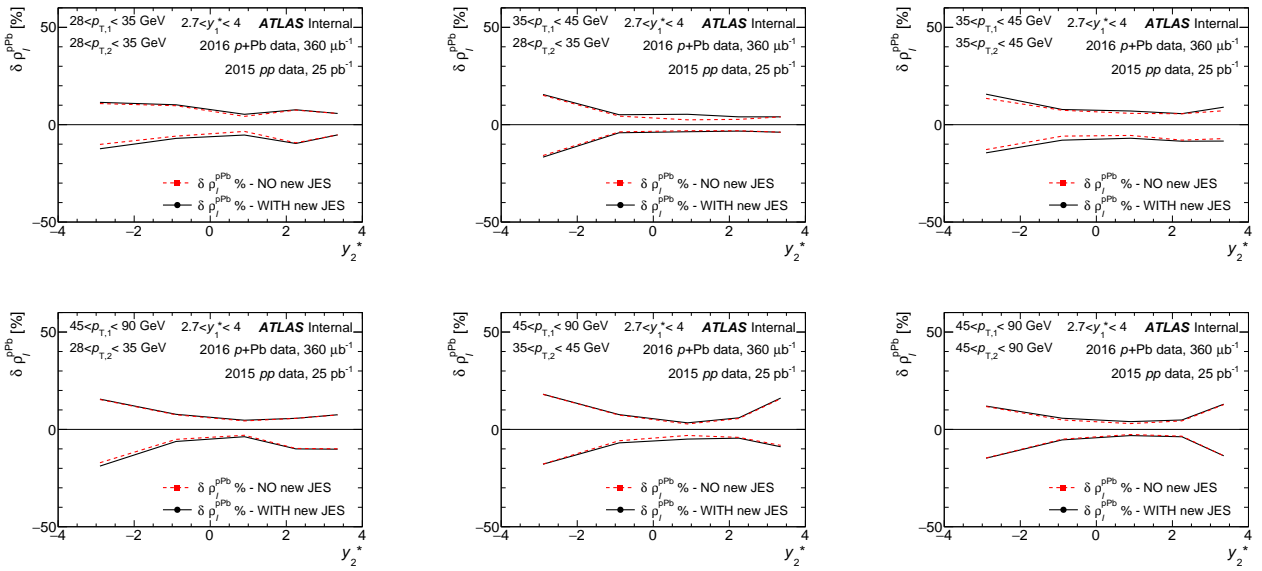


Figure F.4: Effect on total systematic uncertainty on ratio $\rho_I^{p\text{Pb}}$ after adding new JES uncertainties. The total systematic uncertainty on $\rho_I^{p\text{Pb}}$ before the addition of the new JES uncertainties is shown as the dotted red line, after the addition of the new JES uncertainties in the solid black line. Generally the absolute difference is below 2%, with a one bin in the most negative y_2^* region having an effect of 5%.

Appendix G

Fitting Systematic Uncertainties

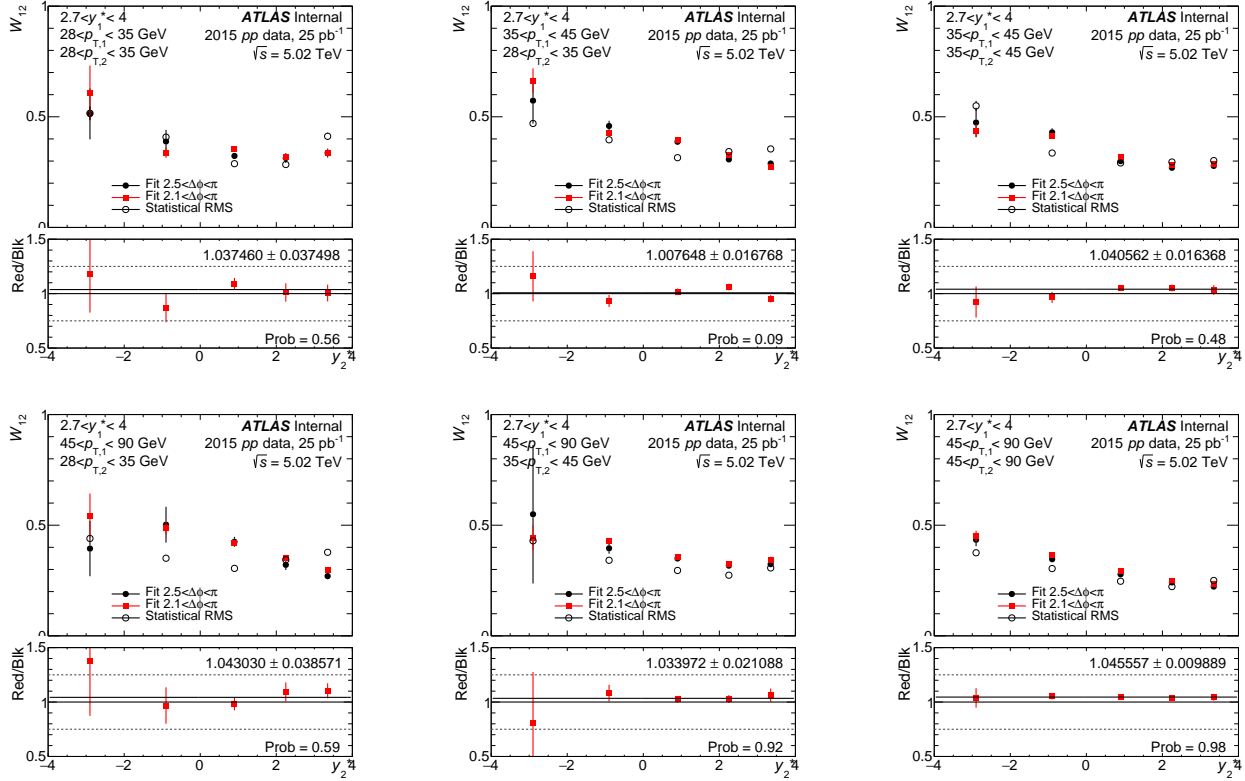


Figure G.1: For pp data, comparison of fits in default range (black) and extended range (red) and their ratios, which represent the systematic uncertainty on the fits. Due to large statistical fluctuations in some points, the ratios are fitted to a constant. Empty black points show result of statistical RMS calculation.

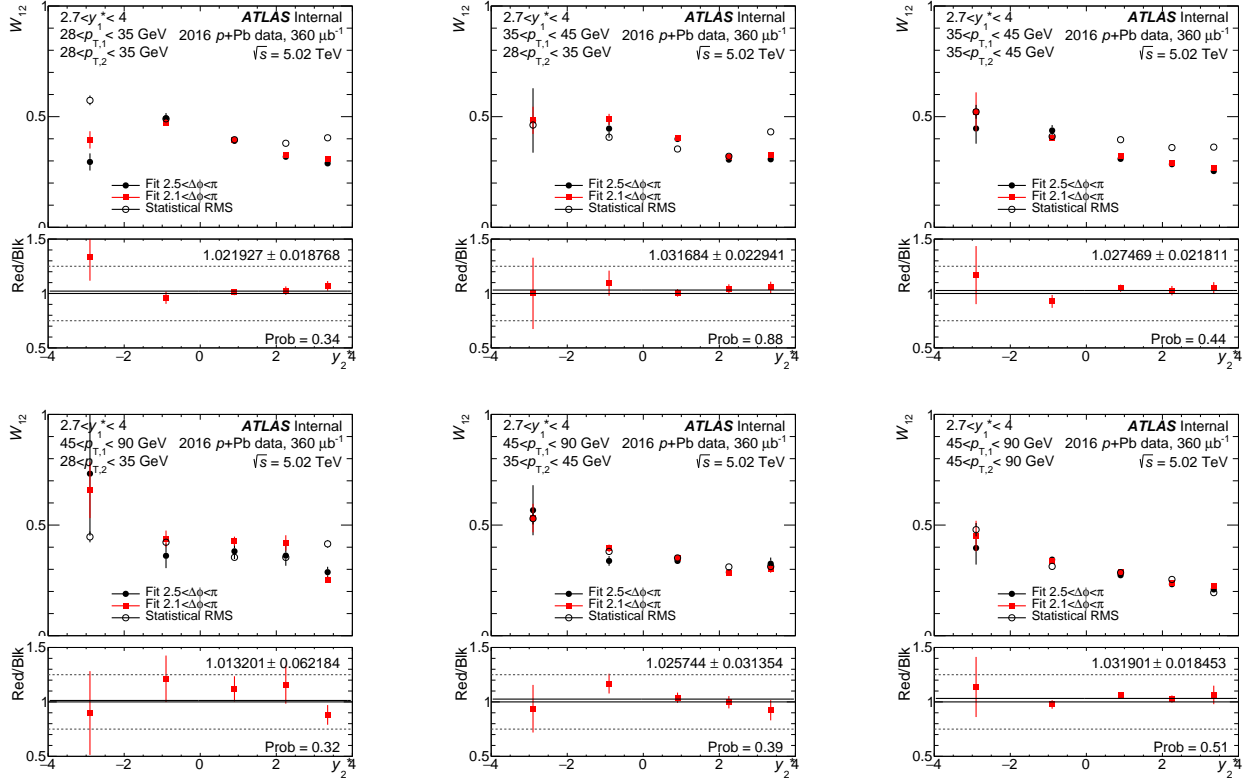


Figure G.2: For $p+\text{Pb}$ data, comparison of fits in default range (black) and extended range (red) and their ratios, which represent the systematic uncertainty on the fits. Due to large statistical fluctuations in some points, the ratios are fitted to a constant. Empty black points show result of statistical RMS calculation.

Appendix H

Unfolded C_{12} Distributions from Data with Systematic Uncertainties

H.1 C_{12} distributions with no Δp_T requirement

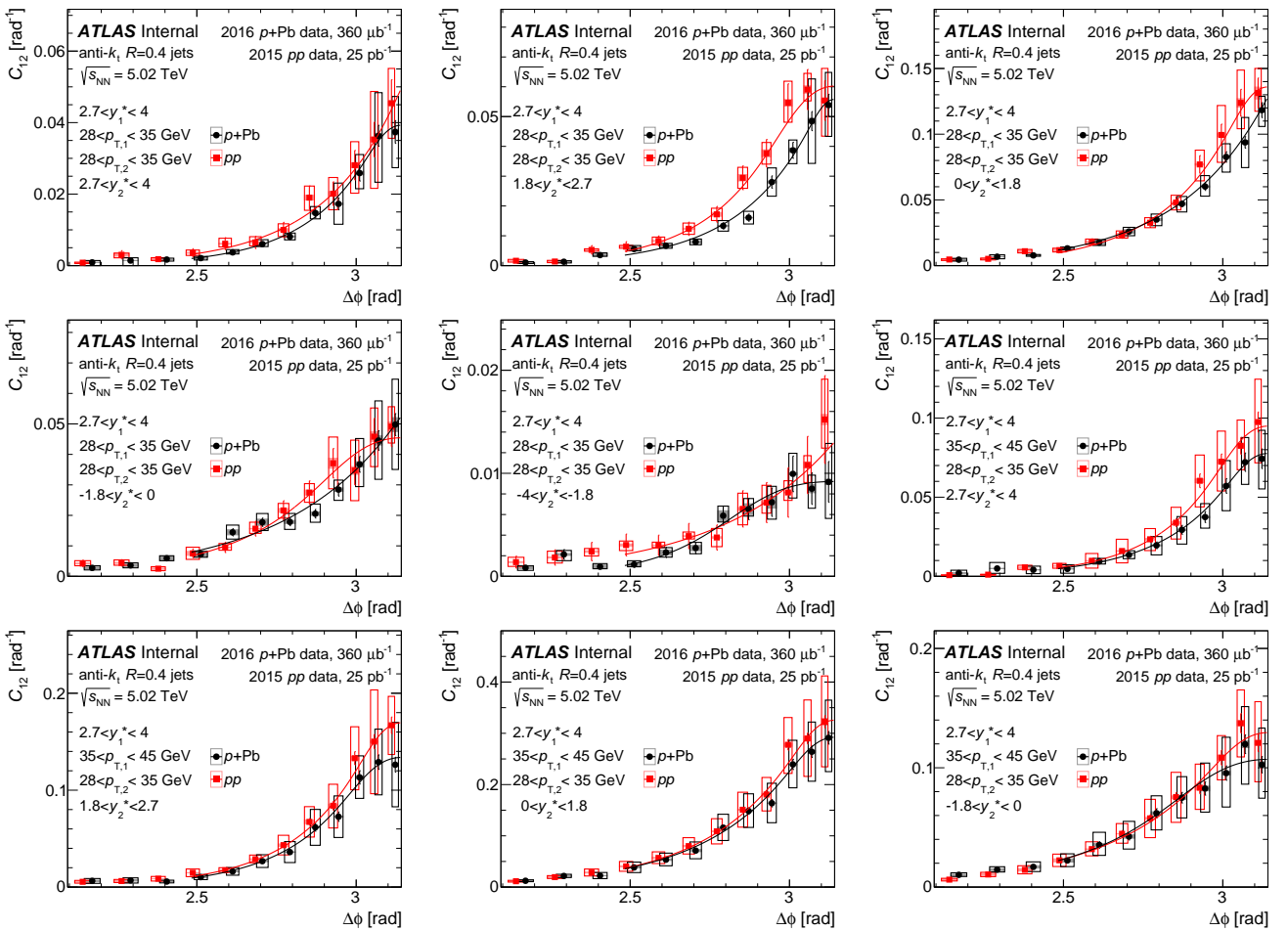


Figure H.1: Unfolded C_{12} distributions in pp (red symbols) and $p+\text{Pb}$ (black symbols) collisions for different selections of $p_{T,1}$, $p_{T,2}$, and y_2^* as a function of $\Delta\phi$. Lines represent results of the fit (for more details see the text). Open boxes represent correlated systematic uncertainties and vertical error bars represent statistical uncertainties. Results are shown with no Δp_T requirement.

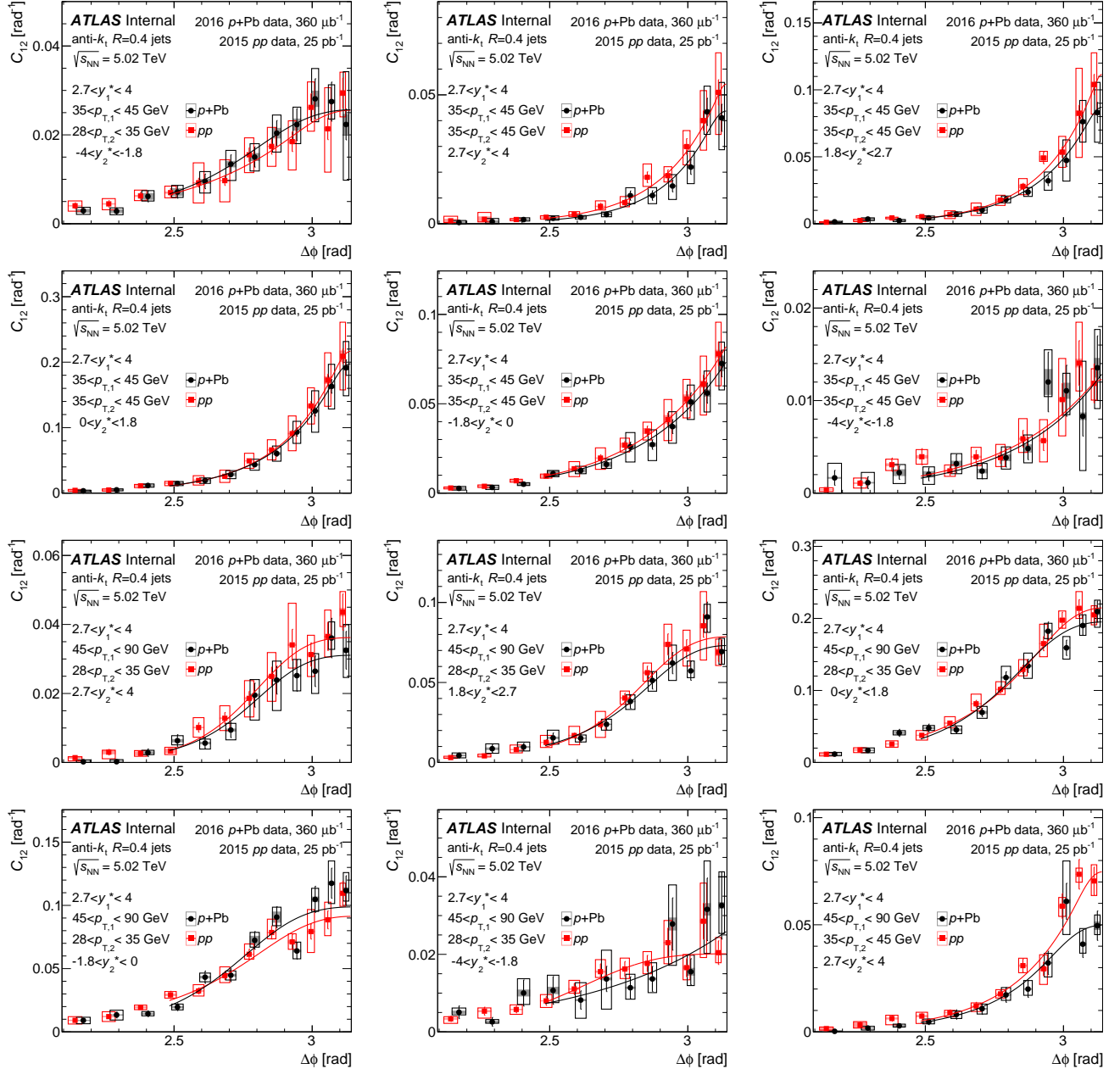


Figure H.2: Unfolded C_{12} distributions in pp (red symbols) and $p+Pb$ (black symbols) collisions for different selections of $p_{T,1}$, $p_{T,2}$, and y_2^* as a function of $\Delta\phi$. Lines represent results of the fit (for more details see the text). Open boxes represent correlated systematic uncertainties and vertical error bars represent statistical uncertainties. Results are shown with no Δp_T requirement.

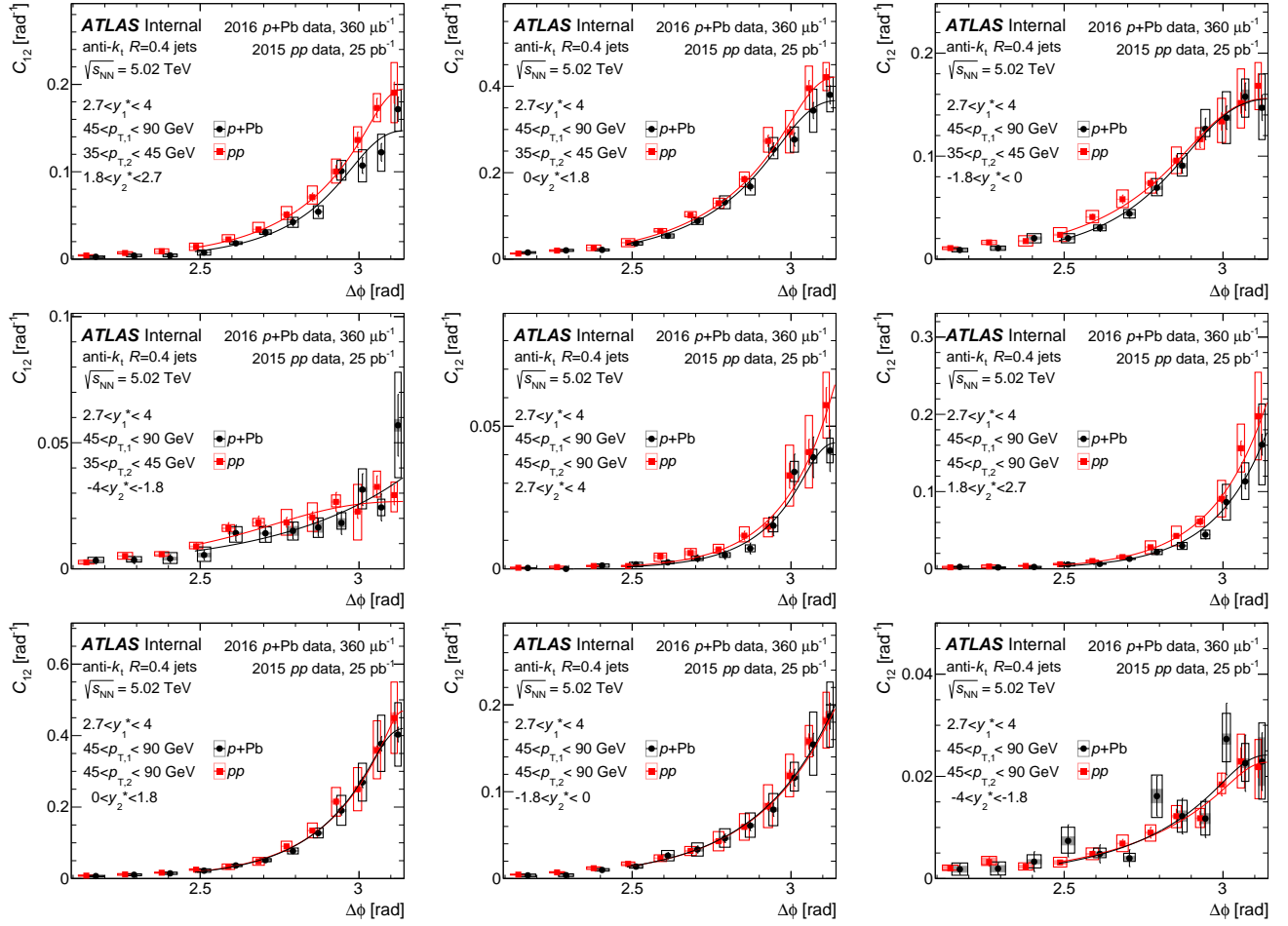


Figure H.3: Unfolded C_{12} distributions in pp (red symbols) and $p+Pb$ (black symbols) collisions for different selections of $p_{T,1}$, $p_{T,2}$, and y_2^* as a function of $\Delta\phi$. Lines represent results of the fit (for more details see the text). Open boxes represent correlated systematic uncertainties and vertical error bars represent statistical uncertainties. Results are shown with no Δp_T requirement.

H.2 C_{12} distributions with a requirement of $\Delta p_T > 3$ GeV

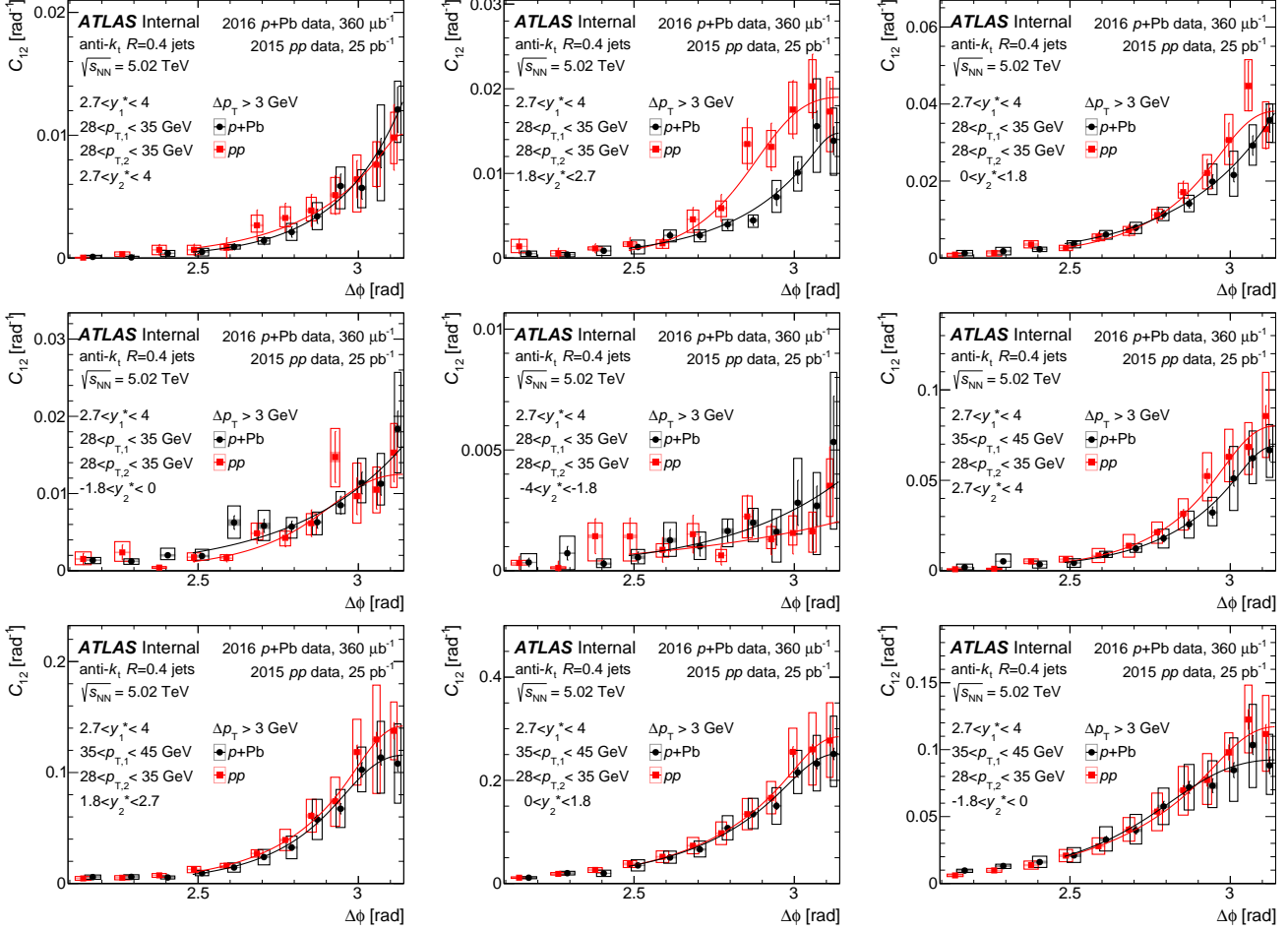


Figure H.4: Unfolded C_{12} distributions in pp (red symbols) and $p+\text{Pb}$ (black symbols) collisions for different selections of $p_{T,1}$, $p_{T,2}$, and y_2^* as a function of $\Delta\phi$. Lines represent results of the fit (for more details see the text). Open boxes represent correlated systematic uncertainties and vertical error bars represent statistical uncertainties. Results are presented with a requirement of $\Delta p_T > 3$ GeV.

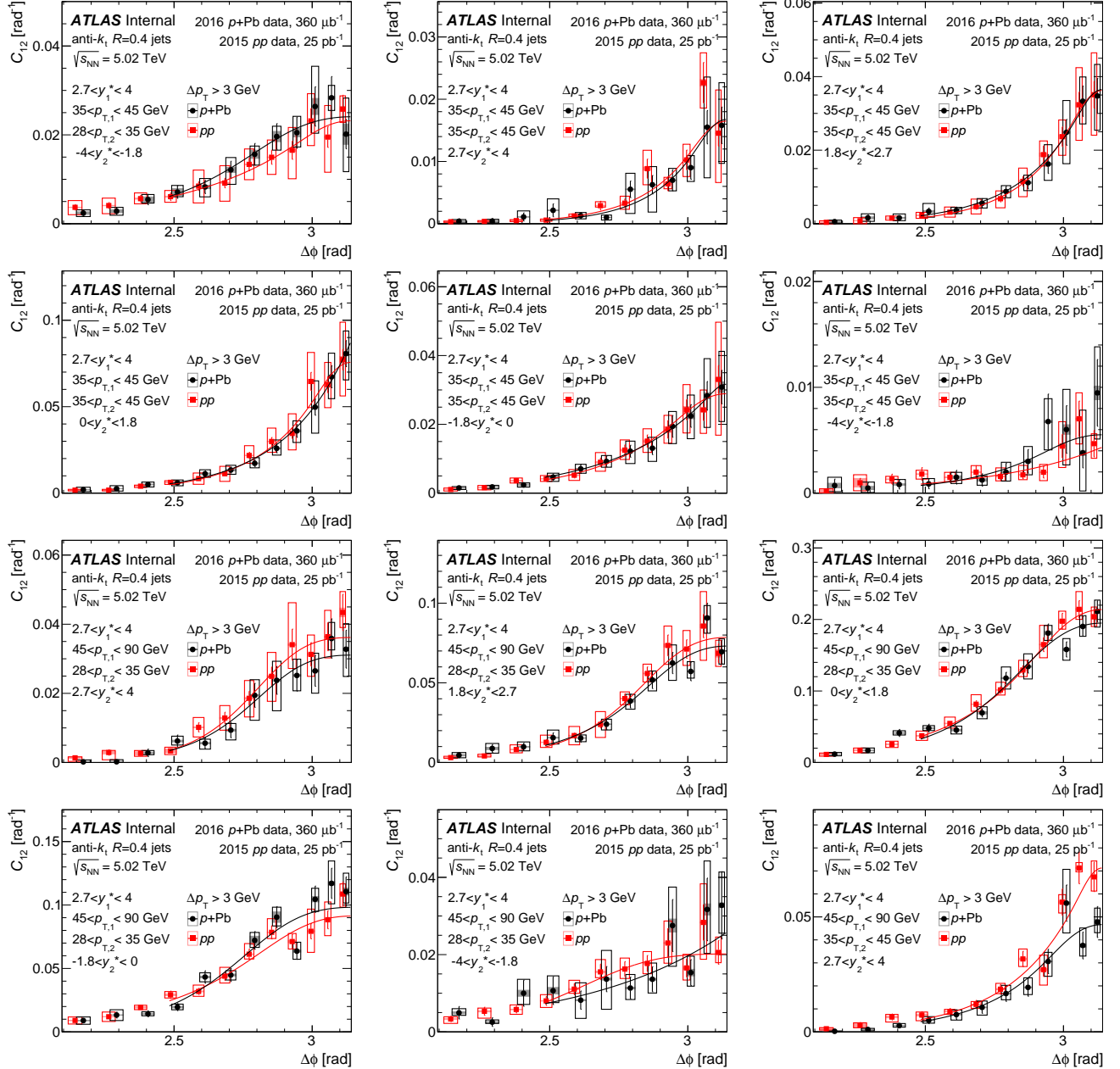


Figure H.5: Unfolded C_{12} distributions in pp (red symbols) and $p+Pb$ (black symbols) collisions for different selections of $p_{T,1}$, $p_{T,2}$, and y_2^* as a function of $\Delta\phi$. Lines represent results of the fit (for more details see the text). Open boxes represent correlated systematic uncertainties and vertical error bars represent statistical uncertainties. Results are presented with a requirement of $\Delta p_T > 3$ GeV.

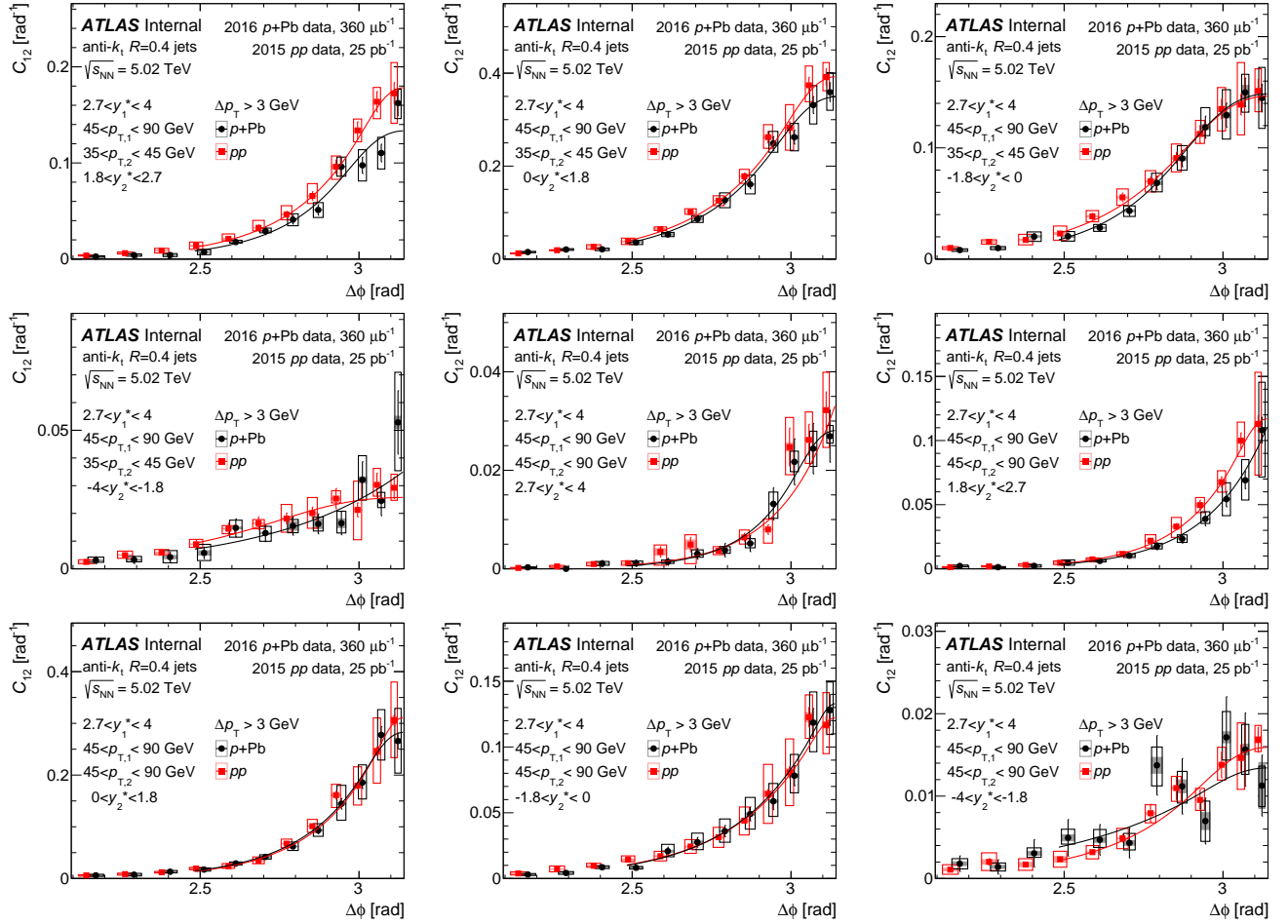


Figure H.6: Unfolded C_{12} distributions in pp (red symbols) and $p+Pb$ (black symbols) collisions for different selections of $p_{T,1}$, $p_{T,2}$, and y_2^* as a function of $\Delta\phi$. Lines represent results of the fit (for more details see the text). Open boxes represent correlated systematic uncertainties and vertical error bars represent statistical uncertainties. Results are presented with a requirement of $\Delta p_T > 3$ GeV.

References

- [1] NMC Collaboration. “LHC Machine”. In: *JINST* 3 (2008), S08001. DOI: [10.1088/1748-0221/3/08/S08001](https://doi.org/10.1088/1748-0221/3/08/S08001).
- [2] CERN. *TE-EPC-LPC*. 2016. URL: <http://te-epc-lpc.web.cern.ch/te-epc-lpc/machines/lhc/general.stm> (visited on 10/26/2016).
- [3] ATLAS Collaboration. “The ATLAS Experiment at the CERN Large Hadron Collider”. In: *JINST* 3 (2008), S08003. DOI: [10.1088/1748-0221/3/08/S08003](https://doi.org/10.1088/1748-0221/3/08/S08003).
- [4] J Bremer. “The Cryogenic System for the ATLAS Liquid Argon Detector”. In: LHC-Project-Report-393. CERN-LHC-Project-Report-393 (June 2000), 5 p. URL: <https://cds.cern.ch/record/449276>.
- [5] C. W. Fabjan and F. Gianotti. “Calorimetry for particle physics”. In: *Rev. Mod. Phys.* 75 (2003), pp. 1243–1286. DOI: [10.1103/RevModPhys.75.1243](https://doi.org/10.1103/RevModPhys.75.1243).
- [6] ATLAS Collaboration. “Performance of the ATLAS Liquid Argon Calorimeter after three years of LHC operation and plans for a future upgrade”. In: (2013). DOI: [10.1109/ANIMMA.2013.6728060](https://doi.org/10.1109/ANIMMA.2013.6728060). arXiv: [1306.6756 \[physics.ins-det\]](https://arxiv.org/abs/1306.6756).
- [7] D Oliveira Damazio. *Signal Processing for the ATLAS Liquid Argon Calorimeter : studies and implementation*. Tech. rep. ATL-LARG-PROC-2013-015. Geneva: CERN, Nov. 2013. URL: <https://cds.cern.ch/record/1630826>.
- [8] Michael H. Seymour. “Quantum chromodynamics”. In: *2004 European School of High-Energy Physics, Sant Feliu de Guixols, Spain, 30 May - 12 June 2004*. 2005, pp. 49–94. arXiv: [hep-ph/0505192](https://arxiv.org/abs/hep-ph/0505192) [hep-ph]. URL: <http://doc.cern.ch/yellowrep/CERN-PH-TH-2005-083>.
- [9] R. Keith Ellis, W. James Stirling, and B. R. Webber. “QCD and Collider Physics”. In: *Camb. Monogr. Part. Phys. Nucl. Phys. Cosmol.* 8 (1996), pp. 1–435.
- [10] M. Tanabashi et al. “Review of Particle Physics”. In: *Phys. Rev. D* 98 (3 Aug. 2018), p. 030001. DOI: [10.1103/PhysRevD.98.030001](https://doi.org/10.1103/PhysRevD.98.030001).

- [11] Raymond Brock et al. “Handbook of perturbative QCD: Version 1.0”. In: *Rev. Mod. Phys.* 67 (1995), pp. 157–248. DOI: 10.1103/RevModPhys.67.157.
- [12] M. Creutz. *Quarks, Gluons and Lattices*. Cambridge Monographs on Mathem. Cambridge University Press, 1985. ISBN: 9780521315357. URL: <https://books.google.com/books?id=mcCyB3ewyeMC>.
- [13] Sz. Borsanyi et al. “Ab initio calculation of the neutron-proton mass difference”. In: *Science* 347 (2015), pp. 1452–1455. DOI: 10.1126/science.1257050. arXiv: 1406.4088 [hep-lat].
- [14] John W. Harris and Berndt Muller. “The Search for the quark - gluon plasma”. In: *Ann. Rev. Nucl. Part. Sci.* 46 (1996), pp. 71–107. DOI: 10.1146/annurev.nucl.46.1.71. arXiv: hep-ph/9602235 [hep-ph].
- [15] PHENIX Collaboration. “Formation of dense partonic matter in relativistic nucleus-nucleus collisions at RHIC: Experimental evaluation by the PHENIX collaboration”. In: *Nucl. Phys.* A757 (2005), pp. 184–283. DOI: 10.1016/j.nuclphysa.2005.03.086. arXiv: nucl-ex/0410003 [nucl-ex].
- [16] STAR Collaboration. “Experimental and theoretical challenges in the search for the quark gluon plasma: The STAR Collaboration’s critical assessment of the evidence from RHIC collisions”. In: *Nucl. Phys.* A757 (2005), pp. 102–183. DOI: 10.1016/j.nuclphysa.2005.03.085. arXiv: nucl-ex/0501009 [nucl-ex].
- [17] BRAHMS Collaboration. “Quark gluon plasma and color glass condensate at RHIC? The Perspective from the BRAHMS experiment”. In: *Nucl. Phys.* A757 (2005), pp. 1–27. DOI: 10.1016/j.nuclphysa.2005.02.130. arXiv: nucl-ex/0410020 [nucl-ex].
- [18] PHOBOS Collaboration. “The PHOBOS perspective on discoveries at RHIC”. In: *Nucl. Phys.* A757 (2005), pp. 28–101. DOI: 10.1016/j.nuclphysa.2005.03.084. arXiv: nucl-ex/0410022 [nucl-ex].
- [19] Edmond Iancu. “QCD in heavy ion collisions”. In: *Proceedings, 2011 European School of High-Energy Physics (ESHEP 2011): Cheile Gradistei, Romania, September 7-20, 2011*. 2014, pp. 197–266. DOI: 10.5170/CERN-2014-003.197. arXiv: 1205.0579 [hep-ph]. URL: <https://inspirehep.net/record/1113441/files/arXiv:1205.0579.pdf>.
- [20] J. D. Bjorken and Emmanuel A. Paschos. “Inelastic Electron Proton and gamma Proton Scattering, and the Structure of the Nucleon”. In: *Phys. Rev.* 185 (1969), pp. 1975–1982. DOI: 10.1103/PhysRev.185.1975.
- [21] Michael E. Peskin and Daniel V. Schroeder. *An Introduction to quantum field theory*. Reading, USA: Addison-Wesley, 1995. ISBN: 9780201503975. URL: <http://www.slac.stanford.edu/~mpeskin/QFT.html>.

- [22] L. W. Whitlow et al. “A Precise extraction of $R = \sigma_L / \sigma_T$ from a global analysis of the SLAC deep inelastic e p and e d scattering cross-sections”. In: *Phys. Lett.* B250 (1990), pp. 193–198. DOI: 10.1016/0370-2693(90)91176-C.
- [23] Yuri V. Kovchegov and Eugene Levin. *Quantum chromodynamics at high energy*. Vol. 33. Cambridge University Press, 2012. ISBN: 9780521112574. URL: <http://www.cambridge.org/de/knowledge/isbn/item6803159>.
- [24] H1, ZEUS Collaborations. “Deep inelastic cross-section measurements at large y with the ZEUS detector at HERA”. In: *Phys. Rev.* D90.7 (2014), p. 072002. DOI: 10.1103/PhysRevD.90.072002. arXiv: 1404.6376 [hep-ex].
- [25] BCDMS Collaboration. “Phenomenological Review on Quark-Gluon Plasma: Concepts vs. Observations”. In: *Universe* 3.1 (2017), p. 7. DOI: 10.3390/universe3010007. arXiv: 1611.01533 [hep-ph].
- [26] E665 Collaboration. “Proton and deuteron structure functions in muon scattering at 470-GeV”. In: *Phys. Rev.* D54 (1996), pp. 3006–3056. DOI: 10.1103/PhysRevD.54.3006.
- [27] L. W. Whitlow et al. “Precise measurements of the proton and deuteron structure functions from a global analysis of the SLAC deep inelastic electron scattering cross-sections”. In: *Phys. Lett.* B282 (1992), pp. 475–482. DOI: 10.1016/0370-2693(92)90672-Q.
- [28] J. D. Bjorken. “Asymptotic Sum Rules at Infinite Momentum”. In: *Phys. Rev.* 179 (1969), pp. 1547–1553. DOI: 10.1103/PhysRev.179.1547.
- [29] V. N. Gribov and L. N. Lipatov. “e+ e- pair annihilation and deep inelastic e p scattering in perturbation theory”. In: *Sov. J. Nucl. Phys.* 15 (1972). [Yad. Fiz. 15, 1218 (1972)], pp. 675–684.
- [30] V. N. Gribov and L. N. Lipatov. “Deep inelastic e p scattering in perturbation theory”. In: *Sov. J. Nucl. Phys.* 15 (1972). [Yad. Fiz. 15, 781 (1972)], pp. 438–450.
- [31] Yuri L. Dokshitzer. “Calculation of the Structure Functions for Deep Inelastic Scattering and e+ e- Annihilation by Perturbation Theory in Quantum Chromodynamics.” In: *Sov. Phys. JETP* 46 (1977). [Zh. Eksp. Teor. Fiz. 73, 1216 (1977)], pp. 641–653.
- [32] Guido Altarelli and G. Parisi. “Asymptotic Freedom in Parton Language”. In: *Nucl. Phys.* B126 (1977), pp. 298–318. DOI: 10.1016/0550-3213(77)90384-4.
- [33] I. I. Balitsky and L. N. Lipatov. “The Pomeranchuk Singularity in Quantum Chromodynamics”. In: *Sov. J. Nucl. Phys.* 28 (1978). [Yad. Fiz. 28, 1597 (1978)], pp. 822–829.

- [34] E. A. Kuraev, L. N. Lipatov, and Victor S. Fadin. “The Pomeranchuk Singularity in Nonabelian Gauge Theories”. In: *Sov. Phys. JETP* 45 (1977). [Zh. Eksp. Teor. Fiz. 72, 377 (1977)], pp. 199–204.
- [35] Victor S. Fadin, E. A. Kuraev, and L. N. Lipatov. “On the Pomeranchuk Singularity in Asymptotically Free Theories”. In: *Phys. Lett.* 60B (1975), pp. 50–52. DOI: 10.1016/0370-2693(75)90524-9.
- [36] L. N. Lipatov. “Reggeization of the Vector Meson and the Vacuum Singularity in Nonabelian Gauge Theories”. In: *Sov. J. Nucl. Phys.* 23 (1976). [Yad. Fiz. 23, 642 (1976)], pp. 338–345.
- [37] H. Abramowicz et al. “Combination of measurements of inclusive deep inelastic $e^\pm p$ scattering cross sections and QCD analysis of HERA data”. In: *Eur. Phys. J.* C75.12 (2015), p. 580. DOI: 10.1140/epjc/s10052-015-3710-4. arXiv: 1506.06042 [hep-ex].
- [38] Sayipjamal Dulat et al. “New parton distribution functions from a global analysis of quantum chromodynamics”. In: *Phys. Rev.* D93.3 (2016), p. 033006. DOI: 10.1103/PhysRevD.93.033006. arXiv: 1506.07443 [hep-ph].
- [39] Richard D. Ball et al. “Parton distributions from high-precision collider data”. In: *Eur. Phys. J.* C77.10 (2017), p. 663. DOI: 10.1140/epjc/s10052-017-5199-5. arXiv: 1706.00428 [hep-ph].
- [40] L. A. Harland-Lang et al. “Parton distributions in the LHC era: MMHT 2014 PDFs”. In: *Eur. Phys. J.* C75.5 (2015), p. 204. DOI: 10.1140/epjc/s10052-015-3397-6. arXiv: 1412.3989 [hep-ph].
- [41] L. V. Gribov, E. M. Levin, and M. G. Ryskin. “Semihard Processes in QCD”. In: *Phys. Rept.* 100 (1983), pp. 1–150. DOI: 10.1016/0370-1573(83)90022-4.
- [42] Alfred H. Mueller and Jian-wei Qiu. “Gluon Recombination and Shadowing at Small Values of x ”. In: *Nucl. Phys.* B268 (1986), pp. 427–452. DOI: 10.1016/0550-3213(86)90164-1.
- [43] George F. Sterman and Steven Weinberg. “Jets from Quantum Chromodynamics”. In: *Phys. Rev. Lett.* 39 (1977), p. 1436. DOI: 10.1103/PhysRevLett.39.1436.
- [44] B. R. Webber. “A QCD Model for Jet Fragmentation Including Soft Gluon Interference”. In: *Nucl. Phys.* B238 (1984), pp. 492–528. DOI: 10.1016/0550-3213(84)90333-X.
- [45] Bo Andersson et al. “Parton Fragmentation and String Dynamics”. In: *Phys. Rept.* 97 (1983), pp. 31–145. DOI: 10.1016/0370-1573(83)90080-7.
- [46] Stephen D. Ellis and Davison E. Soper. “Successive combination jet algorithm for hadron collisions”. In: *Phys. Rev.* D48 (1993), pp. 3160–3166. DOI: 10.1103/PhysRevD.48.3160. arXiv: hep-ph/9305266 [hep-ph].

- [47] Yuri L. Dokshitzer et al. “Better jet clustering algorithms”. In: *JHEP* 08 (1997), p. 001. doi: 10.1088/1126-6708/1997/08/001. arXiv: hep-ph/9707323 [hep-ph].
- [48] M. Wobisch and T. Wengler. “Hadronization corrections to jet cross-sections in deep inelastic scattering”. In: *Monte Carlo generators for HERA physics. Proceedings, Workshop, Hamburg, Germany, 1998-1999*. 1998, pp. 270–279. arXiv: hep-ph/9907280 [hep-ph].
- [49] Gerald C. Blazey et al. “Run II jet physics”. In: *QCD and weak boson physics in Run II. Proceedings, Batavia, USA, March 4-6, June 3-4, November 4-6, 1999*. 2000, pp. 47–77. arXiv: hep-ex/0005012 [hep-ex]. URL: http://lss.fnal.gov/cgi-bin/find_paper.pl?conf=00-092.
- [50] Matteo Cacciari, Gavin P. Salam, and Gregory Soyez. “The Anti-k(t) jet clustering algorithm”. In: *JHEP* 04 (2008), p. 063. doi: 10.1088/1126-6708/2008/04/063. arXiv: 0802.1189 [hep-ph].
- [51] PHENIX Collaboration. “High p_T charged hadron suppression in Au + Au collisions at $\sqrt{s_{NN}} = 200$ GeV”. In: *Phys. Rev.* C69 (2004), p. 034910. doi: 10.1103/PhysRevC.69.034910. arXiv: nucl-ex/0308006 [nucl-ex].
- [52] STAR Collaboration. “Forward- and Mid-Rapidity Jet-like correlations”. In: (2007). [Int. J. Mod. Phys.E16,3168(2007)]. doi: 10.1142/S0218301307009166. arXiv: 0707.0815 [nucl-ex].
- [53] PHENIX Collaboration. “Suppression of back-to-back hadron pairs at forward rapidity in d+Au Collisions at $\sqrt{s_{NN}} = 200$ GeV”. In: *Phys. Rev. Lett.* 107 (2011), p. 172301. doi: 10.1103/PhysRevLett.107.172301. arXiv: 1105.5112 [nucl-ex].
- [54] Javier L. Albacete and Cyrille Marquet. “Gluon saturation and initial conditions for relativistic heavy ion collisions”. In: *Prog. Part. Nucl. Phys.* 76 (2014), pp. 1–42. doi: 10.1016/j.ppnp.2014.01.004. arXiv: 1401.4866 [hep-ph].
- [55] Jean-Paul Blaizot. “High gluon densities in heavy ion collisions”. In: *Rept. Prog. Phys.* 80.3 (2017), p. 032301. doi: 10.1088/1361-6633/aa5435. arXiv: 1607.04448 [hep-ph].
- [56] ATLAS Collaboration. “Centrality and rapidity dependence of inclusive jet production in $\sqrt{s_{NN}} = 5.02$ TeV proton-lead collisions with the ATLAS detector”. In: *Phys. Lett. B* 748 (2015), pp. 392–413. doi: 10.1016/j.physletb.2015.07.023. arXiv: 1412.4092 [hep-ex].
- [57] ALICE Collaboration. “Measurement of dijet k_T in p-Pb collisions at $\sqrt{s_{NN}}=5.02$ TeV”. In: *Phys. Lett. B* 746 (2015), pp. 385–395. doi: 10.1016/j.physletb.2015.05.033. arXiv: 1503.03050 [nucl-ex].
- [58] ALICE Collaboration. “Measurement of charged jet production cross sections and nuclear modification in p-Pb collisions at $\sqrt{s_{NN}} = 5.02$ TeV”. In: *Phys. Lett. B* 749 (2015), pp. 68–81. doi: 10.1016/j.physletb.2015.07.054. arXiv: 1503.00681 [nucl-ex].

- [59] CMS Collaboration. “Measurement of inclusive jet production and nuclear modifications in pPb collisions at $\sqrt{s_{NN}} = 5.02$ TeV”. In: *Eur. Phys. J.* C76.7 (2016), p. 372. DOI: 10.1140/epjc/s10052-016-4205-7. arXiv: 1601.02001 [nucl-ex].
- [60] CMS Collaboration. “Very forward inclusive jet cross sections in p+Pb collisions at $\sqrt{s_{NN}} = 5.02$ TeV at CMS”. In: (2018), p. 045. URL: https://cds.cern.ch/record/2275228/files/CR2017_183.pdf.
- [61] T. Pierog et al. “EPOS LHC: Test of collective hadronization with data measured at the CERN Large Hadron Collider”. In: *Phys. Rev.* C92.3 (2015), p. 034906. DOI: 10.1103/PhysRevC.92.034906. arXiv: 1306.0121 [hep-ph].
- [62] Xin-Nian Wang and Miklos Gyulassy. “HIJING: A Monte Carlo model for multiple jet production in p p, p A and A A collisions”. In: *Phys. Rev.* D44 (1991), pp. 3501–3516. DOI: 10.1103/PhysRevD.44.3501.
- [63] S. Ostapchenko. “QGSJET-II: physics, recent improvements, and results for air showers”. In: *EPJ Web Conf.* 52 (2013), p. 02001. DOI: 10.1051/epjconf/20125202001.
- [64] Kari J. Eskola et al. “EPPS16: Nuclear parton distributions with LHC data”. In: *Eur. Phys. J.* C77.3 (2017), p. 163. DOI: 10.1140/epjc/s10052-017-4725-9. arXiv: 1612.05741 [hep-ph].
- [65] K. Kovarik et al. “nCTEQ15 - Global analysis of nuclear parton distributions with uncertainties in the CTEQ framework”. In: *Phys. Rev.* D93.8 (2016), p. 085037. DOI: 10.1103/PhysRevD.93.085037. arXiv: 1509.00792 [hep-ph].
- [66] Edmond Iancu, Andrei Leonidov, and Larry McLerran. “The Color glass condensate: An Introduction”. In: *QCD perspectives on hot and dense matter. Proceedings, NATO Advanced Study Institute, Summer School, Cargese, France, August 6-18, 2001.* 2002, pp. 73–145. arXiv: hep-ph/0202270 [hep-ph].
- [67] Dmitri Kharzeev, Eugene Levin, and Larry McLerran. “Jet azimuthal correlations and parton saturation in the color glass condensate”. In: *Nucl. Phys. A* 748 (2005), pp. 627–640. DOI: 10.1016/j.nuclphysa.2004.10.031. arXiv: hep-ph/0403271 [hep-ph].
- [68] F. Gelis. “Color Glass Condensate and Glasma”. In: *Int. J. Mod. Phys.* A28 (2013), p. 1330001. DOI: 10.1142/S0217751X13300019. arXiv: 1211.3327 [hep-ph].
- [69] ALICE Collaboration. “Measurement of J/ψ production in pp collisions at LHC energies with ALICE”. In: *J. Phys. Conf. Ser.* 832.1 (2017), p. 012029. DOI: 10.1088/1742-6596/832/1/012029. arXiv: 1704.04627 [hep-ex].

- [70] A. van Hameren et al. “Saturation effects in forward-forward dijet production in p+Pb collisions”. In: *Phys. Rev. D* 89.9 (2014), p. 094014. doi: 10.1103/PhysRevD.89.094014. arXiv: 1402.5065 [hep-ph].
- [71] Krzysztof Kutak and Sebastian Sapeta. “Gluon saturation in dijet production in p-Pb collisions at Large Hadron Collider”. In: *Phys. Rev. D* 86 (2012), p. 094043. doi: 10.1103/PhysRevD.86.094043. arXiv: 1205.5035 [hep-ph].
- [72] B. Potter. “JetViP 2.1: The hbook version”. In: *Comput. Phys. Commun.* 133 (2000), pp. 105–118. doi: 10.1016/S0010-4655(00)00158-2. arXiv: hep-ph/9911221 [hep-ph].
- [73] M. Klasen and G. Kramer. “Dijet cross-sections at $\alpha(\alpha\alpha)^{**2}$ in photon - proton collisions”. In: *Phys. Lett.* B366 (1996), pp. 385–393. doi: 10.1016/0370-2693(95)01352-0. arXiv: hep-ph/9508337 [hep-ph].
- [74] Stefano Frixione and Giovanni Ridolfi. “Jet photoproduction at HERA”. In: *Nucl. Phys.* B507 (1997), pp. 315–333. doi: 10.1016/S0550-3213(97)00575-0. arXiv: hep-ph/9707345 [hep-ph].
- [75] Marcin Bury et al. “Calculations with off-shell matrix elements, TMD parton densities and TMD parton showers”. In: *Eur. Phys. J.* C78.2 (2018), p. 137. doi: 10.1140/epjc/s10052-018-5642-2. arXiv: 1712.05932 [hep-ph].
- [76] Torbjorn Sjostrand et al. “An Introduction to PYTHIA 8.2”. In: *Comput. Phys. Commun.* 191 (2015), pp. 159–177. doi: 10.1016/j.cpc.2015.01.024. arXiv: 1410.3012 [hep-ph].
- [77] S. Agostinelli et al. “GEANT4: A Simulation toolkit”. In: *Nucl. Instrum. Meth.* A506 (2003), pp. 250–303. doi: 10.1016/S0168-9002(03)01368-8.
- [78] ATLAS Collaboration. “The ATLAS Simulation Infrastructure”. In: *Eur. Phys. J. C* 70 (2010), pp. 823–874. doi: 10.1140/epjc/s10052-010-1429-9. arXiv: 1005.4568 [physics.ins-det].
- [79] ATLAS Collaboration. “Measurement of jet fragmentation in 5.02 TeV proton-lead and proton-proton collisions with the ATLAS detector”. In: *Nucl. Phys.* A978 (2018), pp. 65–106. doi: 10.1016/j.nuclphysa.2018.07.006. arXiv: 1706.02859 [hep-ex].
- [80] ATLAS Collaboration. *ATLAS Run 1 Pythia8 tunes*. ATLAS-PHYS-PUB-2014-021. URL: <https://cds.cern.ch/record/1966419>.
- [81] Richard D. Ball et al. “Parton distributions with LHC data”. In: *Nucl. Phys.* B867 (2013). doi: 10.1016/j.nuclphysb.2012.10.003. arXiv: 1207.1303 [hep-ph].

- [82] M. Bahr et al. “Herwig++ Physics and Manual”. In: *Eur. Phys. J. C* 58 (2008), pp. 639–707. doi: 10.1140/epjc/s10052-008-0798-9. arXiv: 0803.0883 [hep-ph].
- [83] ATLAS Collaboration. “Jet energy measurement with the ATLAS detector in proton-proton collisions at $\sqrt{s} = 7$ TeV”. In: *Eur. Phys. J. C* 73 (2013). doi: 10.1140/epjc/s10052-013-2304-2. arXiv: 1112.6426 [hep-ex].
- [84] ATLAS Collaboration. *Jet calibration and systematic uncertainties for jets reconstructed in the ATLAS detector at $\sqrt{s}=13$ TeV*. ATLAS-PHYS-PUB-2015-015. URL: <https://cds.cern.ch/record/2037613>.
- [85] CMS Collaboration. “Studies of dijet transverse momentum balance and pseudorapidity distributions in pPb collisions at $\sqrt{s_{\text{NN}}} = 5.02$ TeV”. In: *Eur. Phys. J. C* 74.7 (2014), p. 2951. doi: 10.1140/epjc/s10052-014-2951-y. arXiv: 1401.4433 [nucl-ex].
- [86] ATLAS Collaboration. “Jet energy scale and its uncertainty for jets reconstructed using the ATLAS heavy ion jet algorithm”. In: (2015). ATLAS-CONF-2015-016. URL: <https://cds.cern.ch/record/2008677>.
- [87] ATLAS Collaboration. “Measurement of the nuclear modification factor for inclusive jets in Pb+Pb collisions at $\sqrt{s_{\text{NN}}} = 5.02$ TeV with the ATLAS detector”. In: (2018). arXiv: 1805.05635 [nucl-ex].
- [88] ATLAS Collaboration. “Jet energy measurement and its systematic uncertainty in proton-proton collisions at $\sqrt{s} = 7$ TeV with the ATLAS detector”. In: *Eur. Phys. J. C* 75 (2015), p. 17. doi: 10.1140/epjc/s10052-014-3190-y. arXiv: 1406.0076 [hep-ex].
- [89] ATLAS Collaboration. “In situ calibration of large- R jet energy and mass in 13 TeV proton-proton collisions with the ATLAS detector”. In: *Submitted to: Eur. Phys. J.* (2018). arXiv: 1807.09477 [hep-ex].
- [90] ATLAS Collaboration. “Angular correlations of jets in lead-lead collisions at 2.76 TeV using the ATLAS detector at the LHC”. In: *Nuclear Physics A* 931 (2014). QUARK MATTER 2014, pp. 455–459. ISSN: 0375-9474. doi: <https://doi.org/10.1016/j.nuclphysa.2014.08.024>.
- [91] Lynne H. Orr and W. James Stirling. “BFKL physics in dijet production at the LHC”. In: *Phys. Lett. B* 436 (1998), pp. 372–378. doi: 10.1016/S0370-2693(98)00864-8. arXiv: hep-ph/9806371 [hep-ph].
- [92] Krzysztof Kutak and Dawid Toton. “Gluon saturation scale from the KGBJS equation”. In: *JHEP* 11 (2013), p. 082. doi: 10.1007/JHEP11(2013)082. arXiv: 1306.3369 [hep-ph].

- [93] Krzysztof Kutak. “Hard scale dependent gluon density, saturation and forward-forward dijet production at the LHC”. In: *Phys. Rev.* D91.3 (2015), p. 034021. doi: 10.1103/PhysRevD.91.034021. arXiv: 1409.3822 [hep-ph].